

MULTI-TRANSDUCER ULTRASONIC COMMUNICATION

A THESIS SUBMITTED TO  
THE GRADUATE SCHOOL OF NATURAL AND APPLIED SCIENCES  
OF  
MIDDLE EAST TECHNICAL UNIVERSITY

BY

ERDEM ERSAGUN

IN PARTIAL FULFILLMENT OF THE REQUIREMENTS  
FOR  
THE DEGREE OF MASTER OF SCIENCE  
IN  
ELECTRICAL AND ELECTRONICS ENGINEERING

FEBRUARY 2009

Approval of the thesis:

**MULTI-TRANSDUCER ULTRASONIC COMMUNICATION**

submitted by **ERDEM ERSAGUN** in partial fulfillment of the requirements for the degree of **Master of Science in Electrical and Electronics Engineering Department, Middle East Technical University** by,

Prof. Dr. Canan Özgen  
Dean, **Graduate School of Natural and Applied Sciences**

\_\_\_\_\_

Prof. Dr. İsmet Erkmen  
Head of Department, **Electrical and Electronics Engineering**

\_\_\_\_\_

Assoc. Prof. Dr. A. Özgür Yılmaz  
Supervisor, **Electrical and Electronics Engineering Dept., METU**

\_\_\_\_\_

**Examining Committee Members:**

Prof. Dr. Yalçın Tanık  
Electrical and Electronics Engineering Dept., METU

\_\_\_\_\_

Assoc. Prof. Dr. A. Özgür Yılmaz  
Electrical and Electronics Engineering Dept., METU

\_\_\_\_\_

Assoc. Prof. Dr. Ö. Barış Akan  
Electrical and Electronics Engineering Dept., METU

\_\_\_\_\_

Assist. Prof. Dr. Çağatay Candan  
Electrical and Electronics Engineering Dept., METU

\_\_\_\_\_

Ahmet Doğrusöz, PhD.  
ASELSAN

\_\_\_\_\_

**Date:**

04.02.2009

**I hereby declare that all information in this document has been obtained and presented in accordance with academic rules and ethical conduct. I also declare that, as required by these rules and conduct, I have fully cited and referenced all material and results that are not original to this work.**

Name, Last Name: Erdem ERSAGUN

Signature :

## **ABSTRACT**

### MULTI-TRANSDUCER ULTRASONIC COMMUNICATION

Ersagun, Erdem

M.Sc., Department of Electrical and Electronics Engineering

Supervisor : Assoc. Prof. Dr. A. Özgür Yılmaz

February 2009, 113 pages

RF and acoustic communications are widely used in terrestrial and underwater environments, respectively. This thesis examines the use of ultrasonic communication alternately in terrestrial applications. We first investigate the ultrasonic channel in order to observe whether reliable communication is possible among the ultrasonic nodes as an alternative to RF-based communications. Some key characteristics of the single-input-single-output (SISO) and single-input-multiple-output (SIMO) ultrasonic channel are inspected with extensive experiments utilizing ultrasonic transmitters and receivers. Well known receiver diversity techniques are employed to combine the observations of multiple receiving ultrasonic transducers in a SIMO scheme and receiver diversity gain is attained. The thesis also covers the implementation of a receiver node by using a low-cost microcontroller.

Keywords: ultrasonic communication, ultrasonic channel, single-input-single-output, single-input-multiple-output, receiver diversity.

## ÖZ

### ÇOKLU DÖNÜŞTÜRÜCÜLÜ SESÜSTÜ HABERLEŞME

Ersagun, Erdem

Yüksek Lisans, Elektrik-Elektronik Mühendisliği Bölümü

Tez Yöneticisi : Doç. Dr. A. Özgür YILMAZ

Şubat 2009, 113 sayfa

RF ve akustik haberleşme, sırasıyla karasal ve sualtı ortamlarda geniş ölçüde kullanılmaktadır. Bu çalışmada, sesüstü haberleşmenin karasal uygulamalardaki kullanımı incelenmektedir. Sesüstü kanalı gözlemekteki amacımız, RF haberleşmeye alternatif olarak, sesüstü alıcı-vericiler arasında güvenilir haberleşmenin mümkün olup olmadığını değerlendirmektir. Tek girdili – tek çıktılı (SISO) ve tek girdili – çok çıktılı (SIMO) sesüstü kanala ait bazı önemli özellikler, sesüstü alıcı ve vericilerin kullanıldığı deneyler ile gözlemlenmiştir. SIMO sesüstü kanalında, literatürde tanımlanmış olan alıcı çeşitlemesi algoritmaları kullanılarak çoklu dönüştürücülere ait gözlemler birleştirilmiş ve alıcı çeşitlemesi kazancı sağlanmıştır. Bu çalışma ayrıca bir alıcı düğümün düşük maliyetli bir mikroişlemci ile gerçekleştirilmesini de kapsamaktadır.

Anahtar Kelimeler: sesüstü haberleşme, sesüstü kanal, tek girdili – tek çıktılı sistem, tek girdili – çok çıktılı sistem, alıcı çeşitlemesi.

To My Family

## **ACKNOWLEDGMENTS**

I would like to thank Assoc. Prof. Dr. A. Özgür Yılmaz for his valuable guidance, supervision, advice, criticism, encouragements, and insight throughout the development and improvement of this thesis.

I would also like to express my deepest gratitude to Miss Özlem Yılmaz for her interest, advice, and support.

I would like to extend my special appreciation to my family for their encouragement. They have given me not only throughout my thesis but also throughout my life.

## TABLE OF CONTENTS

ABSTRACT.....	iv
ÖZ.....	v
ACKNOWLEDGMENTS.....	vii
TABLE OF CONTENTS.....	viii
LIST OF TABLES.....	xi
LIST OF FIGURES.....	xii
CHAPTER	
1. INTRODUCTION.....	1
1.1 Motivation .....	1
1.2 Scope of Thesis.....	3
1.3 Outline of Thesis .....	4
2. PAST RESEARCH ON ACOUSTIC COMMUNICATION.....	6
2.1 Underwater Acoustic Communications.....	6
2.2 Terrestrial Acoustic Communications .....	7
3. EXPERIMENTAL SETUP FOR ULTRASONIC CHANNEL MEASUREMENTS .....	10
3.1 Transmitter.....	10
3.1.1 Signal Generator.....	11
3.1.2 Transmitting Ultrasonic Transducer.....	12
3.2 Receiver .....	15
3.2.1 Receiving Ultrasonic Transducer .....	16
3.2.2 Amplifier .....	16
3.3 A/D Converter Module.....	20
3.4 Experiment Environment.....	21

4. EXPERIMENTAL RESULTS .....	23
4.1 Overview .....	23
4.2 Free-space Ultrasonic Channel Measurements.....	24
4.2.1 Signal Selection for Transmission.....	24
4.2.2 Signal Processing and Results.....	25
4.3 Multipath Ultrasonic Channel Measurements .....	32
4.4 Receiver Correlation.....	40
4.5 Transmission of Modulated Signals .....	45
4.5.1 Signal Modulation and Demodulation .....	45
4.5.2 Receiver Diversity Combining.....	49
4.6 Conclusion .....	53
5. DEVICES AND TOOLS FOR IMPLEMENTING AN ULTRASONIC RECEIVER NODE .....	54
5.1 PIC 18F452.....	54
5.1.1 Loading Software to the Microcontroller.....	56
5.1.2 Initialization Options.....	57
5.1.3 RS-232 Serial Channel Communication .....	58
5.1.4 A/D Conversion.....	61
5.1.5 Sampling Rate Adjustment.....	63
5.2 Power Supply.....	66
5.3 Programming Language and Compiler.....	67
6. THE IMPLEMENTATION OF A DOUBLE TRANSDUCER ULTRASONIC RECEIVER NODE .....	72
6.1 Packet Detection.....	72
6.1.1 Down-Conversion .....	74
6.1.2 The Matched Filtering Operation.....	76
6.1.3 Thresholding and Detection Mechanism.....	82
6.1.3.1 Determining Threshold Level.....	83
6.1.3.2 Implementation of the CFAR Detection Mechanism .....	85
6.2 The Implementation of D-BPSK Demodulation .....	91
6.3 Testing and Measuring System Performance .....	93
6.3.1 Observing Computational Results on PIC 18F452 .....	93

6.3.2	Timing Measures.....	95
6.3.3	Memory Measures.....	96
6.3.4	False Alarm Rate Observations.....	97
6.3.5	BER Measurements.....	99
6.4	Conclusion.....	101
7.	CONCLUSION.....	103
7.1	Summary.....	103
7.2	Conclusions on Experiments.....	104
7.3	Conclusion on Implementations.....	106
7.4	Future Directions.....	107
	REFERENCES.....	109

## LIST OF TABLES

### TABLES

Table 1.1 Ultrasonic frequency ranges and typical applications [6].....	2
Table 3.1 Some piezoelectric materials and their piezoelectric constants [16] ...	12
Table 3.2 Some piezoelectric materials and their conversion efficiency [12] .....	13
Table 3.3 Specifications of ultrasonic transducer C40-12 [17] [18].....	14
Table 4.1 SNR and spectral efficiencies .....	31
Table 5.1 Fuse options used on the microcontroller .....	58
Table 5.2 Durations of mathematical operations for 18F452 [35].....	69
Table 5.3 Standard data types supported by PCW compiler.....	71
Table 6.1 Average accuracy loss at step 3 of the pseudo code .....	76
Table 6.2 Execution times (in units of timer increments) for different phases....	96
Table 6.3 Amount of memory elements used .....	97
Table 6.4 False alarm rate observations .....	98

## LIST OF FIGURES

### FIGURES

Figure 3-1 Transmitter side .....	10
Figure 3-2 D/A module: NI USB-6211 [13] .....	11
Figure 3-3 C40-12 series ultrasonic transducers .....	13
Figure 3-4 Sensitivity and Sound Pressure Level (SPL) [37] .....	14
Figure 3-5 Beam angle of the transducers tested at 40 kHz [37] .....	15
Figure 3-6 Receiver side .....	15
Figure 3-7 TL072 Pin diagram [22] .....	17
Figure 3-8 The two-stage amplifier .....	18
Figure 3-9 AC analysis of amplifier circuit .....	19
Figure 3-10 A/D module: NI USB-6009 [23] .....	20
Figure 3-11 Indoor experiment environment .....	21
Figure 4-1 Autocorrelation function of 13-element Barker code .....	25
Figure 4-2 The received Barker waveform and the matched filter output .....	26
Figure 4-3 The received Barker waveform and the matched filter output .....	27
Figure 4-4 Matched filter output split into windows of 374 samples .....	29
Figure 4-5 Noise at the matched filter output .....	29
Figure 4-6 Distribution of the noise components at the matched filter output ....	30
Figure 4-7 Maximum SNR vs. transmitter-receiver range .....	31
Figure 4-8 Spectral efficiency vs. transmitter-receiver range .....	32
Figure 4-9 Matched filter output for a LOS transmission .....	34
Figure 4-10 Matched filter output for a LOS transmission .....	34
Figure 4-11 Coherent sum of the matched filter output, indoor environment .....	35
Figure 4-12 Coherent sum of the matched filter output, indoor environment .....	36
Figure 4-13 Coherent sum of the matched filter output, outdoor environment ...	37
Figure 4-14 Coherent sum of the matched filter output, outdoor environment ...	38

Figure 4-15 Coherent sum of the matched filter output, outdoor environment ...	39
Figure 4-16 Coherent sum of the matched filter output, outdoor environment ...	39
Figure 4-17 FFT performed on windows of 150 samples.....	41
Figure 4-18 FFT performed on windows of 150 samples.....	42
Figure 4-19 Magnitude of peaks at each window .....	44
Figure 4-20 Magnitude of peaks at each window .....	44
Figure 4-21 Receiver correlation.....	45
Figure 4-22 D-BPSK modulation structure.....	46
Figure 4-23 PSK and D-BPSK waveforms [29] .....	47
Figure 4-24 D-BPSK demodulation structure.....	47
Figure 4-25 Measured BER for receivers 1&2 and with MRC.....	52
Figure 5-1 PIC 18F452 pin diagram [31].....	56
Figure 5-2 PIC 18F452 serial programmer .....	56
Figure 5-3 IC-Prog serial programmer software .....	57
Figure 5-4 MAX232 pin diagram [32].....	59
Figure 5-5 PIC18F452 and MAX232 connections for a typical application .....	60
Figure 5-6 HyperTerminal configuration for serial communication.....	61
Figure 5-7 FFT operation performed on 1350 samples.....	65
Figure 5-8 Flow chart for sampling the two analog channels.....	66
Figure 5-9 LM7805 pin diagram [34] .....	67
Figure 5-10 Screenshot of the PCW C Compiler IDE .....	68
Figure 6-1 Block diagram for packet detection.....	73
Figure 6-2 Average bit error probability vs. average branch SNR [28].....	74
Figure 6-3 Matched filter construction for the 13-length Barker sequence .....	77
Figure 6-4 The matched filtering operation on a length-78 linear window .....	78
Figure 6-5 78-length circular window used for filtering operation.....	79
Figure 6-6 Execution of matched filtering operation for consecutive iterations..	80
Figure 6-7 Block diagram for calculating the threshold adaptively.....	86
Figure 6-8 Overall data packet structure .....	87
Figure 6-9 Flow chart for packet detection .....	89
Figure 6-10 Threshold levels for a number of ratio constants $K$ .....	90
Figure 6-11 Convolution with rectangular filter .....	91

Figure 6-12 Comparison of PIC and MATLAB outputs.....	95
Figure 6-13 False alarm rate for a number of ratio constants K .....	99
Figure 6-14 BER measurements for varying receiver-transmitter separations ..	101

# CHAPTER 1

## INTRODUCTION

### 1.1 Motivation

Acoustic communication research has mainly focused on the area of underwater acoustic sensor networks for the purpose of oceanographic data collection, pollution monitoring, offshore exploration, disaster prevention, assisted navigation, and tactical surveillance applications [1]. RF communication is preferred in terrestrial environments for many reasons such as its proven efficiency and low cost, and is the primary choice for power limited applications such as wireless sensor networks (WSN) [2].

In this thesis, we explore the use of ultrasonic communication in terrestrial applications. The ultrasonic channel is a part of the acoustic channel and consists of acoustic frequencies above the range audible to the human ear, which lies above approximately 20 kHz [3]. Ultrasound has been utilized in many applications in medicine, manufacturing, and so on [4]. Table 1.1 summarizes some usage areas of ultrasound along with the frequency ranges. However, its use in communications has been very much limited to underwater except for a few studies. This is in large due to the short-range coverage of this channel. For example, an ultrasonic indoor positioning system which operates in the range 10-20 m is presented in [5]. Although the short-range of the ultrasonic communication may deem it of little use in many communication scenarios, we believe that its short range is not important in a WSN since the nodes in a WSN communicate at quite small distances, e.g., tens of meters. Furthermore, in such a network the amount and rate of data transfer among the nodes is not required to

be in the order of other wireless communication devices such as wireless modems that provide huge data streams at the rates of a few Mbps. In a WSN, for instance, a few bytes sent at the rates of a few kbps may be sufficient to monitor the status of the nodes and to configure their operations. Moreover, even in the necessity of higher data rates, the ultrasonic channel may well provide a backup channel on which it may be possible to continue some sort of degraded mode capabilities with reduced packet sizes or communication rates in the presence of persistent RF failures. To this extent, WSNs may be enhanced to reach a more robust sense and may keep exchanging crucial data even under severe environmental conditions. Presenting an alternative to RF communication is one of the main motivations for this study, since diversification in communication media is very important especially in some areas such as military communication.

**Table 1.1** Ultrasonic frequency ranges and typical applications [6]

<b>Applications</b>	<b>Frequency</b>
Upper limit of human hearing	16 kHz
Defoaming and degassing	2-30 kHz
Ultrasonic metal working and welding	16-25 kHz
Control applications	16-45 kHz
Ultrasonic cleaning	20-40 kHz
Nondestructive testing (NDT)	1-10 MHz

A very important benefit in using the ultrasonic channel is the ease of design and manufacturing at lower frequencies. There are many active and inactive components such as capacitors, amplifiers and analog-to-digital converters that work very efficiently at low frequencies, and are accessible even at the level of undergraduate students in electrical engineering programs. The design and manufacturing processes will be simplified and made available to a larger community at least for educational purposes if ultrasonic communication is

utilized. For instance, a research group, specialized in communication theory rather than building communication systems, can check and validate many of their studies simply by using relatively low speed analog-to-digital converters along with a low-complexity analog circuitry to perform all communication related operations in a more familiar PC platform.

The speed of the sound waves in air is around 350 m/sec depending on temperature, humidity etc. [3]. The low propagation speed of sound in air, in comparison with the speed of electromagnetic waves, is likely to yield shorter wavelengths depending on its frequency, as well. For instance, the wavelength of the 40 kHz ultrasound employed in our experiments is about 8.5 mm in air. Recalling that antennas should be placed in the order of wavelengths in multiple input-multiple output (MIMO) systems, this means that multiple antennas can be located within a small transmitter or receiver without demanding larger sizes. This is the main benefit in using ultrasound for communication purposes and is in opposition to RF waves, since the same wavelength for RF corresponds to approximately 35 GHz which would introduce some difficulties related to working with extremely high frequencies. Hence, we investigate the use of multiple transducers in order to see whether diversity or multiplexing gains of MIMO systems are possible in a small size enabled by ultrasound.

## **1.2 Scope of Thesis**

In this thesis, it is intended to examine the ultrasonic channel in order to observe whether reliable communication is possible among the ultrasonic nodes of a WSN. Hence, building up an experiment setup constitutes an important milestone in this study. To this extent a transmitter that is able to transmit ultrasonic signals of the desired waveform and a receiver scheme that first amplifies the received ultrasonic signal, than samples and transfers to a PC for further analysis are utilized.

The results of excessive experiments conducted in both indoor and outdoor environments are used to draw some important conclusions about the ultrasonic channel. Experiments are extended to the case where two ultrasonic transducers are used at the receiver side to observe possible receiver diversity gain. Some well-known diversity techniques widely available in the literature are applied for this purpose and the diversity gain attained is demonstrated a from the bit error rate (BER) curves.

Relying on the offline computations and analysis, an 18F452 series PIC (Programmable Interface Controller) microcontroller is employed to execute algorithms of the receiver in real-time. Several adjustments and fine-tunings are applied on both hardware and software which is implemented in the C programming language using a standard compiler and IDE (Integrated Development Environment) optimized for the mentioned series of microcontrollers.

### **1.3 Outline of Thesis**

The outline of this thesis can be summarized as follows.

Chapter 2 consists of a brief summary of the noteworthy past research efforts on acoustic communication both in terrestrial and underwater environments.

Chapter 3 reveals experimental setup details. It presents receiver and transmitter models assumed in the scope of this thesis.

Chapter 4 presents important experimental results along with offline calculations and analysis regarding ultrasonic channel justifying the efforts on implementing an ultrasonic receiver node.

Chapter 5 is devoted to preliminary work required for implementation of an ultrasonic receiver node by using a PIC microcontroller. Several hardware and software related issues related to customizing tools and devices for implementation are treated in this chapter.

Chapter 6 provides details for the implementation of an ultrasonic receiver node that executes selection diversity combining technique on two receiver transducers.

Finally, Chapter 7 concludes the thesis along with highlights on some future directions.

## **CHAPTER 2**

### **PAST RESEARCH ON ACOUSTIC COMMUNICATION**

This chapter is devoted to noteworthy past research in the area of acoustic communications. It is organized as to overview underwater and terrestrial applications separately since many distinct concerns are present due to the different communication media.

#### **2.1 Underwater Acoustic Communications**

There are many research interests in the area of underwater acoustic communications. RF waves are exposed to high attenuation and optical signals suffer from severe scattering thus leaving acoustic link as the primary choice for the underwater environment [1]. The efforts for underwater object ranging (sonar) during the World War II gave rise to the first serious application of acoustics in this environment [7]. In [7], experiments are performed for underwater acoustic communication and many practical aspects of the channel are observed. For instance, communication rates in the order of Kb/s are attained over distances up to 10 km under LOS conditions.

One may refer to [8] for recent advances in underwater acoustic communication. With the emerging use areas both in military and commercial applications, requirements for system performance put forth high data rates as a necessity in underwater communication. Although many underwater communication systems employ non-coherent modulation techniques, [8] encourages the use of

bandwidth effective phase coherent modulation schemes to achieve higher data rates under severe multipath propagation. Here crucial aspects of signal design and processing considerations are pointed at and experimental results for the proposed system is provided as to coherently detect signals transmitted at 30 and 40 Kb/s through one-mile shallow water.

In [1], some important research challenges are discussed to deploy underwater sensors for the purpose of oceanographic data collection, pollution monitoring, offshore exploration, disaster prevention, assisted navigation, and tactical surveillance applications. The proposed architectures for the acoustic sensor networks are classified into static two-dimensional, static three-dimensional and three-dimensional networks with autonomous vehicles depending on the network topology and different usage areas. The study contributes to the analysis of many factors that influence underwater acoustic communication including path loss, noise, multipath, and Doppler spread. Performance of several digital modulation schemes are also inspected in terms of bit rates and communication ranges underlining the performance differences under deep and shallow water circumstances.

In an ongoing project described in [9], utilization of autonomous vehicles in a three-dimensional architecture for underwater acoustic sensor networks is realized. It emphasizes two important challenges in this area as adapting to the changes in environmental conditions due to the movement of the underwater platform and self configuration for fully autonomous behavior.

## **2.2 Terrestrial Acoustic Communications**

Communication in terrestrial acoustic channel has created interest for some time. For instance, [10] tries to propose a new form of communication for WSNs when link quality or possible hardware damages cause RF communication failures. Therefore, it refers to the ultrasonic channel in order to retrieve some important

data of the nodes after subjected to these failures. The main motivation in their study is to demonstrate that the ultrasonic channel is capable of providing reliable communication and can be utilized as a backup channel in WSNs. The study includes development of a communication protocol which is organized so that physical and MAC (medium access control) layers are handled separately. In the physical layer, the Manchester coding scheme is applied since it provides self-clocking features and eliminates phase recovery activities at the receiver side. In the MAC layer, acoustic channel status is followed to avoid collisions and automatic acknowledgement is generated after successful reception. The main restriction in the study is the use of existing hardware with 4.5 kHz sounder as a transmitter and a tone detector with the operation range of 4.3 kHz – 5.2 kHz as a receiver. Hence, with the proposed scenario, successful packet delivery range does not exceed a few meters. Analysis on bit error rate reveals that, with their existing hardware, bit rates should be around 6 bps to achieve successful delivery even the transmitter-receiver separation is 1.5 feet.

In another study, 40 kHz ultrasonic transducers are used as a part of indoor localization system that is utilized for equipment and asset tracking in a hospital [5]. The attainable range in this study is 10-20 m and thus suitable for indoor use in practice. An important feature of the proposed system is that ultrasound is used as the only mean for communication. The system uses the principle of confinement and insulating properties of walls unlike the usual RF/ultrasound mixed localization systems where the time difference of arrival is tracked for RF signals and ultrasound to locate an object. Another important difference from the common ultrasound based localization systems is that many important data exchange including time, status ID, equipment ID etc. is accomplished over the ultrasonic channel. In the communication system proposed in that study, rather than an adaptive thresholding mechanism, fixed threshold scheme is used at the receiver side for detection of transmission in the channel. Performance of the system is estimated by making comparison with speech and local whistling languages rather than actual experiences. Since some nodes are worn by humans, Doppler shift introduced to the system is analyzed, as well. From those analyses,

a data rate in the range 16.7 – 100 bps is found to be achievable which is also specified to be consistent with the actual system performance. [11] details the hardware and software aspects of the same system. The transmitter (placed in a tag) consists of an ultrasonic transducer, a microprocessor, a battery, a movement sensor and optionally an optical tampering sensor. At the transmitter side, a carrier sense multiple access protocol (CSMA) is provided to prevent packet collisions in the channel. On the other hand, the stationary receivers use more powerful computational units that are capable of processing signals fed from a total of 8 ultrasonic transducers with no mention on the used receiver diversity scheme.

In the ultrasonic communication project developed by the National Security Program Office in the U.S.A digital signal processing techniques are applied for ultrasonic communication through air and many other solid media [12]. Commercially available ultrasonic transducers are utilized throughout. Many considerations such as system efficiency, low power consumption, ultrasound propagation and absorption in different media are identified and inspected in the scope of the study. Since the aim of the project is to develop an ultrasonic communication system, the study reviews many practical aspects such as amplifier design, communication range, handshaking protocols, error checking considerations, and noise filtering. The finalized system achieves a communication rate of 75 bps over a distance of 10 feet (approximately 3 m) through pipes filled with air. Computer files and images are successfully transmitted at this rate.

## CHAPTER 3

### EXPERIMENTAL SETUP FOR ULTRASONIC CHANNEL MEASUREMENTS

The following sections define the whole system model used in the scope of experiments conducted on the ultrasonic channel. They start with the details of transmitter scheme and continue with the receiver model revealing the details of its components. Finally, the indoor experiment environment which hosts many of the experiments is overviewed.

#### 3.1 Transmitter

The simple transmitter scheme depicted in Figure 3-1 is employed in the experiments. The components of the transmitter are a signal generator and an ultrasonic transducer whose details follow in the subsequent subsections. As a signal generator, an arbitrary waveform generator device or a DAC module is utilized depending on the nature of the experiments to be conducted. For instance, complex signals like the 13-chip Barker waveform is simply constructed by the DAC module, whereas the signal-to-noise ratio (SNR) can be readily adjusted by an arbitrary waveform generator.



**Figure 3-1** Transmitter side

### 3.1.1 Signal Generator

As a signal generator, the Agilent 33220A Function and Arbitrary Waveform Generator or the NI USB-6211 D/A converter module is used depending on the experiments. For instance, for frequency sweeping or signal amplitude adjustments, 33220A provides a simple interface that can readily be used.

Experiments that require more mobility are performed with USB-6211 as it is lightweight and bus-powered from a USB interface hence requiring no external power supply in the presence of a laptop. The generation of user-defined waveforms is performed by USB-6211. When used in coordination with the software Labview Signal Express of National Instruments, it accepts desired waveforms in the form of standard ASCII files. The device has two analog output ports and has a maximum D/A conversion rate of 250 KS/s which is capable of driving 40 kHz ultrasonic transducers.



**Figure 3-2** D/A module: NI USB-6211 [13]

### 3.1.2 Transmitting Ultrasonic Transducer

Transducers used in the experiment and implementation phases in this study are produced from piezoelectric materials that are able to convert mechanical vibrations into electrical signals and vice versa. Ultrasound generation depends on the deformation of piezoelectric substances under electric fields. This deformation can be very fast in some materials up to 500 MHz, the material has to relax to its original dimensions to obtain intended response [14]. If the piezoelectric material is exposed to mechanical stress, the deformation in its dimensions gives rise to generation of electric field. Hence, the piezoelectric materials can be employed to fabricate both ultrasound generator and detector transducers. There are many materials that exhibit the behavior discussed here. The following two tables list some of those along with their piezoelectric constants and conversion efficiency, respectively. One of the most famous piezoelectric materials is quartz crystal primarily used for its good electrical and thermal stability and high resistance to wear and aging. However its low conversion coefficient and the requirement for large voltages for low frequency oscillation restrict its use in some applications [15].

**Table 3.1** Some piezoelectric materials and their piezoelectric constants [16]

<b>Material</b>	<b>Piezoelectric Constant (<math>\times 10^{12}</math> m/V)</b>
Quartz	2.3
Barium titanate	100-149
Lead niobate	80-85
Lead zirconate titanate	250-365

**Table 3.2** Some piezoelectric materials and their conversion efficiency [12]

Material	Conversion Efficiency (%)
Quartz	0.01
ADP	0.7
BaTiO <sub>3</sub>	4.0
PZT#5 (Lead Zirconate-Lead Titanate Mixture)	20.0

Commercially available C40-12 series ultrasonic transducers are used in the experiments. The letter ‘C’ in the part number implies that it is capable of both transmitting and receiving ultrasonic signals. Many other series that are specifically labeled as ‘T’ or ‘R’ are also available for only transmitting and receiving purposes, respectively. As ‘C’ series reduce the required number of transducers in a transeiving node, it is the primary choice in the experiments performed herein. The numerals in the part number 40 and 12 correspond to the operating frequency and the diameter of the transducer in mm, respectively. Although the manufacturer information is not specified on the devices employed in the experiments, the following table lists many typical characteristics of 40 kHz-12 mm diameter ultrasonic transducers obtained from several manufacturer datasheets.



**Figure 3-3** C40-12 series ultrasonic transducers

**Table 3.3** Specifications of ultrasonic transducer C40-12 [17] [18]

<b>Center Frequency</b>	40 kHz $\pm$ 1 kHz
<b>Nominal Impedance</b>	1 K $\Omega$
<b>Sound Pressure Level</b> (0 dB = 0.0002 $\mu$ bar) (for transmission)	$\sim$ 115 dB
<b>Sensitivity</b> (0 dB = 1 Volt/ $\mu$ bar) (for reception)	$\sim$ -70 dB
<b>Directivity (-6 dB)</b>	$\sim$ 60 $^\circ$
<b>Capacitance</b>	2000 pF $\pm$ 20% pF
<b>Housing Material</b>	Aluminum
<b>Driving Voltage</b>	$\leq$ 60 V <sub>pp</sub>
<b>Operating Temperature</b>	-20 $^\circ$ C $\sim$ +70 $^\circ$ C
<b>Storage Temperature</b>	-30 $^\circ$ C $\sim$ +80 $^\circ$ C

Figure 3-4 depicts the change of sensitivity and sound pressure level as a function of the frequency which is obtained by transmitting 10 V<sub>rms</sub> at a 30 cm receiver-transmitter separation [37]. Figure 3-5 demonstrates the beam angle of the transducer which is tested at 40 kHz [37].

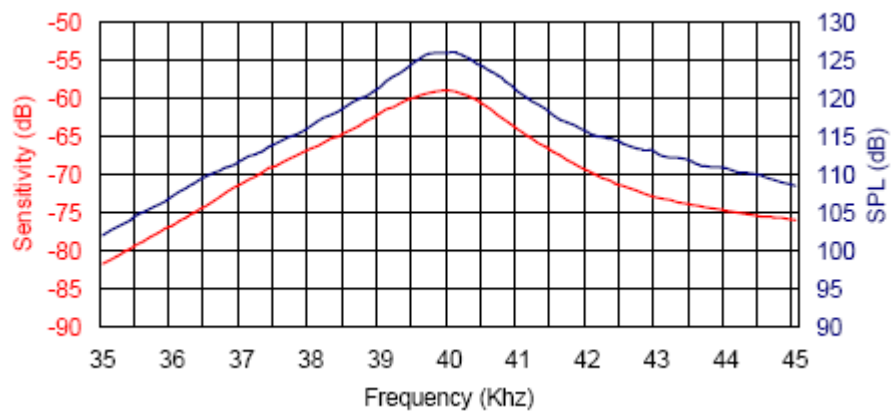


**Figure 3-4** Sensitivity and Sound Pressure Level (SPL) [37]

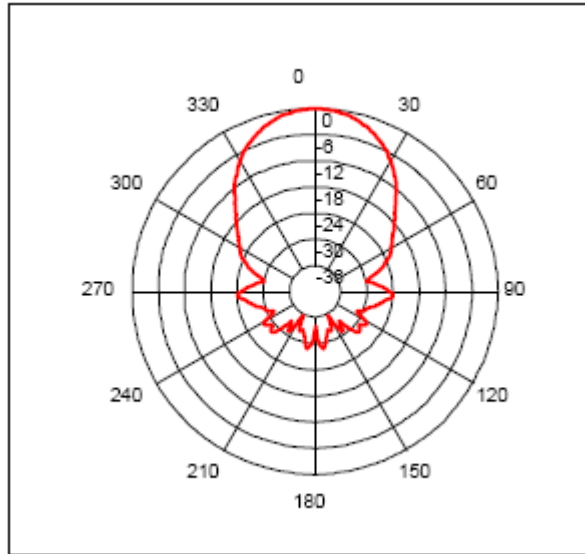


**Figure 3-5** Beam angle of the transducers tested at 40 kHz [37]

### 3.2 Receiver

Figure 3-6 shows a receiver scheme with multiple receiving ultrasonic transducers. The received ultrasonic signal is first passed through an amplifier and then sampled with an A/D converter. Specific tools for handling the sample points and the activities performed to transform relevant data to a PC platform are all explained in the following subsections. Note that separate amplifiers are employed for separate channels in the receiver. Consequences of this design choice are discussed as it comes into consideration.

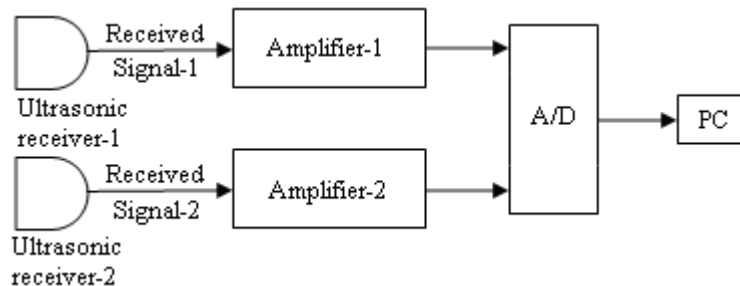


**Figure 3-6** Receiver side

### **3.2.1 Receiving Ultrasonic Transducer**

The transducers used for ultrasound reception are identical to the ones used for ultrasound transmission as the piezoelectric materials used to fabricate those devices are capable of both converting mechanical stress into voltage and vice versa. Separate pairs of transmitting and receiving ultrasonic transducers are produced by several manufacturers and specified to be optimized for only transmission or reception purposes; analysis of possible improvements in the communication range by utilizing such pairs of transducers is not treated in this thesis and left for future studies.

### **3.2.2 Amplifier**

In order to amplify ultrasonic signal at the receiver side, an amplifier scheme consisting of two stages is proposed in Figure 3-8. It is a common cascaded inverting amplifier circuit, highly used for ultrasonic applications as in [19] [20]. The first stage provides 10 times (20 dB) and the second stage provides 100 times (40 dB) voltage gains summing up to 60 dB of voltage gain at the output. Voltage gain is not intended to be more than 40 dB in a single stage because, if more than 40 dB voltage gain is to be attained in a stage, special care must be taken to avoid internal oscillations and unexpected behavior [21].

Note that the amplifier circuit uses a single power supply. This design selection reduces the circuit size and cost which should be important criteria in WSNs. IC TL072 is an OP-AMP (operational amplifier) that supports single supply applications over a wide range of voltages. It produces the maximum peak-to-peak output voltage for the frequencies lying below approximately 100 kHz [22]. Therefore it specifically enables 40 kHz ultrasonic signal amplification. Figure 3-7 displays the pin schematics of TL072. A single IC includes two identical OP-AMPs permitting circuit size reductions for applications as in our case in which two cascaded stages are required.

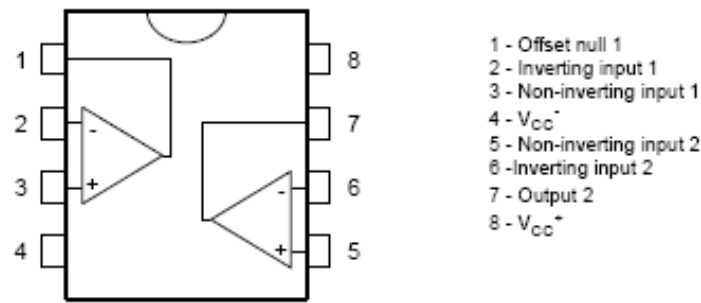


**Figure 3-7** TL072 Pin diagram [22]

One of the most important features of TL072 is its low noise behavior. The typical noise floor is specified as  $15nV / \sqrt{Hz}$  [22]. TL071 is another IC series having the same electrical characteristics as TL072 but containing a single OP-AMP. A practical analysis on low noise behavior of TL071 and a comparison with two other highly available IC's can be found in [12]. It can be concluded from that study that TL071 is a good choice providing low noise floor yet having low price. Although the experiment setup utilized in this thesis primarily focuses on the SIMO capability in the ultrasonic channel and investigates receiver diversity, employing low noise amplifiers evidently enhances the experimental results in terms of enabling observation of more multi-paths and conducting experiments in longer distances.

It is not desirable to have an outgrowing DC voltage gain at the output, since it can cause saturation depending on the electrical characteristics of the OPAMP and the amplitude of the control voltage  $V_{CC}$ . Furthermore, the output of the amplifier is passed through A/D converter modules that all have upper voltage limits beyond which it produces the same sampling value. For example, the maximum voltage level that can be sampled by the PIC 18F452's internal A/D converter is 5 V and slightly higher voltages cannot be distinguished. Even higher voltages may produce harmful effects on the holding capacitor or any other internal circuitry inside the microcontroller and should be avoided. For this

reason, coupling capacitors are provided at the input of each stage. Note that the reference voltage used by the input and output of the each stage is the virtual ground obtained by a simple voltage divider. Hence the output AC voltage is forced to swing above and below of a predetermined DC voltage level, specifically  $V_{CC}/2$ , which maximizes the observable peak-to-peak AC amplitude range at the output node.

There is a trade-off between electrical noise and power consumption in the selection of resistor values. For high speed applications, resistors in the range  $100\text{-}\Omega$  to  $1\text{-k}\Omega$  are recommended with higher power consumption and good noise performance, while resistors in the order of  $1\text{-M}\Omega$  consume less power with less immunity to noise [21]. Since the ultrasonic application in our case can be categorized as a medium speed application and initially there is no strict criterion on power consumption, the resistor values that are depicted in Figure 3-8 along with the corresponding capacitors are chosen all with 1% tolerance.

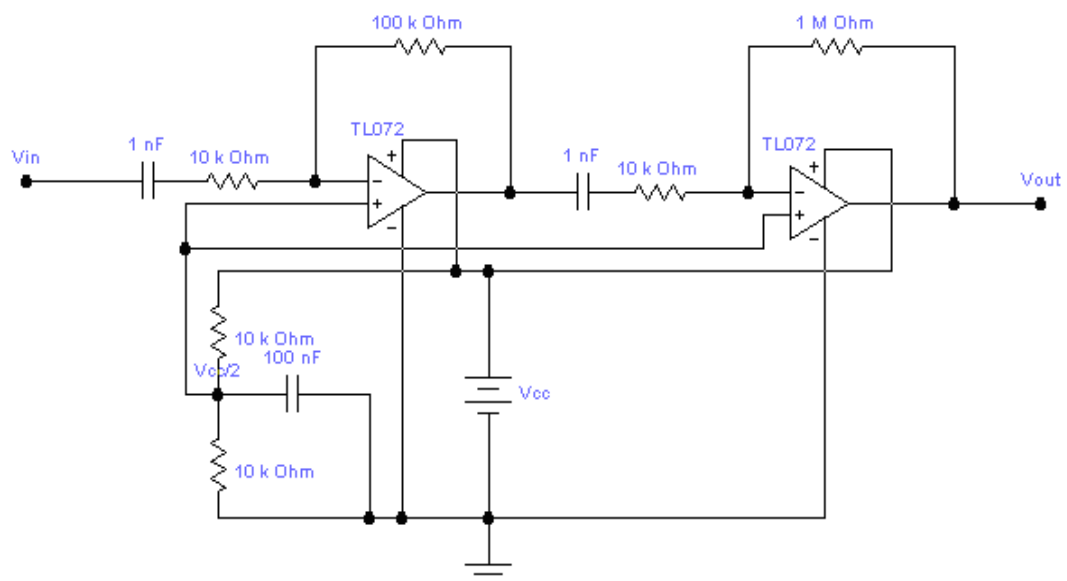


**Figure 3-8** The two-stage amplifier

Figure 3-9 shows the AC-frequency analysis of the amplifier circuit conducted with Electronics Workbench v. 5.0.c. It is a simple tool enabling basic circuits' construction and testing with simulation. In Figure 3-9, the plots are obtained by

supplying an AC source to the input node with a constant peak amplitude of 1 mV sinusoidal and sweeping frequency in the range of 10 kHz to 60 kHz. From this result, maximum voltage gain is 58.98 dB and it occurs around 29.5 kHz. At the ultrasonic transducers' operating frequency of 40 kHz, the voltage gain decreases to 58.28 dB; 0.7 dB decrease is fairly negligible for the sake of experiments.

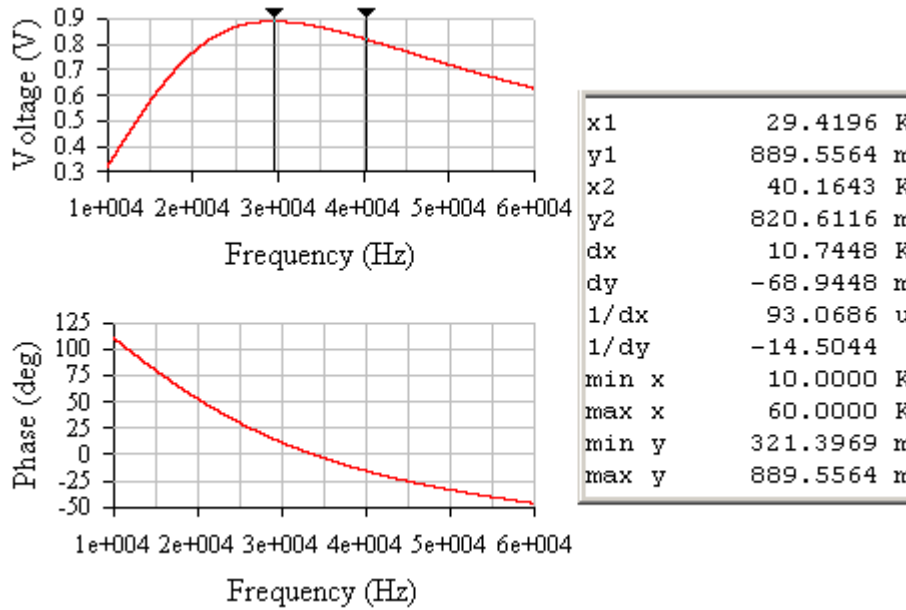


**Figure 3-9** AC analysis of amplifier circuit

One can note from the simulation results that the circuit exhibits bandpass amplifier characteristics. However, it has a large  $BW_{3-dB}$  of around 44 kHz. According to the formula given below, the quality factor  $Q$ , which is an important metric for filters, is found to be 0.677 for 29.5 kHz center frequency. This is evidently inadequate to filter out the noise components within a very narrow bandwidth as in our case; however it truly removes cumbersome fine-tuning activities to be performed to match the filter center frequency and the transducers' operating frequency.

$$Q = \frac{f_c}{BW_{3dB}} \quad (3.1)$$

### 3.3 A/D Converter Module

Referring to Figure 3-6, the amplified signals are sampled with an analog-to-digital converter. National Instruments' multi channel/general purpose data acquisition product USB-6009 is used for this purpose. It provides 14-bit resolution for a wide range of analog input levels at a maximum sampling rate of 48 kS/s [23]. In fact, this sampling rate is shared among the separate channels, i.e. one can use a maximum rate of 24 kS/s to record two separate channels. The device also allows low-rate D/A conversion, up to 150 S/s, which is not utilized in this study. Figure 3-10 shows a general view of the device NI-USB-6009.



**Figure 3-10** A/D module: NI USB-6009 [23]

In order to avoid exhaustion with excessive calculations, very large sampling rates are avoided. For most of the experiments a sampling rate of 6 kHz is found to be convenient for a bit duration of 1 ms based on the bandpass sampling theorem. Along with many other parameters, sampling rate and upper/lower voltage bounds to observe are important settings that are software configurable with National Instruments' LabVIEW Signal Express v.2.5.0. Adjustments on these upper/lower bounds enable the use of 14-bit in an optimum range, hence giving rise to enhancement of resolution.

NI data acquisition module's abilities to operate continuously and keep corresponding records enable long duration observations. It does not require an external power module; it is bus-powered from a standard USB interface which makes it more compact. One of the most important features of USB-6009, when used along with the tool LabVIEW Signal Express, is the ease of access to the stored sample points. The records can be readily converted to a standard format such as MS Excel or text file that can be transferred as an input to the MATLAB for further analysis.

### 3.4 Experiment Environment

The experiments are conducted both in outdoor and indoor environments. Figure 3-11 depicts the laboratory of dimensions about 12x6x3 meters with no carpet on the floor as carpets may absorb the energy of the acoustic signals. The receiver and the transmitter are located approximately 75 cm above the floor and the separation between them is adjusted according to the nature of the experiment to be performed.

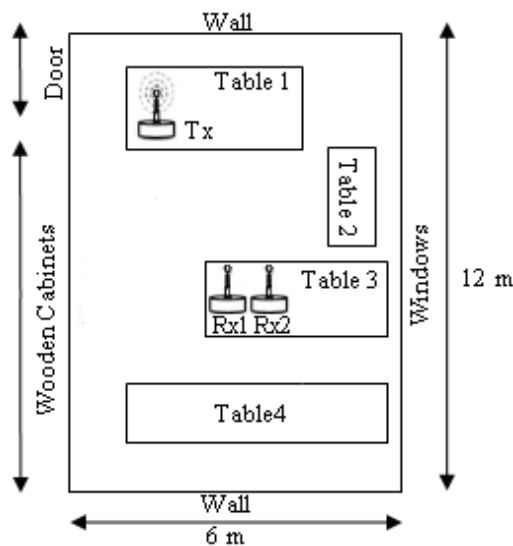


**Figure 3-11** Indoor experiment environment

Figure 3-11 shows a specific placement of the transmitter and the two receivers which are positioned on the tables 1 and 3, respectively. The environment is suitable to observe several multi-paths as there are many scatterers such as tables, chairs, monitors, and laboratory equipments such as signal generators, oscilloscopes, power supplies on the tables.

## CHAPTER 4

### EXPERIMENTAL RESULTS

#### 4.1 Overview

The experiments presented in this section start with the free-space ultrasonic channel observations performed in an outdoor environment. Having transmitted a pilot sequence, namely the 13-element Barker code, the channel is recorded and the response of the ultrasonic channel and transducers is observed in large time windows. Furthermore, SNR is calculated at varying transmitter and receiver separations. This allows obtaining the maximum spectral efficiency, a measure for achievable amount of information exchange between the nodes. The experiment also inspects the limit at which the signal strength is still above the noise floor for the detection range with the setup in hand.

Delay spread is an important parameter in ISI-channels. To measure the differences in the time arrivals of multipath signals, another experiment is performed in an indoor environment suitable to model as an ISI-channel.

MIMO (multiple-input-multiple-output) systems are proven to have increased the capacity and taken advantage of diversity techniques for enhanced communication in RF channels, when signal correlation between the multiple terminals is low [24][25]. To draw similar results and examine relevant channel characteristics, the correlation of the channel gains at two ultrasonic receivers under both LOS and non-LOS conditions at high SNR are presented in this section.

Depending on the results obtained in the previous steps, a maximal ratio combining (MRC) based technique is applied for an actual data transmission scenario and the receiver diversity gain for the ultrasonic channel is inspected. The modulation and demodulation schemes and the details of the combining algorithm are presented in the following subsections.

## **4.2 Free-space Ultrasonic Channel Measurements**

Free-space ultrasonic channel observations are important in the sense that they provide a better feeling about the channel and the response of the transducers in the absence of inter-symbol interference (ISI) related concerns. Specifically, the range limit for detecting ultrasonic signal and latency introduced by the electromechanical components of the transducers are investigated in this experiment. Furthermore it is possible to calculate the ultrasonic channel capacity under the assumption of additive white Gaussian noise (AWGN). To comply with the tasks defined herein, the experiments are performed in an outdoor environment with no possible source of multipath around.

### **4.2.1 Signal Selection for Transmission**

In the experiment, a pilot sequence consisting of the well known 13-element Barker code is sent by the transmitter. The amplitude of the transmitted waveform is set to be  $5 V_{pp}$ . The Barker code family yields a peak-to-peak mainlobe-sidelobe ratio of 13 [26]. One of the unique characteristics of those codes is that the energy in sidelobes is uniformly distributed and still kept at a minimum [27].

Figure 4-1 shows the autocorrelation of 13-element Barker code employed in the experiment. Note that the mainlobe has 13 times greater amplitude than the equal-amplitude sidelobes which enhances the possible detection range. This is

the primary reason for using a pilot sequence. It can serve to synchronize the receiver in the sense that demodulation starts at the correct time. The details of the use of the Barker code is left to the implementation phase where detection and synchronization constitute two major problems to be solved for actual data transmission.

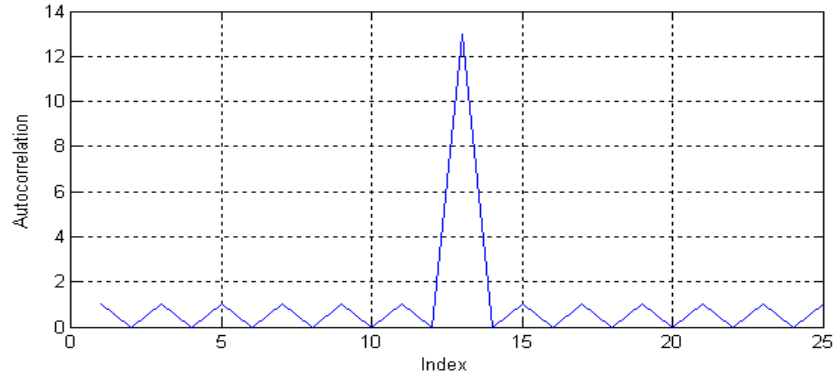


**Figure 4-1** Autocorrelation function of 13-element Barker code

### 4.2.2 Signal Processing and Results

While the transmitter transmits Barker waveform continuously at each 63 ms (50 ms delay is put between each consecutive waveform), the receiver records the channel at distances starting from 1 m. For the ease of implementation, rectangular windowing is used to construct the analog waveforms. The chip duration, the time interval at which the distinct symbols of the Barker code is sent, is set to be 1 ms. Hence the transmission of the 13-element Barker code is finalized at 13 ms. Analog waveforms are all sampled at 6 kHz at the receiver side. The digitized symbols are down-converted to the baseband and then convolved with the filter matched to the Barker sequence as

$$r_I[k] = r[k] \times \cos(2\pi f_c kT), \quad (4.1)$$

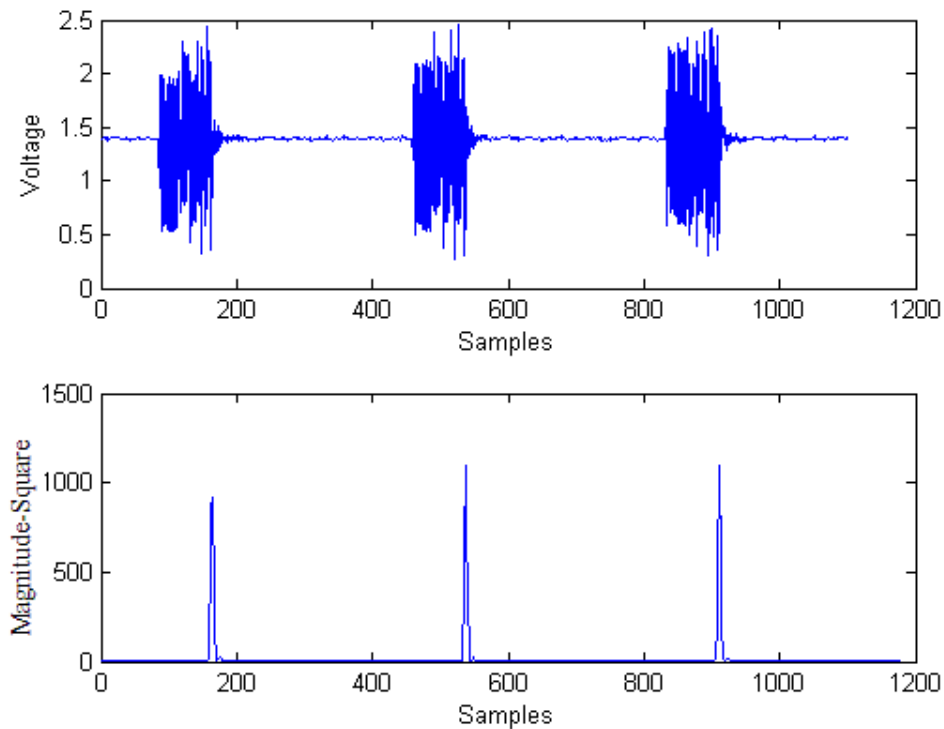
$$r_Q[k] = -r[k] \times \sin(2\pi f_c kT), \quad (4.2)$$

$$r_{Lp}[k] = r_I[k] + jr_Q[k], \quad (4.3)$$

$$y[k] = h[k] * r_{Lp}[k], \quad (4.4)$$

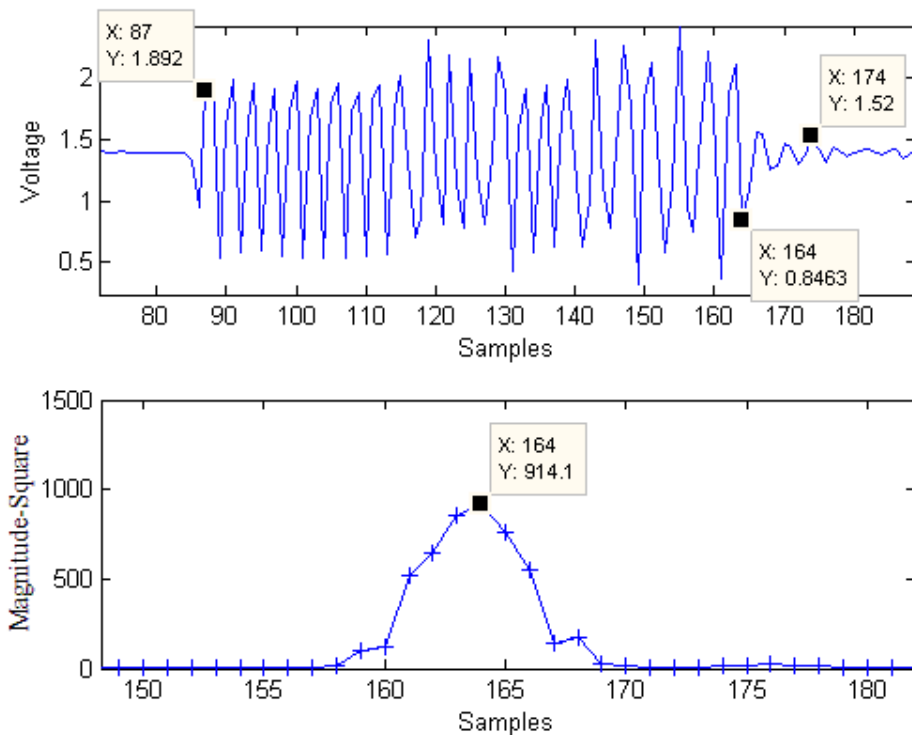
where  $k = 0, 1, \dots, T = 1/6000s$ ,  $r[k]$  denotes the received symbols,  $h[k]$  is the filter matched to the Barker sequence, and  $y[k]$  is the output of the matched filter. Low pass filtering that should follow the mixers in order to obtain the baseband equivalent signal is performed as combined with the Barker code matching. Here we refer to the samples after mixing as baseband signals.

Figure 4-2 depicts a small section of the A/D conversion along with the output of matched filter corresponding to that section when the separation between the receiver and the transmitter is 1 m.



**Figure 4-2** The received Barker waveforms and the corresponding matched filter output for 1 m separation of receiver and transmitter

The response time of the electromechanical components of the transducers can be examined by zooming around a signal component depicted in the figure above. The response observed here is from the input of the transducer at the transmitter side to the input of D/A module. So, the channel response measured here consists of the conversion at the transducers, the physical communication medium etc. By performing the experiments in a free-space-like environment the delay spread due to possible multipaths in the channel is avoided.



**Figure 4-3** The received Barker waveform and the corresponding matched filter output for 1 m separation of receiver and transmitter, zoomed in

With the sampling rate of 6 kHz and chip duration of 1 ms, 6 samples are taken from each chip. Since the 13-element Barker code is employed, a total of 78 samples are collected from the waveform. As it is seen from Figure 4-3, a power peak occurs at the sample index 164. The samples in the interval [87, 164] in the

voltage plot belong to the modulated Barker waveform. The voltage level can still be distinguished from the noise level, with a peak to peak amplitude 7 times lower than the previous interval, up until the sample index 174. This is due to spread response of the electromechanical components and lasts about 1.5 ms. Note in the power plot that 6 samples from right or left of a peak crosses the zero-power axis, hence this delayed response of the transducers may not have a significant destructive effect.

Observing that each successive peak occurs at a period of 374 samples in average (about 63 ms) in the power plot, the whole matched filter output is split into windows of 374 samples. Now, each window contains signal components and noise components which can be separated for noise variance and SNR calculations. In Figure 4-4, samples in the interval [1, 100] can be treated as the noise components only and can be used for noise variance estimation. Figure 4-5 reveals a 3-D graph for noise power that is extracted from Figure 4-4. From the noise data, noise variance  $N_0$  is estimated to be  $4.2e-3$ . This result agrees with the other measurements from which noise variance is estimated to be in the range  $4.2e-3$  to  $4.9e-3$  depending on the environmental conditions. Since magnitude squared terms are involved in the derivation, it is a power related term that can be used in SNR calculation conveniently and no absolute unit of power is required here. A histogram depicting the Gaussian-distribution of real and imaginary parts of noise is given in Figure 4-6. Hence complex-Gaussian noise model will be applied at the output of the matched filter.

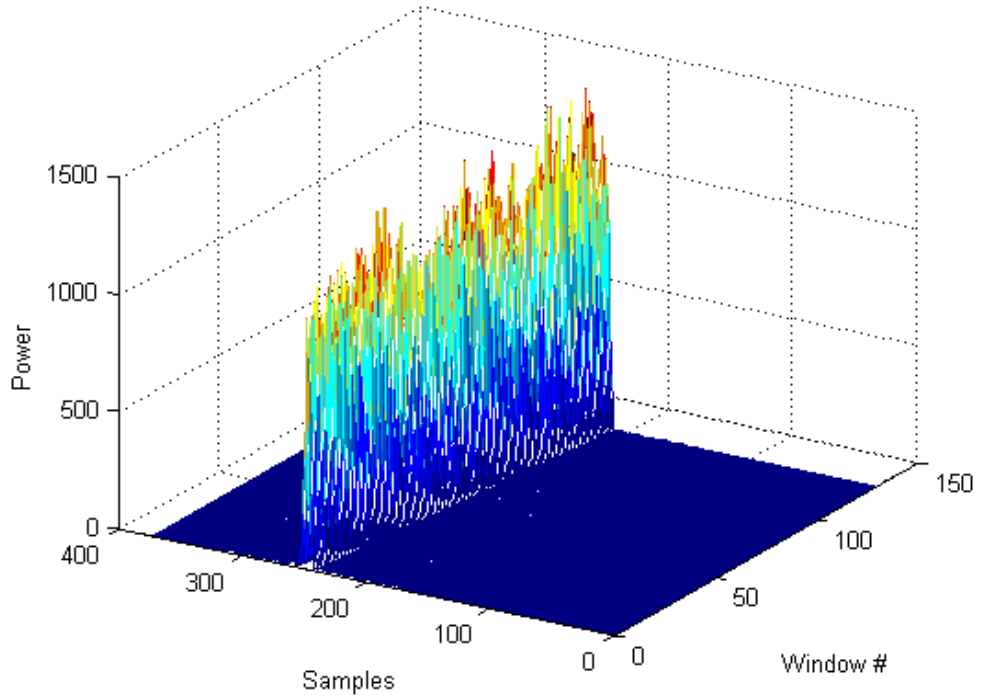


**Figure 4-4** Matched filter output split into windows of 374 samples for 1 m separation of receiver and transmitter

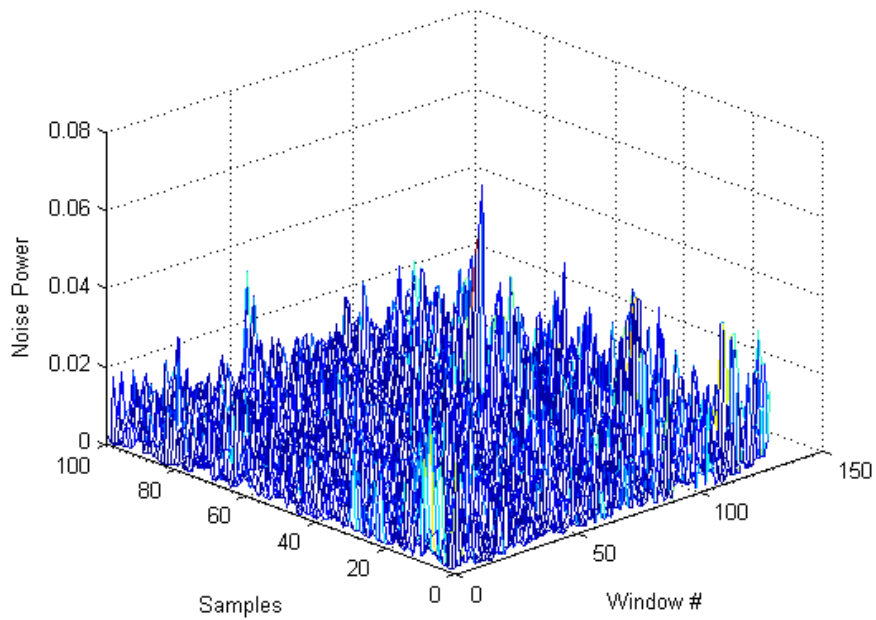


**Figure 4-5** Noise at the matched filter output for 1 m separation of receiver and transmitter

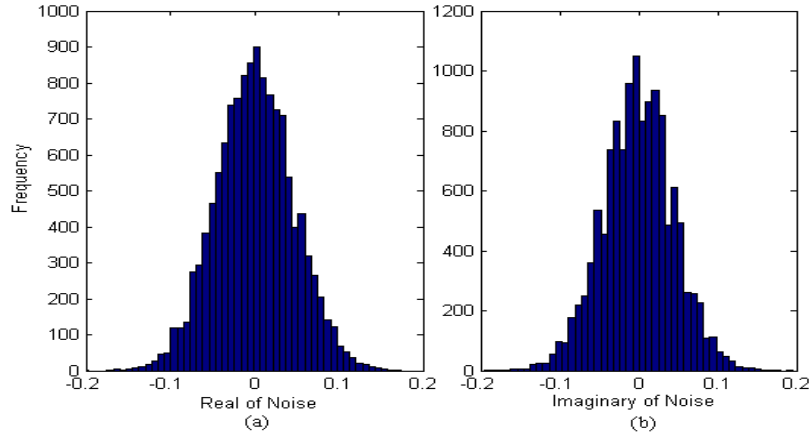


**Figure 4-6** Distribution of the noise components at the matched filter output for 1 m separation of receiver and transmitter, (a) real part, (b) imaginary part

In order to calculate the SNR, we use the formula below in which the spreading gain of 13 that is introduced by the Barker code is taken into account. The formula makes sense for the points where the signal power peaks occur in Figure 4-4.

$$SNR = \frac{P_{signal}}{13 \times N_0} \quad (4.5)$$

The maximum spectral efficiency  $\eta$  can be used as a measure for comparing the amount of information exchange that can be achieved by altering the transmitter-receiver separation. For the AWGN channel, the maximum  $\eta$  is given as, where C denotes the channel capacity in bits/s and B is the channel bandwidth in Hz.

$$\eta = \frac{C}{B} = \log_2(1 + SNR), \quad (4.6)$$

Referring to Figure 4-4 again,  $SNR_{max}$  is calculated for each window. Thereafter, this maximum SNRs are averaged ( $\overline{SNR_{max}}$ ) over the windows to put into the

formula (4.6). For 1 m separation between transmitter and the receiver  $\overline{SNR}_{\max}$  and the corresponding spectral efficiency are calculated to be 43.5 dB and 14.423 bps/Hz, respectively. The following table and the figures summarize all the results obtained with varying transmitter-receiver ranges.

**Table 4.1** SNR and spectral efficiencies obtained for altering transmitter-receiver separations

Separation (m)	$\overline{SNR}_{\max}$ (dB)	$\eta$ (bps/Hz)
1	43.4173	14.4230
5	26.6847	8.8676
10	13.1128	4.4248
15	6.9000	2.5602
20	1.3702	1.2455

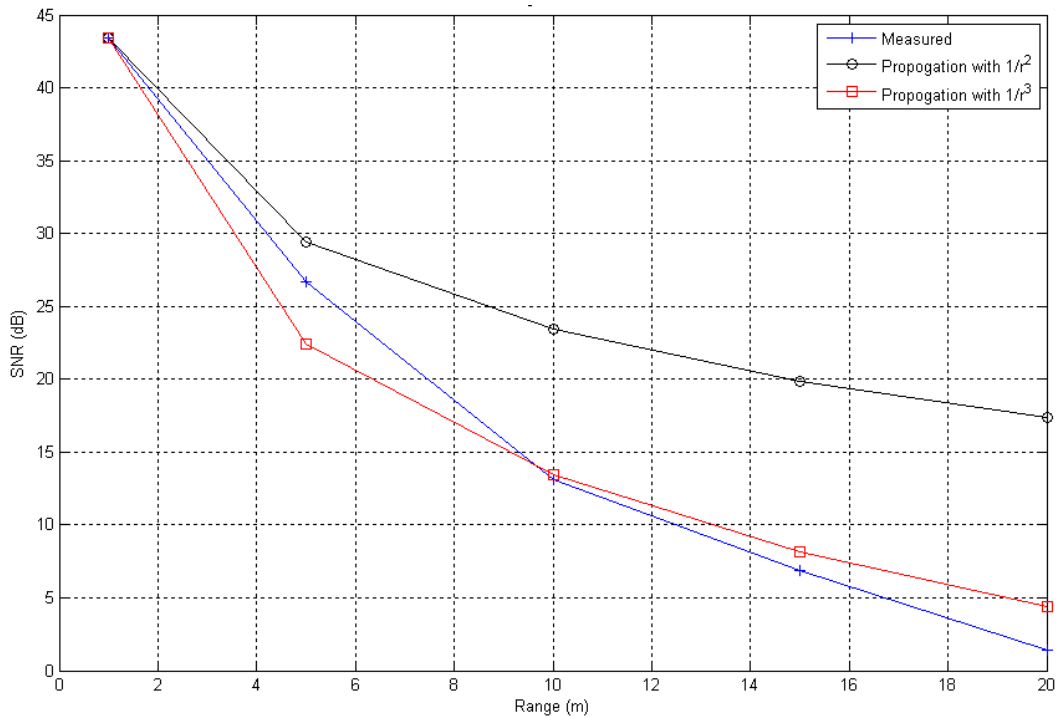


**Figure 4-7** Maximum SNR averaged over windows vs. transmitter-receiver range

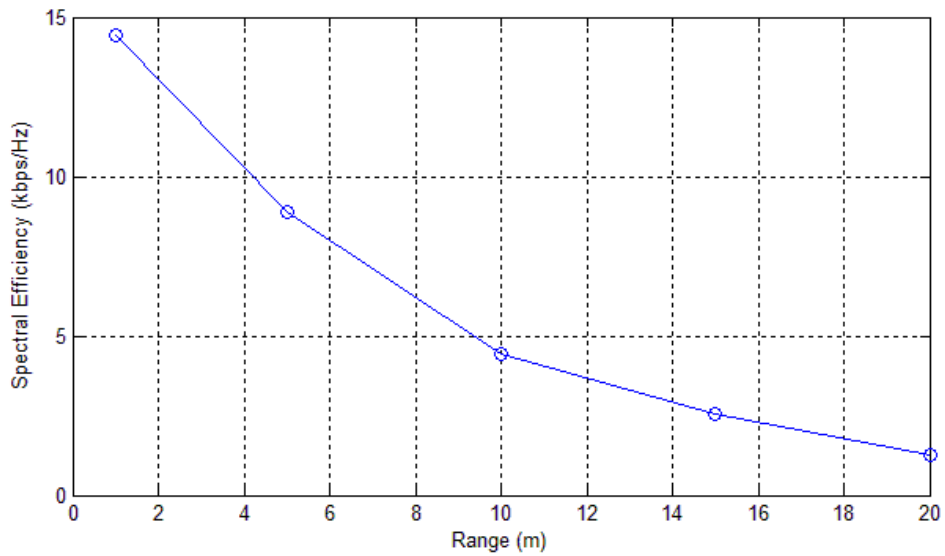


**Figure 4-8** Spectral efficiency vs. transmitter-receiver range

From communication range point of view, the preamble is still fairly above the noise level at 20 m. According to the results depicted in Table 4.1, one can expect to transmit hundreds of bits at that range, around 1 kbps for 1 kHz communication bandwidth.

### 4.3 Multipath Ultrasonic Channel Measurements

Delay spread is one of the most important characteristics of the multipath channels. In this section it is intended to provide some useful measures regarding the average delay spread within the ultrasonic channel relying on empirical measurements obtained from multipath environments. Although some characterization methods for the channel delay spread exist, such as rms delay spread and excess delay spread depending on the power delay profile, here the contribution of multipath components that are significantly above the noise floor is considered for estimating the channel average delay spread. Since

understanding the general impact of delay spread on multipath channels does not require exact characterization of this parameter, we do not aim to provide a complete characterization for the power delay profile but rather to present rough measures on the delay associated with significant multipath components [28]. As the channel delay spread highly depends on the propagation environment, separate experiments are conducted both in outdoor and indoor environments to inspect corresponding channel characteristics.

A receiver and a transmitter are located on table 1 and 4, respectively in the indoor experiment environment as described in the previous chapter. This corresponds to a transmitter-receiver separation of around 4 m. The transmitted waveform is the output of the arbitrary waveform generator operating in burst mode of period 100 msec. In each burst, a 40 KHz sinusoidal with peak-to-peak amplitude of 1 V and duration of 1 msec, corresponding to 40 cycles, is applied to the transmitter. At the receiver side, 1.4 seconds of continuous data is recorded at 45 kHz sampling rate. As an exception in the experiment setup for the indoor multipath channel observations case only, a multiple feedback bandpass amplifier scheme is used with the OP-AMP LM324 which provides 14 dB power gain. The details of this type of amplifier topology can be found in [36].

First, the orientation of the transmitter and the receiver are aligned in order to inspect the channel under strong LOS condition. The received bandpass signal is down-converted to baseband as explained in the previous section. Afterwards, the baseband signal is passed through a matched filter which is a rectangular window consisting of 45 samples in this case. Figure 4-9 depicts the matched filter output for the LOS transmission. The signal level can be distinguished from the noise level by around 14 dB. Apart from the LOS component, no strong multipath components can be distinguished in this scheme. In Figure 4-10 it can be seen that from the beginning of the rise to the end of fall centered at a peak point takes approximately 140 samples corresponding to 3 msec. Hence the average delay spread of the channel is estimated to be around 1 msec taking into account the

burst duration of 1 msec. The channel may be modeled as a narrowband fading channel at 1 kHz communication bandwidth.

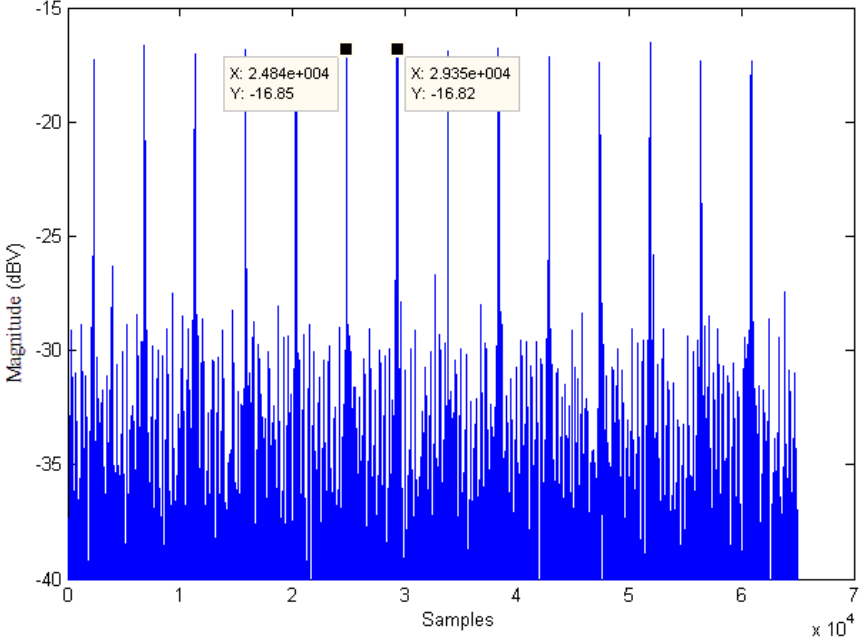


**Figure 4-9** Matched filter output for a LOS transmission in an indoor environment

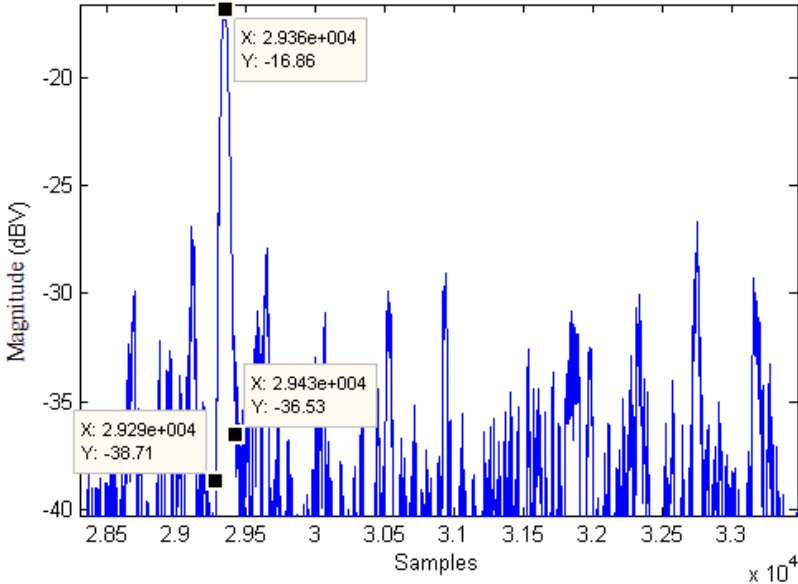


**Figure 4-10** Matched filter output for a LOS transmission in an indoor environment, zoomed around a peak

The collected data is split into delay bins taking into account burst period of 100 msec and 45 kHz sampling rate. Therefore each delay bin consists of 4500 sample points. Figure 4-11 shows the coherent sum of the bins by Fast Fourier Transform (FFT) for further signal amplification as pulse-doppler radar. It should be stated that the frequency axis corresponds to the oscillator mismatch between the A/D converter module and the arbitrary waveform generator. Here frequency offset between these devices is estimated to be 2.8 Hz.

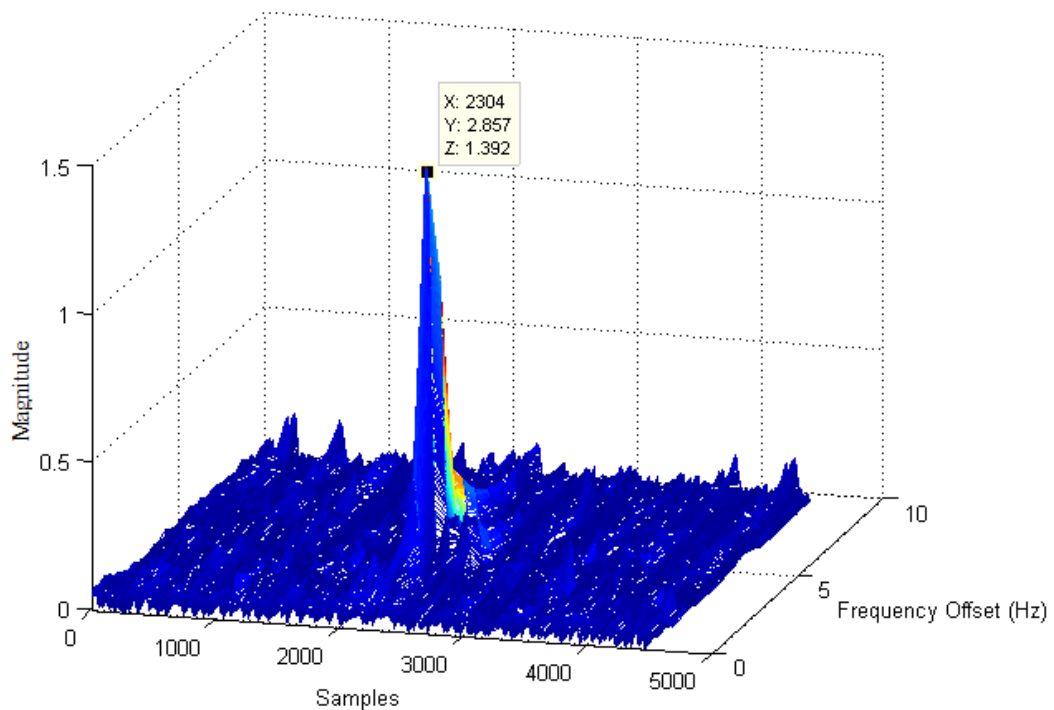


**Figure 4-11** Coherent sum of the matched filter output for a LOS transmission in an indoor environment

The orientations of the transmitter and the receiver are rearranged to observe stronger multipath signals. They are directed towards the wooden cabinets as mentioned in the indoor experiment environment. Figure 4-12 depicts the coherent sum of the matched filter output for the non-LOS transmission in which

signal components coming from two paths can be distinguished. The second path is weaker than the first one by about 6.4 dB. The average delay spread of the ultrasonic channel is estimated to be around 2.7 msec. The channel may be modeled as a wideband fading channel at 1 kHz communication bandwidth. This gives an idea about the order of the delay spread in the indoor ultrasonic channel along with the previous estimate.

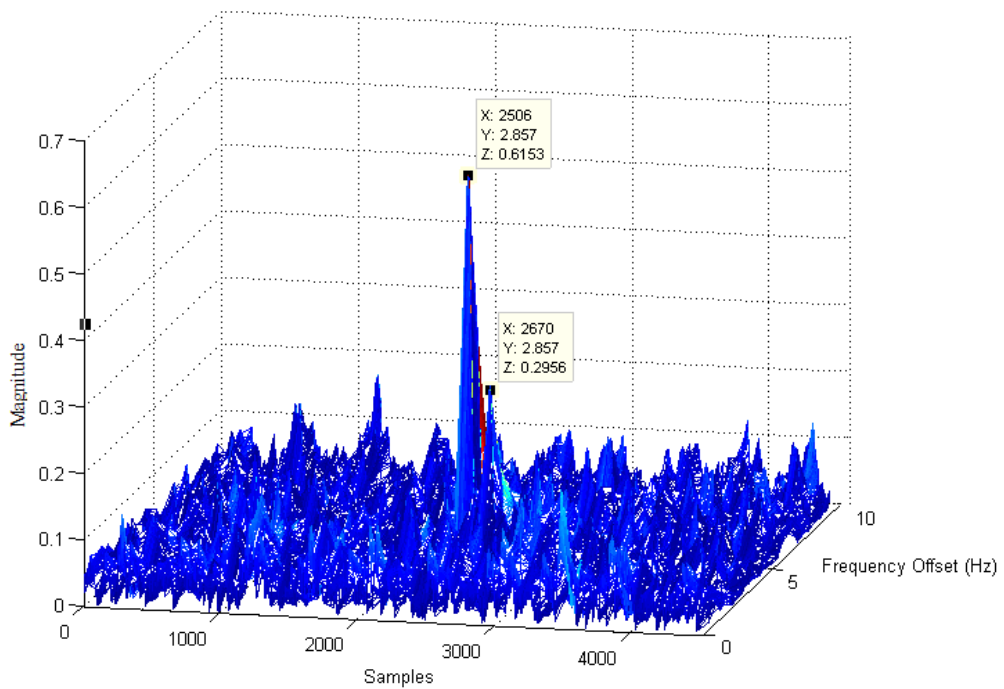


**Figure 4-12** Coherent sum of the matched filter output for a non-LOS transmission in an indoor environment

Similar experiments are performed in an outdoor environment that is convenient for multipath propagation. The transmitted waveform is replaced with the 13-chip Barker waveform considered in the previous section to enhance the observable ranges. Furthermore, two ultrasonic transducers are utilized with 5 cm spacing at the transmitter side. They both send the same waveform with a period of 100 ms, but 50 ms time difference is put between the transmission instances of the two separate transmitters. The channel is recorded for LOS transmissions. At the receiver side, the down-conversion and the matched filtering operations are held

exactly the same as explained in the previous section. Additionally, the matched-filter output is split into delay bins taking into account the transmission period of 100 ms and 45 kHz sampling rate. Therefore in each delay bin, one can expect to observe the responses due to the separate transmitters. The coherent sums of the bins by FFT operation are illustrated in Figures 4-13 and 4-14 corresponding to 8 m and 12 m communication ranges, respectively. Average delay spreads are roughly measured as 15-16 ms for 8 m and 12-13 ms for 12 m separation.

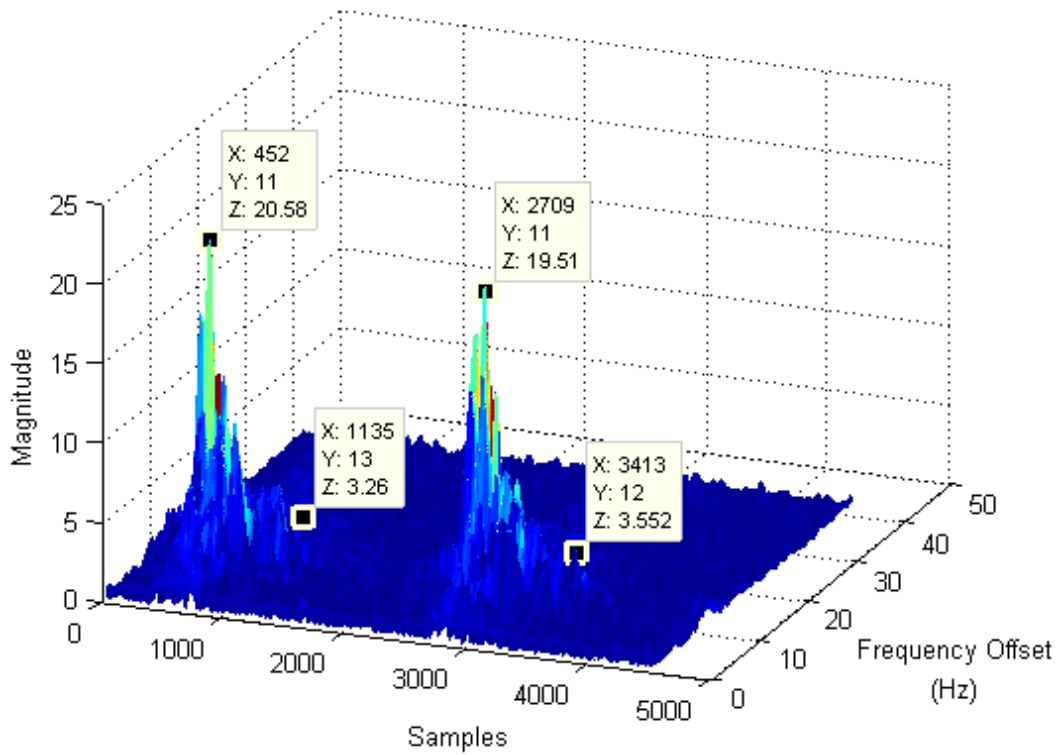


**Figure 4-13** Coherent sum of the matched filter output for an 8 m LOS transmission in an outdoor environment

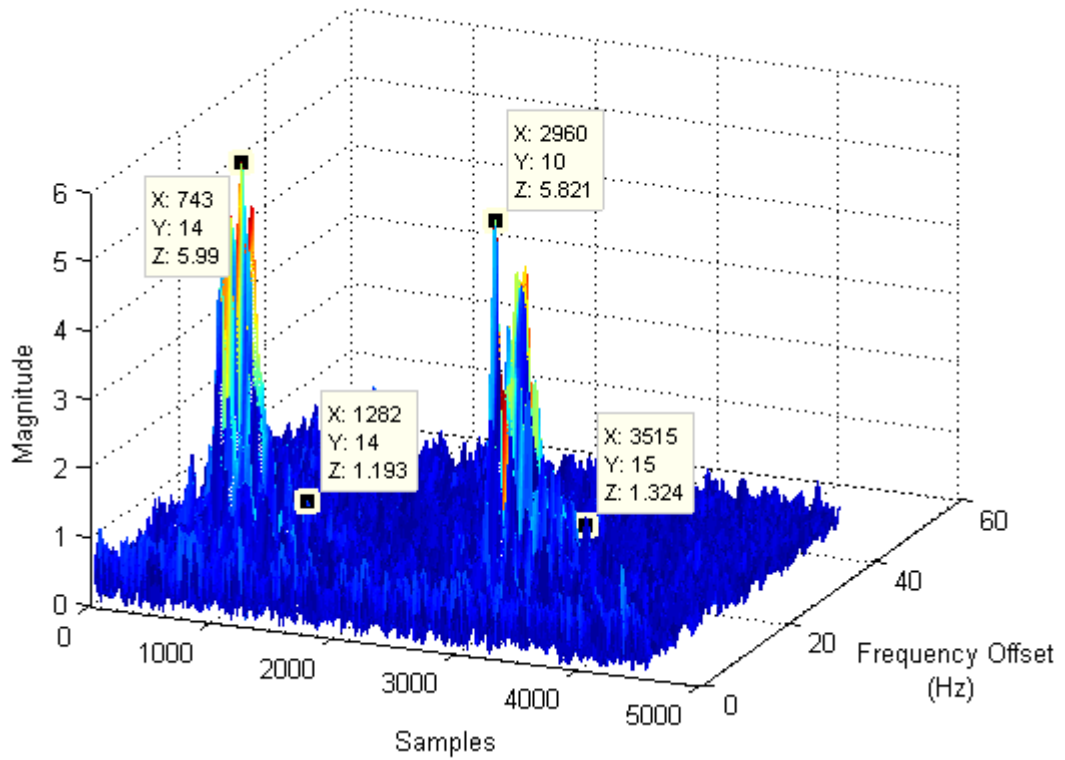


**Figure 4-14** Coherent sum of the matched filter output for a 12 m LOS transmission in an outdoor environment

Figure 4-15 corresponds to the Samples vs. Magnitude display for the 11<sup>th</sup> Doppler bin where the receiver and the transmitters are separated by 8 m. Figure 4-16 depicts the 14<sup>th</sup> Doppler bin that is extracted from Figure 4-14 when the receiver-transmitter separation is 12 m. The rough estimate of the delay spread around 15 ms is more obvious from those 2-D plots.

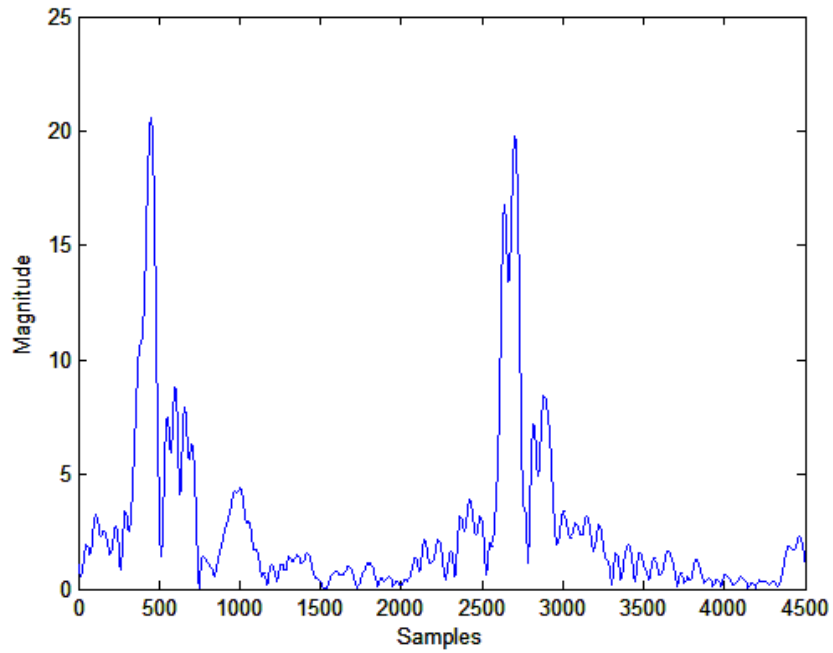


**Figure 4-15** Coherent sum of the matched filter output corresponding to the 11<sup>th</sup> Doppler bin for 8m LOS transmission in the outdoor environment,  $f_s = 45$  kHz

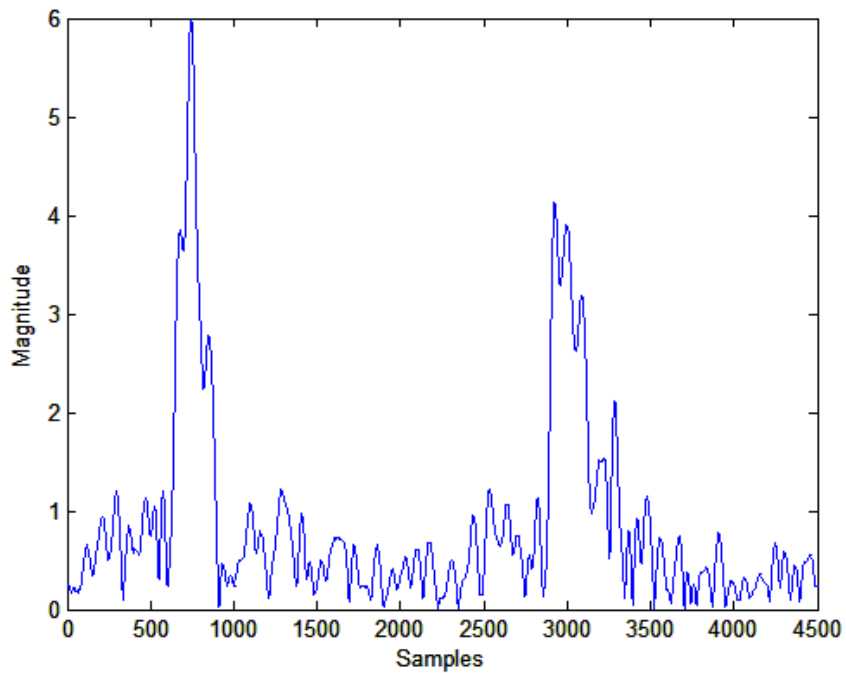


**Figure 4-16** Coherent sum of the matched filter output corresponding to the 14<sup>th</sup> Doppler bin for 12m LOS transmission in the outdoor environment,  $f_s = 45$  kHz

## 4.4 Receiver Correlation

To observe the receiver correlation of SIMO ultrasonic channel, the receivers and the transmitter are located in the indoor experiment environment as described in Section 3.4. The output of the A/D converter is transferred to a PC platform to process the digitized data. The A/D module is adjusted to collect continuous sample points at a rate of 6 kHz for both receiver channels.

Under both LOS and non-LOS conditions, while the transmitter is given a slow circular motion, the spacing between the two receivers is increased from 1 cm to 10 cm. The initial distance between the receivers is set to be 1 cm (about  $1.17\lambda$ ). For each receiver alignment, 6 seconds of continuous observations in average are stored and processed. Since our aim is to observe only the correlation in the channel gains, we can work within a very narrow band. Hence, the transmitted signal is a continuous sinusoidal waveform with 40 kHz frequency and peak to peak amplitude of 10 V.

Rather than using the whole observation, FFT (fast time Fourier transform) is taken in small-sized windows of length corresponding to 25 ms in order to observe the possible variation in the channel gains. Collected data is split into windows, each of which has 150 sample points. The FFT operation is utilized to observe the channel gains at antennas. Figure 4-17 shows the result of this operation where the symmetry of Fourier transform is observed for the real observation. In this figure, the x-axis corresponds to the frequency components that are normalized with the sampling frequency. One may observe the response due to another sinusoidal signal which does not interfere with the signal components in the frequency range of interest. Therefore, in our calculations for the receiver correlation we simply discard those signal components as will be described next.

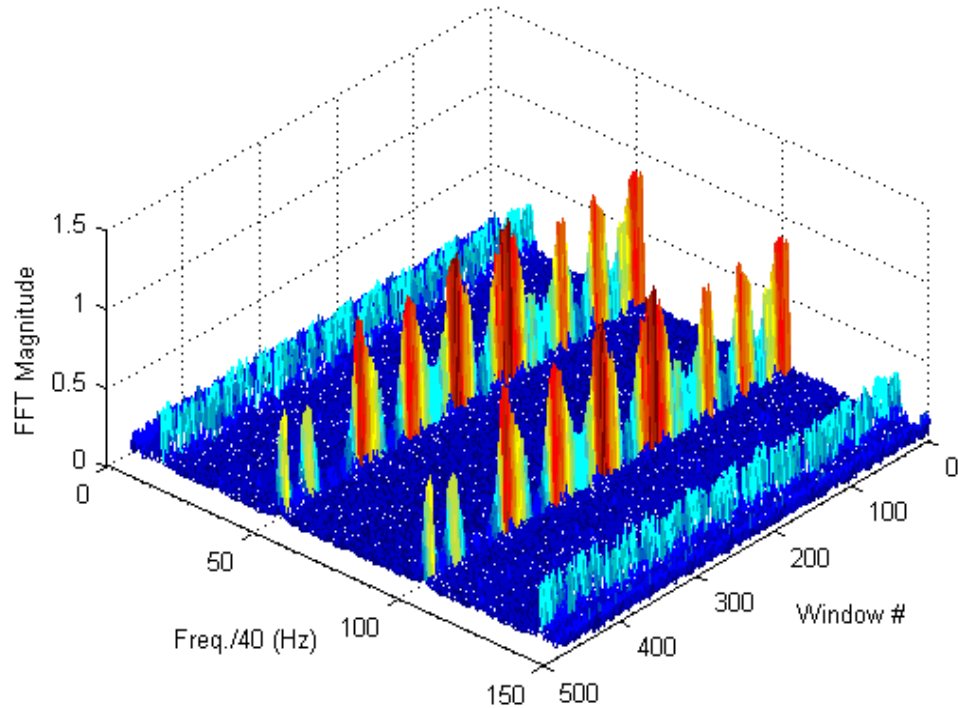


**Figure 4-17** FFT performed on windows of 150 samples, receiver 1 under LOS

We concentrate on the samples in the range of [40,60] since that is the discrete time frequency range that corresponds to 40 kHz with 6 kHz sampling frequency. Figure 4-18 reveals the result when the operations described above are applied to both receivers and the two receivers' data are concatenated in a 3-D plot. Separate amplifiers used for the two channels may be responsible for a portion of the difference in the magnitudes of measurements. Since the metric under consideration here is the correlation between the observations of two transducers, the difference in magnitudes introduced by separate amplifiers does not matter, as long as the relative behavior of two measurements is not violated.

Figure 4-19 displays the peaks points of the receivers at each window. Note that it corresponds to the Window # vs. Magnitude display of Figure 4-18. High correlation between the two signals can be concluded from Figure 4-19.

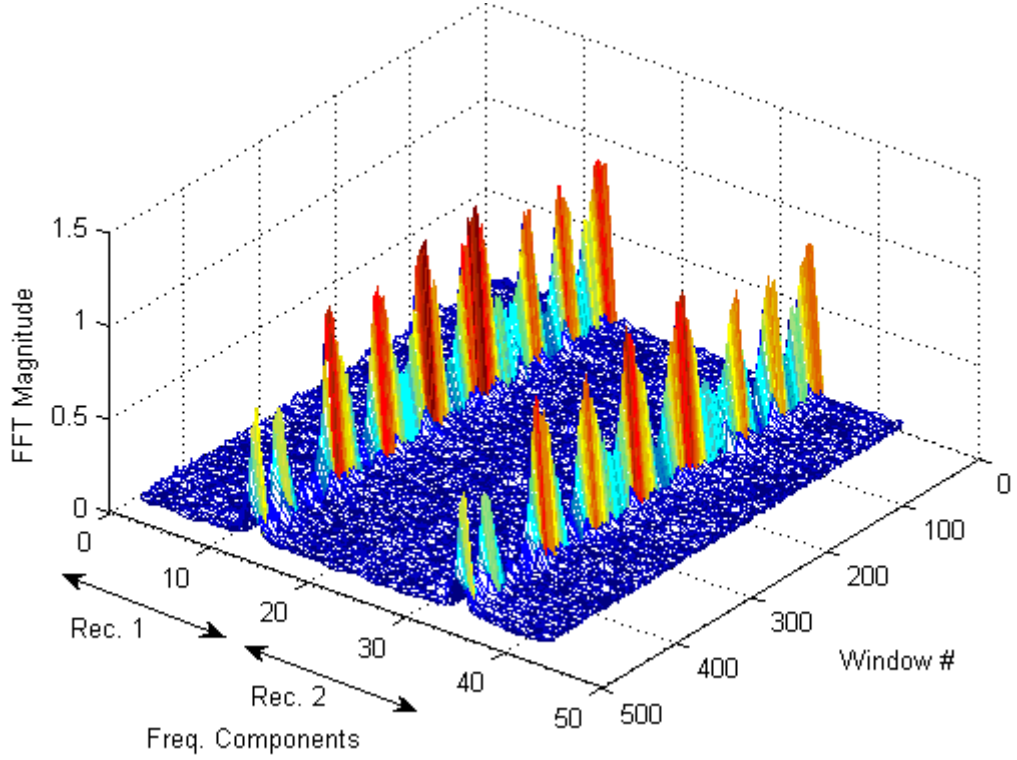


**Figure 4-18** FFT performed on windows of 150 samples, receivers' data concatenated, 1 cm separation between the receivers under LOS

The correlation coefficient  $\rho$  between two complex-valued vectors  $\bar{x}$  and  $\bar{y}$ , whose magnitudes are displayed in Figure 4-19, is calculated to be 0.7128 according to the formula

$$\rho\langle\bar{x},\bar{y}\rangle = \frac{\frac{1}{N} \sum_{i=1}^N x_i y_i^* - \mu_x \mu_y^*}{\sqrt{\frac{1}{N} \sum_{i=1}^N |x_i - \mu_x|^2} \sqrt{\frac{1}{N} \sum_{i=1}^N |y_i - \mu_y|^2}}, \quad (4.7)$$

where the terms  $\mu_x$  and  $\mu_y$  denote the mean of the vectors  $\bar{x}$  and  $\bar{y}$ , respectively and may be expressed as

$$\mu_x = \frac{1}{N} \sum_{i=1}^N x_i \quad (4.8)$$

$$\mu_y = \frac{1}{N} \sum_{i=1}^N y_i . \quad (4.9)$$

This result reveals that there is a strong correlation in the received sequences for the receiver spacing of 1 cm under LOS transmission. Figure 4-20 depicts the corresponding result for non-LOS conditions. Here the correlation coefficient is calculated to be 0.2887 which is enough to fairly assume low correlated reception. Figure 4-21 shows all the calculated correlation values for varying receiver spacing under both LOS and non-LOS transmissions. Note that the signal correlation decreases dramatically as the receiver spacing increases from 1 cm to 2 cm under LOS transmission and that beyond 4 cm of spacing the correlation stays at low values. Under non-LOS transmission scenarios, even 1 cm of receiver spacing is enough for low signal correlation and more spacing still allows almost uncorrelated reception. Those results point out the possible enhancement of communication using diversity techniques with multiple receiving transducers which are very close to each other both under LOS and non-LOS conditions.

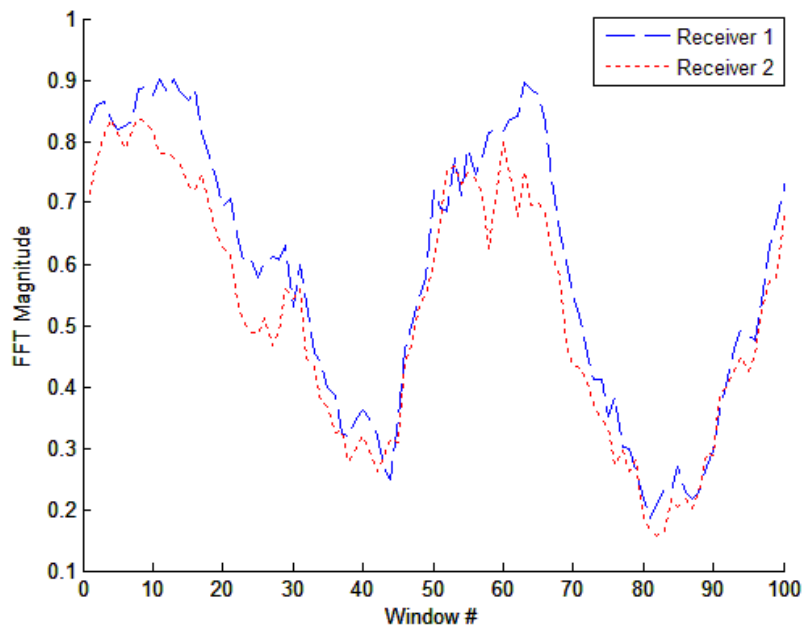


**Figure 4-19** Magnitude of peaks at each window, 1 cm separation between the receivers under LOS

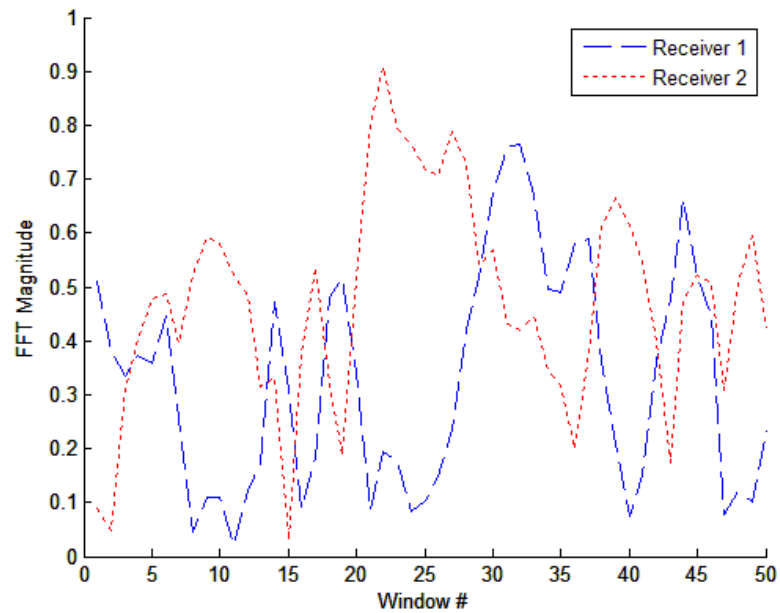


**Figure 4-20** Magnitude of peaks at each window, 1 cm separation between the receivers under non-LOS

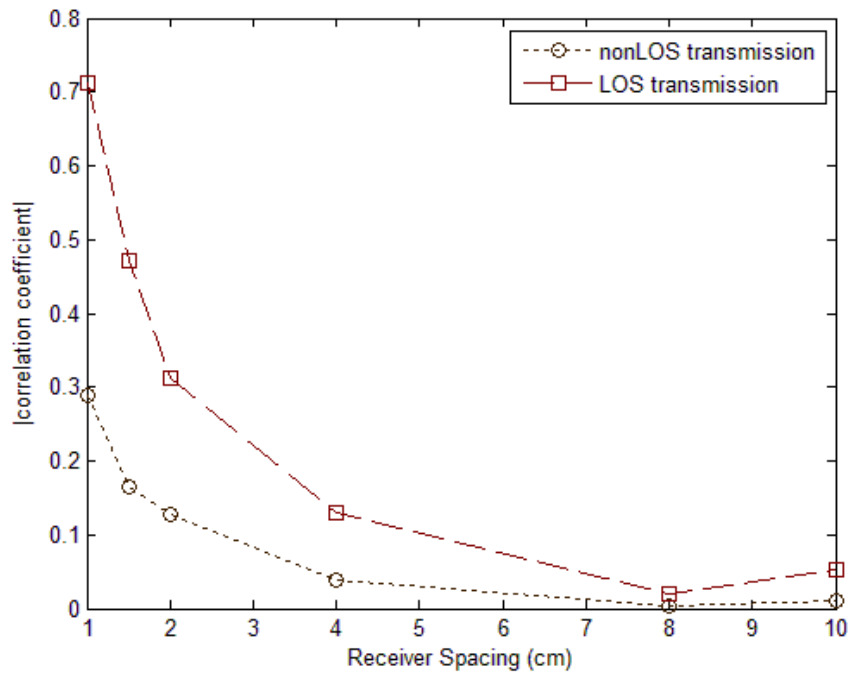


**Figure 4-21** Receiver correlation

## 4.5 Transmission of Modulated Signals

The results in Section 4.4 encourage utilizing a diversity combining. For this purpose, the transmitter and the receivers are located as described in Section 3.4 and their orientations are adjusted to have a strong LOS path. Receivers are separated by 5 cm. In Section 4.2, this separation is found to yield a receiver correlation factor of 0.12 for which it is fair enough to assume uncorrelated reception.

### 4.5.1 Signal Modulation and Demodulation

The modulation scheme for the transmission is selected to be D-BPSK in order not to deal with the small but possibly performance degrading carrier frequency offset. This is an important issue especially in multipath environments.

Differential demodulation, as opposed to coherent demodulation, reduces the load of the receiver node as it does not require a special technique for phase recovery at the receiver side. The previous symbol is used for the phase reference of the current symbol [28]. The conceptual block diagram for this type of modulation is given in Figure 4-22. The differential encoder block performs the binary addition operation given as

$$e_k = e_{k-1} \oplus b_k. \quad (4.10)$$

Hence, sending bit ‘ $b_k = 1$ ’ results in a phase addition of  $\pi$  radians and ‘ $b_k = 0$ ’ in no phase addition. It is contrary to the traditional BPSK in which sending bit ‘0’ corresponds to a specific phase in the resultant analog waveform and bit ‘1’ addition of  $\pi$  radians to that phase, or vice versa. This difference is illustrated in Figure 4-23. In the experiments, bit duration ( $T_b$ ) is set to be 1 ms corresponding a bit rate (R) of 1 kbps. For the ease of experiments, all 0 bits are sent, i.e. no phase change occurs in the transmitted signal.

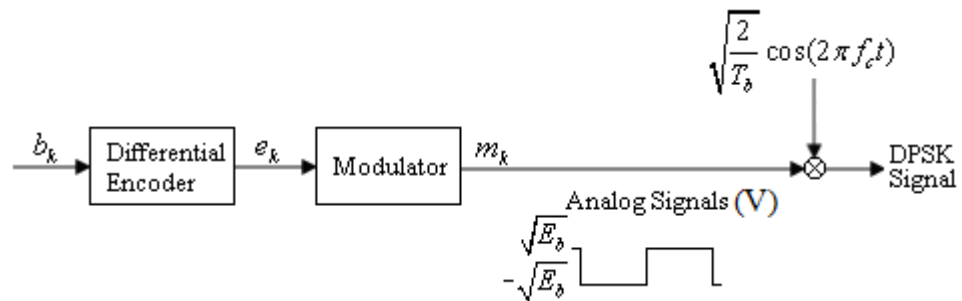


**Figure 4-22** D-BPSK modulation structure

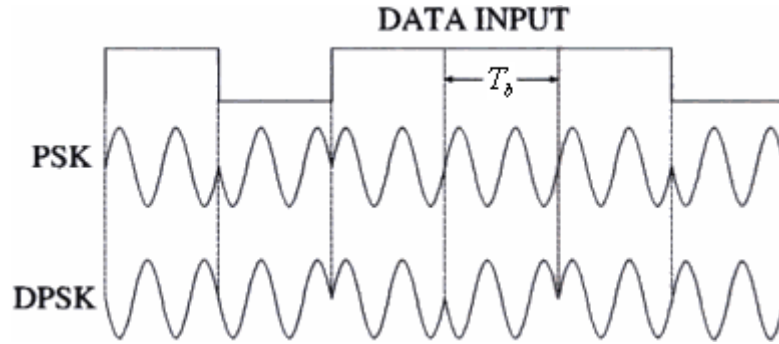


**Figure 4-23** PSK and D-BPSK waveforms [29]

The experiments are conducted under low SNR to be able to observe a significant region of the BER curve. At the receiver side, bandpass signals sampled at a rate of 6 kHz are first down-converted to baseband by I/Q demodulation. The I/Q signals are then passed through the pulse shape matched filter which is rectangular here. To observe the BER at each receiver separately, a decision rule is required to operate on the complex output of the matched filter  $y_k$ . The block diagram for demodulating the D-BPSK signal is depicted in Figure 4-24.

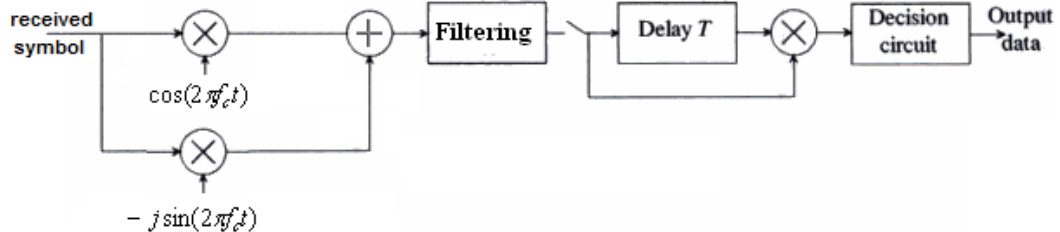


**Figure 4-24** D-BPSK demodulation structure

Since the modulation scheme used herein is differential, the decision rule not only takes into account the current output, but also requires the previous output at the  $(k-1)^{\text{st}}$  time index. The phase difference between the  $k^{\text{th}}$  and  $(k-1)^{\text{st}}$  observations constitutes the decision variable. Assuming additive noise, the output of the matched filter at the  $k^{\text{th}}$  and  $(k-1)^{\text{st}}$  time indices can be expressed as

follows where  $\theta$  is the carrier phase and  $\theta_k$  is the phase angle of transmitted signal at  $k^{\text{th}}$  time index:

$$y_k = \sqrt{E_b} e^{j(\theta_k - \theta)} + n_k, \quad (4.11)$$

$$y_{k-1} = \sqrt{E_b} e^{j(\theta_{k-1} - \theta)} + n_{k-1}, \quad (4.12)$$

$$y_k y_{k-1}^* = E_b e^{j(\theta_k - \theta_{k-1})} + \sqrt{E_b} e^{j(\theta_k - \theta)} n_{k-1}^* + \sqrt{E_b} e^{-j(\theta_{k-1} - \theta)} n_k + n_k n_{k-1}^*. \quad (4.13)$$

In the absence of noise, only the first term in equation (4.13) is nonzero and one would expect to observe no phase difference when bit '0' is sent and a difference of  $\pi$  radians when bit '1' is sent. Among the noise terms,  $n_k n_{k-1}^*$  is negligible relative to  $\sqrt{E_b} e^{j(\theta_k - \theta)} n_{k-1}^* + \sqrt{E_b} e^{-j(\theta_{k-1} - \theta)} n_k$  in the practical SNR ranges of interest and can be neglected [30]. Taking the terms  $e^{j(\theta_k - \theta)}$  and  $e^{-j(\theta_{k-1} - \theta)}$  into the noise Gaussian terms without altering statistical features of  $n_k$  and  $n_{k-1}^*$  yields a new form for equation (4.13):

$$y_k y_{k-1}^* = E_b e^{j(\theta_k - \theta_{k-1})} + \sqrt{E_b} (n_k + n_{k-1}^*). \quad (4.14)$$

Since the phase difference between successive transmitted symbols can be only 0 or  $\pi$  radians, one has to consider only the real part of  $y_k y_{k-1}^*$  to recover information.

$$\text{Re}(y_k y_{k-1}^*) \Big|_{0 \text{ phase difference}} = E_b + \sqrt{E_b} \text{Re}(n_k + n_{k-1}^*) \quad (4.15)$$

$$\text{Re}(y_k y_{k-1}^*) \Big|_{\pi \text{ phase difference}} = -E_b + \sqrt{E_b} \text{Re}(n_k + n_{k-1}^*) \quad (4.16)$$

Hence the decision mechanism for D-BPSK symbols may be expressed as

$$\text{Re}(y_k y_{k-1}^*) \begin{cases} < 0, \text{ bit '1' is sent} \\ > 0, \text{ bit '0' is sent} \end{cases}. \quad (4.17)$$

## 4.5.2 Receiver Diversity Combining

The idea of receiver diversity-combining can be applied for the case in which receivers are separated by a sufficient amount depending on the wavelength of the signal so that the probability of deep fading observed is reduced [28]. The mitigation of severe effects of fading is achieved by receiving signals through independent fading channels without an increase in transmitted power or bandwidth. This type of diversity combining, where multiple receivers are spaced by some range making up an antenna array, is called space diversity. There are several methods in literature to realize receiver diversity-combining such as selection combining (SC), threshold combining (a.k.a. switch and stay combining, SSC), equal gain combining (EGC) and maximal ratio combining (MRC) all of which process the signals that are observed at distinct channels in some way to take the advantage of independent fading [28]. Diversity order is a measure that indicates the change of average probability of error as a function of average SNR per channel [28]. Among the diversity techniques named above, MRC is optimum in the sense that it achieves the best error performance. The important feature of MRC is that the SNR at the output of the combiner is equal to the sum of SNRs obtained from each distinct channel. However, this requires keeping track of the time varying channel gains at different channels. This is not challenging herein due to the offline analysis of experimental data.

MRC technique yields the maximum SNR of the output signal under the assumptions of additive white Gaussian noise which is independent of the signal in channels, locally uncorrelated noise components and locally coherent signal components [28]. Returning to the analysis, making the same assumptions for the ultrasonic channel in our case, it can be shown that the detection rule in equation (4.18) corresponds with two receivers to

$$\text{Re}\left(y_{k,1}y_{k-1,1}^* + y_{k,2}y_{k-1,2}^*\right) \begin{cases} < 0, \text{bit '1' is sent} \\ > 0, \text{bit '0' is sent} \end{cases} \quad (4.18)$$

where  $y_{k,j}$  denotes the observation of the  $j^{\text{th}}$  receiver at the  $k^{\text{th}}$  time index. An alternative representation of  $y_{k,j}$  in terms of the channel gains may be given as follows where  $h_{k,j}$  represent the  $j^{\text{th}}$  channel gain at the  $k^{\text{th}}$  time index:

$$y_{k,1} = h_{k,1}x_k + n_{k,1}. \quad (4.19)$$

Then, the multiplicative term  $y_{k,j}y_{k-1,j}^*$  may be expressed as,

$$\begin{aligned} y_{k,j}y_{k-1,j}^* &= h_{k,j}h_{k-1,j}^*x_kx_{k-1}^* + h_{k,j}x_kn_{k-1,j}^* + h_{k-1,j}^*x_{k-1}^*n_{k,1} + n_{k,1}n_{k-1,j}^* \\ &\approx |h_{k,j}|^2x_kx_{k-1}^* + h_{k,j}x_kn_{k-1,1}^* + h_{k-1,1j}^*x_{k-1}^*n_{k,1}. \end{aligned} \quad (4.20)$$

In equation (4.20), the channel is assumed to be slowly varying so that two consecutive channel gains are supposed to be equal, and the second order noise term  $n_{k,1}n_{k-1,1}^*$  is negligible among other noise terms. SNR can be directly calculated from this expression as

$$SNR_j = \frac{|h_{k,j}|^4 E_b^2}{2|h_{k,j}|^2 E_b N_0} \quad (4.21)$$

$$= \frac{|h_{k,j}|^2 E_b}{2N_0}, \quad (4.22)$$

where transmitted bits at different time indices are assumed to be independent and equally powered. The complex circularly symmetric zero-mean Gaussian noise has variance  $N_0$ . The argument in equation (4.18) can now be rewritten as

$$\begin{aligned} y_{k,1}y_{k-1,1}^* + y_{k,2}y_{k-1,2}^* &\approx (|h_{k,1}|^2 + |h_{k,2}|^2)x_kx_{k-1}^* + h_{k,1}x_kn_{k-1,1}^* + h_{k-1,1}^*x_{k-1}^*n_{k,1} + \\ &h_{k,2}x_kn_{k-1,2}^* + h_{k-1,2}^*x_{k-1}^*n_{k,2}. \end{aligned} \quad (4.23)$$

With the same assumptions defined above the SNR for the signal expressed in equation (4.23) is calculated as

$$SNR_{Total} = \frac{(|h_{k,1}|^2 + |h_{k,2}|^2)^2 E_b^2}{2|h_{k,1}|^2 E_b N_0 + 2|h_{k,2}|^2 E_b N_0} \quad (4.24)$$

$$= \frac{(|h_{k,1}|^2 + |h_{k,2}|^2) E_b}{2N_0} \quad (4.25)$$

$$= SNR_1 + SNR_2. \quad (4.26)$$

The derivation above reveals that the combining method for two channels given in equation (4.18) complies with the key feature of MRC as the SNR at the output of the combiner is the sum of individual SNRs of channel 1 and 2. The 3 dB overhead of D-BPSK demodulation when compared to the coherent PSK demodulation can be observed from individual SNRs and the overall SNR given in equations (4.22) and (4.25), respectively.

Figure 4-25 shows the measured BER for receivers 1 and 2 along with the results obtained when the MRC diversity technique is applied to combine the channel observations. The SNR-axis of the figure does not directly correspond to a signal-to-noise power ratio since we did not measure these in the experiments. Rather than that, we started the measurements with a peak to peak amplitude of 10 mV and recorded the SNR as 0 dB. Then we incremented the amplitude and wrote down the results with an SNR relative to 0 dB with 10 mV amplitude.

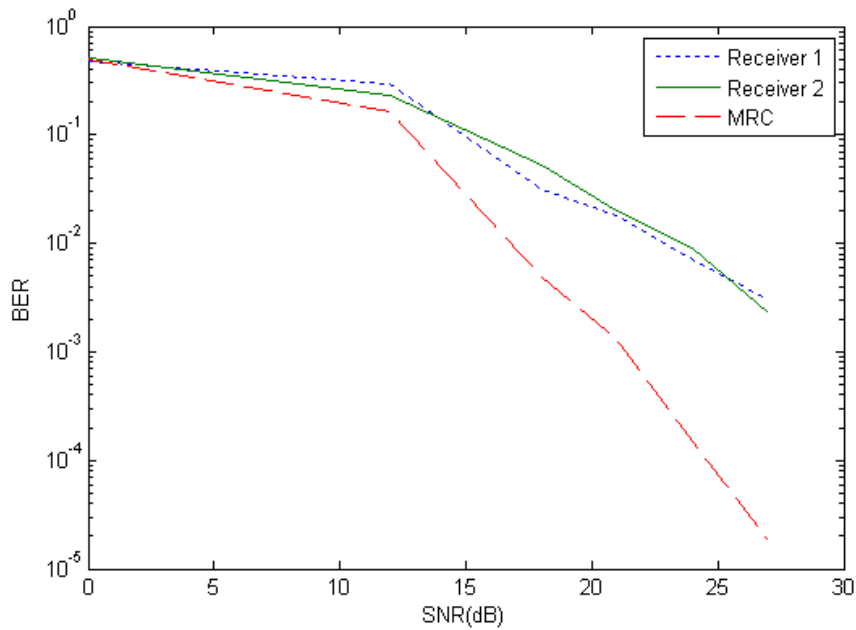


**Figure 4-25** Measured BER for receivers 1&2 and with MRC

The channels are stationary over the duration of a few symbols so that differential demodulation is possible. The duration of channel observation is determined according to a relaxed rule of thumb that to have a reliable estimate of a specific BER value  $P_b$ , one has to transmit at least as many bits as  $10/P_b$ . For instance, the channel is required to be recorded at least 9 minutes to observe a BER of  $2 \times 10^{-5}$  which corresponds to transmission of more than 500,000 bits at a transmission rate of 1 kbps.

From Figure 4-25, it can be stated that BER curves for the two receivers are very close together as expected while the MRC curve decreases sharply after SNR gets above 12 dB. For example, MRC curve assures a BER of 0.0046 at 18 dB; the same rate is attained at about 26 dB for the single receivers. A slope of -1 is observed at high SNR for the single demodulation cases whereas there is a definite slope of -2 for the MRC. This value of the slope shows that a diversity gain of 2 is achieved in the system.

## 4.6 Conclusion

In the experiments performed in an ISI-free environment, no destructive effect of the transducer response is observed with a symbol duration of 1 ms. One may expect to observe interfering effects of the transient response of the electromechanical conversions held at the transducers for shorter symbol durations. The results derived from the experiments performed in a free-space like environment reveal that the channel capacity of around 14 kbps for 1 m transmitter-receiver separation decreases to 1.22 kbps for 20 m separation at 1 kHz communication bandwidth.

The average delay spread of the ultrasonic channel is measured both in an indoor and outdoor environment convenient to model as multipath channels. The indoor analysis is performed under both LOS and non-LOS transmission scenarios and the average delay spreads of the channel are estimated to be in the order of a few milliseconds. At 1 kHz communication bandwidth, the indoor LOS measurements reveals an average delay spread of around 1 ms and the ultrasonic channel can be modeled as a narrowband fading channel. On the contrary, the indoor non-LOS measurements at the same communication bandwidth yields a number of resolvable multipath components leading to the wideband fading model. Average delay spread is estimated to be around 15 ms in an outdoor environment.

The studies regarding the receiver correlation revealed that a small separation between the receivers yields almost uncorrelated reception even under strong LOS conditions. Experimental results agree for the non-LOS condition with further reduction in the separation of receivers. This is an important result in claiming that receiver diversity gain can be achieved by utilizing multiple receiving ultrasonic transducers within a small area. This claim is justified by another experiment in which superiority of the receiver diversity combining method, namely the MRC, over the single branches is presented in terms of the BER performances.

## **CHAPTER 5**

### **DEVICES AND TOOLS FOR IMPLEMENTING AN ULTRASONIC RECEIVER NODE**

This chapter provides the details for some key devices and tools selected before the implementation aspects of an ultrasonic receiver node described in Chapter 6. Both the hardware and software are treated to provide a sense for customizing the relevant features of devices and the tools for the specific application under consideration. The receiver node uses a battery as the power source, two transducers for ultrasonic signal reception, a microcontroller for computation, memory handling, and A/D conversion operation.

#### **5.1 PIC 18F452**

PIC microcontrollers have wide use areas and are preferred mainly due to low cost, wide availability, free development environments, and easy to access experiences. PICs are limited in terms of computational power and memory resources. These limitations restrict the use of PICs in high rate complex applications such as digital signal processing. Despite those restrictions, the simplicity of our communication scheme, the frequency of the ultrasound and the bandwidth of the channel used allow us to employ a PIC for the implementation of a receiver node. Figure 5-1 shows the pin schematics of PIC 18F452 produced by Microchip Technology Inc. that is used in this thesis.

18F452 has many important features that can be summarized as follows:

- 1536 bytes of data memory (RAM) enables much more storage compared to many other series.

- 32 KB of program memory supports larger executable code loading, hence strict optimization is not required to be performed on the binary or hex files as the output of cross-compilation.
- Internal A/D converter with software configurable resolution (8/10 bits) that corresponds to a minimum resolution of 4.88  $\mu\text{V}$  with 5 V reference. This feature allows circuit size reduction, which may be a criterion in some applications, by not requiring an external A/D converter module.
- A/D conversion in sleep mode allows power save and can be referenced in power limited applications.
- 8 analog input channels for A/D conversion enable multiple-channel observation as in our case where the ultrasonic channel's output is to be recorded by two transducers.
- One 8-bit and three 16-bit, a total of 4 independent timers, enable non-sequential control of execution in software when used as source of interrupts.
- Operating frequencies up to 40 MHz, when high speed crystals or resonators are used with PLL, provides a stronger computational power compared to other series of PIC microcontrollers. In this study, the PIC operates at 40 MHz to conform to the timing criterion of the communication scheme.
- 34 digital I/O pins provides a large number of electrical interface to any other peripheral hardware.
- Its low unit price, especially when purchased in order of hundreds makes it applicable for budget critical applications.

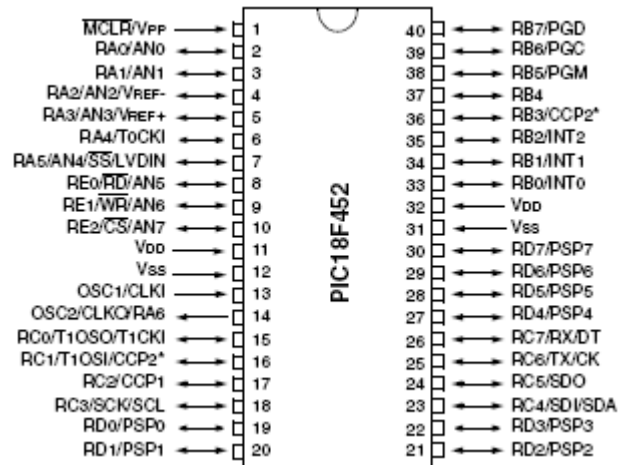


**Figure 5-1** PIC 18F452 pin diagram [31]

### 5.1.1 Loading Software to the Microcontroller

Executables can be loaded on a PIC via a special programmer circuitry. Usually the serial communication line is used for the transmission of executable ‘hex’ file as the RS-232 port is available on majority of computers. However, most recent programmers may also use the USB interface for that purpose. Although such a programmer circuit may be constructed from the instructions in the microcontroller’s datasheet, programmers for many ICs are commercially available. The figure below shows the JDM serial programmer which is able to program a number of microcontrollers including PIC 18F452.

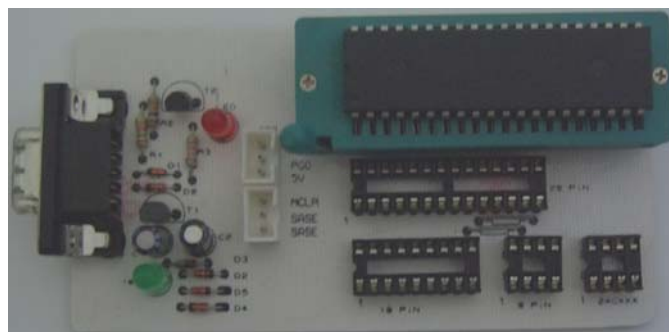


**Figure 5-2** PIC 18F452 serial programmer

At the computer side, a specific software is required to interface with the serial programmer. IC-Prog is a popular and free tool that supports many of the microcontrollers with an easy control over program and EEPROM memory. It is compatible with many of the programmer boards including the JDM programmer. The following screenshot depicts a snapshot of IC-Prog configured for the JDM programmer and PIC 18F452.

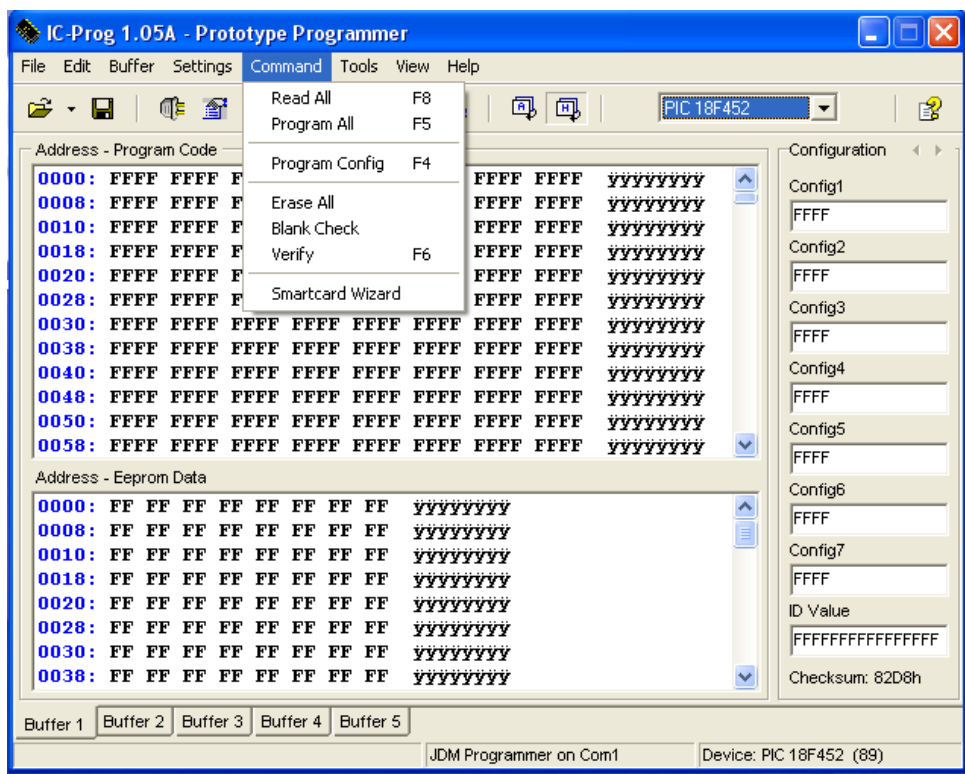


Figure 5-3 IC-Prog serial programmer software

### 5.1.2 Initialization Options

There are many options on the PIC 18F452 that can be selected through precompiler directives. They are called device fuses and can be controlled with the keyword '#fuses' in the source code. The following table indicates the fuses that are referenced in this study along with their descriptions obtained from the compiler help menu.

**Table 5.1** Fuse options used on the microcontroller

<b>#fuse keyword</b>	<b>Description</b>
H4	High speed oscillator with 4xPLL
NOOSSEN	Oscillator switching is disabled
NOPROTECT	Code is not protected from reading
NOBROWNOUT	No brownout reset
NOWDT	No watch dog timer
NOSTVREN	Stack full/underflow will not cause reset
NOLVP	No low voltage programming, B3 pin is used for I/O
PUT	Power up timer

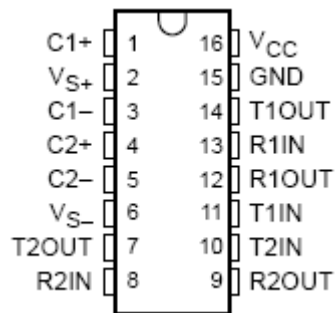
Likewise, A/D resolution and RS-232 serial communication properties are handled with special directives. ‘#device’ is used to set A/D converter resolution to 10 bit. ‘#use rs232’ is used to assign rs232 transmit/receive pins with the serial baud rate. Furthermore, I/O direction for the pins used for A/D conversion and serial transmit and receive should be set by the ‘set\_tris’ function.

### **5.1.3 RS-232 Serial Channel Communication**

Before proceeding with the implementation of software, it is crucial to provide a means for communication to the microcontroller for debugging and logging purposes. By its own, a PIC microcontroller provides I/O ports to interface with any other peripheral hardware but their use depend on the design and the selected communication scheme. The RS-232 serial channel communication is perhaps the most preferred communication scheme between a standard personal computer and such microcontrollers. For this reason, this section is devoted to the RS-232 communication details referenced in this thesis. This infrastructure is constructed before any software related implementations.

PIC 18F452 includes a USART (Universal Synchronous Asynchronous Receiver Transmitter) module capable of operating in one of the asynchronous-full duplex, synchronous-master-half duplex or synchronous-slave-half duplex modes [31]. The asynchronous mode is mainly used for communicating with personal computers whereas synchronous configuration provides communication with other peripheral devices such as external A/D or D/A converters, serial EEPROMs, etc. Referring to the pin schematics depicted in Figure 5-1, pins 25 and 26 can be utilized for RS-232 transmit and receive purposes, respectively.

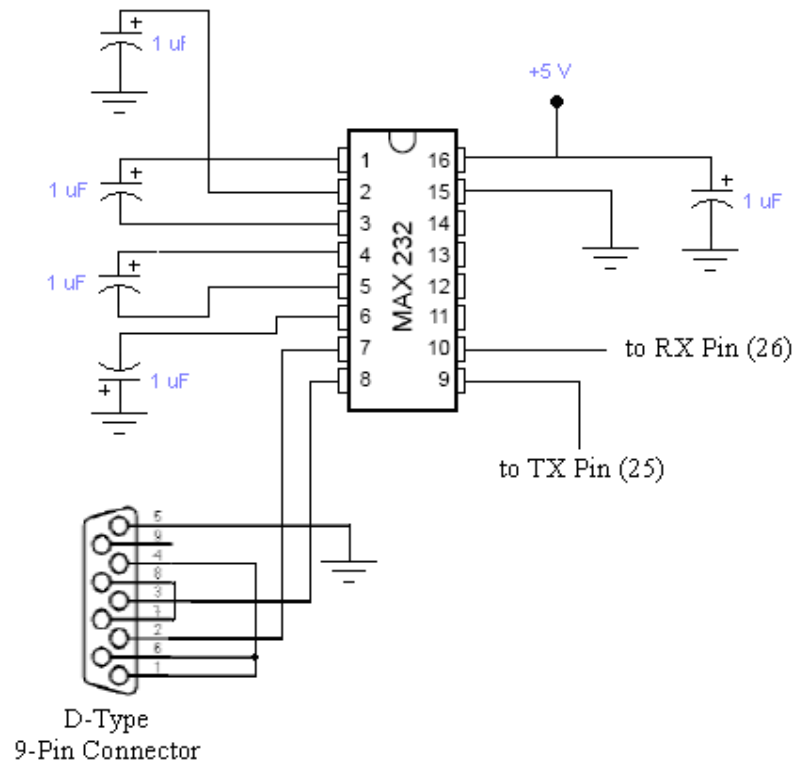
In RS-232 communication, binary logic states are represented by electrical signals so that binary '0' and binary '1' correspond to voltages usually in the ranges [+3V, +12V] and [-12V, -3V], respectively. Therefore, to transfer serial data from PIC to PC, TTL voltage levels (0-5V) must be converted into RS-232 voltage levels. Conversely, RS-232 inputs must be converted into TTL voltage levels to be able to send data from PC to the microcontroller. This requires a level converter IC, namely MAX232, which can be driven with a single +5 V supply.



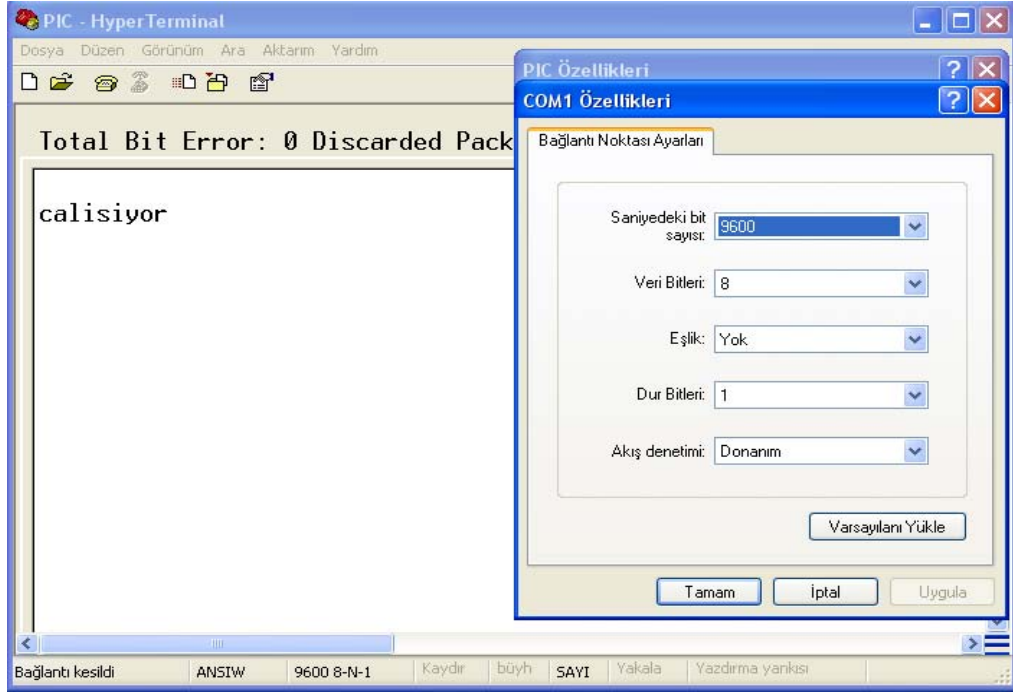
**Figure 5-4** MAX232 pin diagram [32]

Figure 5-5 summarizes the necessary connections to be made between PIC18F452 and MAX232 along with the circuit elements to build a typical working application. In serial communication, the data transfer rate in bits per second is referred to as baud rate. The baud rate is software selectable for the

microcontroller. A rate of 9600 bauds suffices for logging and debugging purposes. This rate entails an agreement between the both ends of the serial line. At the PC site, Hyper Terminal application can be used to listen as well as pass messages from/to the PIC. Other parameters to be adjusted can be followed from the screenshot that is taken from that application.



**Figure 5-5** PIC18F452 and MAX232 connections for a typical application



**Figure 5-6** HyperTerminal configuration for serial communication

#### 5.1.4 A/D Conversion

PIC 18F452 has an internal multi-channel A/D conversion module and a multiplexer for channel selection among eight ready to use possible channels. It provides 10 bits resolution hence enabling to sense at least 4.88 mV (for +5 V reference) deviations in the channel depending on the reference voltage used. For instance, the input signals that are in the range  $[0, V_{DD}]$  are supported for conversion when  $V_{DD}$  (+5 V) is used as reference providing 4.88 mV (5V/1024) precision. This resolution can be improved, as may be necessary in a case where the channel input never exceeds  $V_{DD}$ , by reducing the observation interval in the cost of using another power supply as reference voltage. In this scheme, the pin that is connected to the additional power supply is assigned as reference through the software. Due to the overheads of introducing an additional power supply and dedicating an I/O pin just for A/D reference purposes, in this study  $V_{DD}$  is used for A/D conversion reference voltage.

In [31], timing issues for acquisition of analog data and A/D conversion for PIC18F452 are detailed with many considerations such as input source impedance and capacitance, holding capacitor charging time, amplifier settling time and so on. Furthermore, A/D conversion clock is suggested to be selected to ensure a minimum conversion time per bit of 1.6  $\mu$ s. Hence, with 40 MHz system clock employed in this study, A/D conversion clock is set to be 1/64 of the system clock. From a practical point of view, the tests, which are executed on a single channel to observe the maximum achievable sampling rate with the setup in hand, revealed a minimum sampling time of around 11  $\mu$ s for 10 bit resolution, hence giving a sampling rate of approximately 90 kHz. It is worthy to state that, the rate is highly dependent on the input impedance and Microchip recommends 2.5 K $\Omega$  input impedance for analog sources at most. This rate is achieved for the case no other operation rather than A/D conversion is performed on the PIC. If it is applicable to sample a number of inputs and then process them as a whole and the processing time is tolerable, this rate can be used in the applications. However, a lower sampling rate must be chosen to continuously sample and process the input data before the next sample is acquired as it is the case in this study where 6 kHz sampling rate is intended.

To sum up the configuration of A/D conversion, analog channels AN0 (pin 2) and AN1 (pin 3) are used for the two receiving channels. The conversion clock is set to 1/64 of the 40 MHz system clock to ensure a minimum conversion time per bit of 1.6  $\mu$ s.  $V_{DD}$  is used as voltage reference at both channels and the resolution is set to be 10 bits so that 4.88 mV input voltage deviations can be sensed. Since the two channels share the same capacitance holding circuitry, reading the other channel requires a multiplexing operation first. The compiler recommends a short time delay around 10  $\mu$ s between a channel change and read for successful A/D conversion.

### 5.1.5 Sampling Rate Adjustment

Normally, statements in the code are executed sequentially in microprocessors. However, some applications require more complex execution control as reaction to particular conditions. Upon detection of such an unusual case, the current state of the running software is stored at memory and execution jumps to a different location. Having executed the particular statements at that location, the control returns back to the statements suspended previously and the state of the software is restored. In PICs, sequential execution is altered by the use of interrupts. Interrupts may be raised as a result of timer overflow, on completion of A/D conversion, on reception of a byte from serial line, etc.

PIC 18F452 has one 8 bit and three 16 bit, hence a total of four timer modules. They can be used as the source of timer interrupts, especially to realize regular intervals. Timer interrupt is raised when the counter associated with that timer overflows. For instance, for 16 bit Timer1 module, an interrupt is raised as the counter falls from 65535 to 0. If the counter is initialized to be 0, an interrupt occurs after 65536 increments. The following formula gives the interrupt rate for a 16 bit timer module in which a prescaler is used to reduce the system clock frequency so that the counter is not necessarily incremented at each clock cycle:

$$f_s = \frac{\text{clock frequency}}{4 \times \text{prescaler} \times 65536} \quad (5.1)$$

With the prescaler set to 1 and 40 MHz clock frequency, 152 Hz interrupt rate is achieved. To achieve higher rates, the timer is set to a nonzero value each time the timer interrupt is raised. The following generalized formula can be used to calculate the interrupt rate given the start of counter increment, or conversely, the initial timer value to be used given the desired rate.

$$f_s = \frac{\text{clock frequency}}{4 \times \text{prescaler} \times (65536 - N)} \quad (5.2)$$

Hence, with the prescaler set to 1 and 40 MHz clock frequency, 6 kHz interrupt rate can be achieved by setting the timer to 63870 each time a timer interrupt occurs. This corresponds to incrementing the counter 1666 times.

PIC 18F452 has two capture/compare/PWM (CCP) modules. In a study conducted at Microchip Technology Inc., CCP modules for PIC18F452 are reported to be reliable to sample analog data at regular intervals [33]. The module is used in special event trigger compare mode and initialized with a 16 bit value. Timer1 counter is automatically compared to that value at each increment. Whenever a match occurs between the CCP and the Timer1 counter an interrupt is raised. Upon the reception of the CCP interrupt, the software starts the A/D conversion operation that is guaranteed to be at regular intervals.

Although the mathematical analysis above on sampling rate adjustment provides us the necessary parameters for CCP module initialization, it should be tested on the actual hardware to observe a desired behavior. For instance, imperfections in manufacturing can prevent generating an exact clock rate that is assumed in software. This deficiency is sufficient alone to violate the aimed sampling rate. An iterative fine tuning activity here is performed to obtain a 6 kHz interrupt rate. For instance, it is straightforward to write some sort of test software that counts the CCP interrupts and gives a sign out when it counts up to 6,000,000. Meanwhile, elapsed time should be recorded to observe the mismatch between the desired and current rate. In this configuration, 1  $\mu$ s mismatch in the sampling period yields 6 seconds of error. As more interrupts are counted, the accuracy of fine tuning increases. Having performed a few iterations, it is found that initializing the CCP2 module to be 1626 yields the 6 kHz sampling rate.

This experimentally found sampling rate can be further analyzed in accordance with the Nyquist sampling criteria. For this reason, a 3 kHz sinusoidal is directly fed to the A/D conversion pins of the microcontroller from a signal generator. With 6 kHz sampling rate, one should expect to see a single peak response in the middle due to overlapping of symmetric components at the output of FFT

operation. Deviations from the 6 kHz sampling rate would prevent this behavior as it is seen in Figure 5-7 in which the responses for the mathematically and experimentally found sampling rates are compared. This double check increases the confidence at the sampling rate obtained by initializing the CCP2 module to 1626 so that the samples can be collected regularly at the rate of 6 kHz.

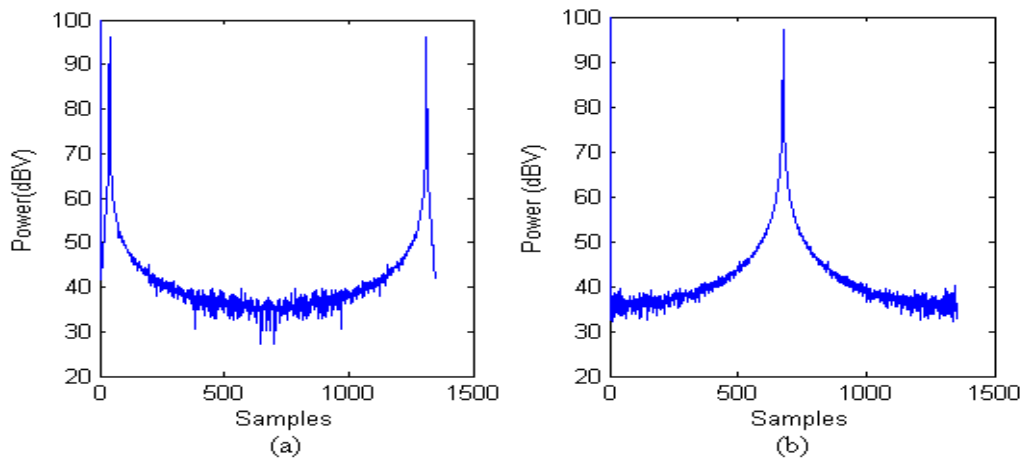


**Figure 5-7** FFT operation performed on 1350 samples collected from a 3 kHz sinusoidal at (a) mathematically found sampling rate (b) experimentally found sampling rate

Figure 5-8 depicts the flow chart which indicates a number of activities put in an order within the designed communication scheme. 6 kHz sampling rate requires the time interval between successive CCP interrupts to be around 166.67  $\mu$ s, and note that this time interval is shared among the two channels for the execution of algorithms on separate channels. Wait block in the figure is required to isolate the second time slot from the first one so that regular samples from the second channel can be obtained as well, as long as the process in the first time fit into 83,33  $\mu$ s. This isolation here is especially important since there is no guarantee that the processing of the first channel is accomplished within the same time interval at each execution. Processing details will be treated in the subsequent sections.

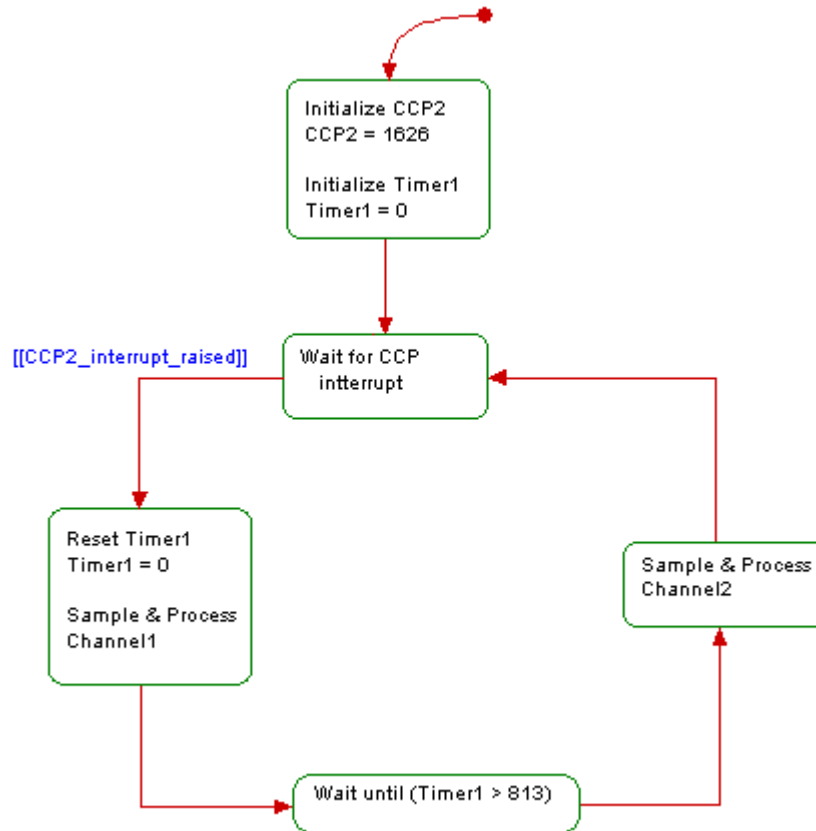


**Figure 5-8** Flow chart for sampling the two analog channels

## 5.2 Power Supply

A 9 V battery is used to supply power to the microcontroller. Typically, PIC 18F452 operates at 5 V. It is reported to have low power consumption at 5 V and 4 MHz clock frequency; it is driven with less than 1.6 mA. However, as the clock frequency increases to 10 MHz with internal PLL activated to provide 10 MIPS (mega instructions per second) in a special mode used in this study, driving current increases up to 16 mA at maximum [31]. A 3-pin Voltage regulator IC LM7805, whose pin diagram is depicted in Figure 5-9, is employed in order to provide voltage stability around 5 V and protection against high voltage at the control voltage input of the microcontroller. The use of such a regulator unit in the circuit driving the PIC is important while working with several batteries and power supplies in the development phase: Keeping the input voltage constant and stable, response due to electrical components is more likely to be deterministic. In

other words, microcontroller's operations are attempted to be kept at a level which offers a steady environment for software development.

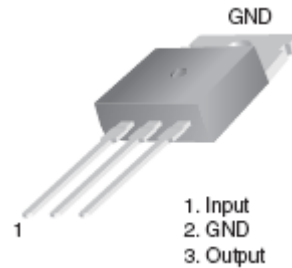


**Figure 5-9** LM7805 pin diagram [34]

### **5.3 Programming Language and Compiler**

For the implementation of real time software that will run on the microprocessor, the C programming language is preferred over the Assembly-language. Even though a program written in Assembly is asserted to execute faster, the C language provides easy development and maintenance activities especially when there is some simulation code such as written in MATLAB in hand. The C language grants a more developer-friendly environment important especially in adapting the updates and modifications that are likely to occur in the proposed algorithms. For this purpose PCW C Compiler IDE (Integrated Development Environment) v.3.26 is used. The output of the compiler is a '\*.hex' file that can be directly loaded into the PIC's program memory.

```

PCW C Compiler IDE
File Project Edit Options Compile View Tools Debug Help
Microchip PIC18
sample6000hz_no_decimation_2_channel_optimizeddetectionandreception_for100bit_observe_ber.c

{
while(newInt == 0)
{;}

ADC_Value1 = read_adc();
set_adc_channel(1);

if(PeakDetected == 0)
{
PeakEstimate_real1 = PeakEstimate_real1-window_signal_I1[currentPointer];
PeakEstimate_imag1 = PeakEstimate_imag1-window_signal_Q1[currentPointer];

switch(samplesHold)
{
case 0:
window_signal_I1[currentPointer] = ADC_Value1;
window_signal_Q1[currentPointer] = 0;
break;
case 1:
window_signal_I1[currentPointer] = 0 - (ADC_Value1>>1);
window_signal_Q1[currentPointer] = ADC_Value1 - (ADC_Value1>>3);
break;
case 2:
window_signal_I1[currentPointer] = 0 - (ADC_Value1>>1);
window_signal_Q1[currentPointer] = (ADC_Value1>>3) - ADC_Value1;
break;
}

ntemp = window_signal_I1[Pointer_12_Past]-window_signal_I1[Pointer_6_Past] -
PeakEstimate_real1 += ntemp + ntemp + window_signal_I1[currentPointer];

ntemp = window_signal_Q1[Pointer_12_Past]-window_signal_Q1[Pointer_6_Past] -

```

**Figure 5-10** Screenshot of the PCW C Compiler IDE

When developing software on a computationally limited processor it is important to continuously refer to the processor datasheet as well as the compiler manual. As an example, to ensure real-time operation, one at least must know the time elapsed in specific instructions. Even the simple mathematical operations can occupy a significant amount of time which is to be specially managed to obtain intended results. Table 5.2 provides a means for the duration of mathematical operations likely to vary depending on the memory banks used in the microprocessor [35].

**Table 5.2** Durations of mathematical operations for 18F452 operating at 40 MHz and for various variable types (integers are unsigned by default) [35]

	int8	int16	int32	float
+	0.3 $\mu$ sec	0.4 $\mu$ sec	0.6 $\mu$ sec	51.3 $\mu$ sec
-	0.3 $\mu$ sec	0.4 $\mu$ sec	0.6 $\mu$ sec	52.3 $\mu$ sec
*	0.4 $\mu$ sec	3.2 $\mu$ sec	22.2 $\mu$ sec	35.8 $\mu$ sec
/	11.3 $\mu$ sec	32 $\mu$ sec	106.6 $\mu$ sec	144.9 $\mu$ sec
exp()	*	*	*	510.4 $\mu$ sec
ln()	*	*	*	644.8 $\mu$ sec
sin()	*	*	*	698.7 $\mu$ sec

Note from table above that, from variable type point of view, 8-bit integer operations performs much faster than any other types. For instance, a simple addition operation takes 51.3  $\mu$ sec when performed on float variables which is 171 times larger than that on 8-bit integers. This is a major constraint in scientific calculations in which most of the formulas require floating point operations. This problem is specifically aimed by many compilers as fixed-point operation support or must be handled manually at the cost of accuracy losses. To this extent, it is desirable to replace time-consuming floating point operations with fixed-point or decimal operations when accuracy loss is graceful, algorithms and software should be more precisely designed and implemented by keeping the properties of the hardware and compiler in mind.

Another important measure to notice from Table 5.2 is that, the operation time for integer variables may increase in a non-linear fashion as the number of bits increase. For instance, an 8-bit integer multiplication lasts 0.4  $\mu$ sec whereas a 32-bit integer multiplication requires about 9.5 times more: 106.6  $\mu$ sec. This forces the developers to choose smallest-sized types to store and manipulate variables even when RAM can still provide space for larger-sized variables. For this reason, it is important to check on each variable to determine its possible range in

terms of upper and lower bounds, hence giving rise to deciding which type to use. All the available standard data types supported by the PCW compiler are shown in Table 5-3.

Optimizations can be helpful in enhancing the run-time performance and attending to the time constraints set by the nature of the problem under consideration. Indeed, the most significant optimization can be attained by reconsidering the algorithm. Costly steps of the current version of an algorithm may not be required at all with another solution. For instance, the algorithm may not require absolute values, rather may work with relative values which can remove costly type conversions. Having decided on the algorithm, timings may depend on different implementations. Considering programming language specific features and the compiler in hand, more efficient implementations may always be possible. For instance, division by a power of 2 can be performed much faster by bitwise shift operations. Observing the trade-off between memory use and performance, even more improvement may be present. For instance, costly run-time trigonometric or exponential computations can be removed by constructing a look-up table in advance and referencing at run-time. If loss of accuracy to some extent is appreciable in the problem, replacement of exact computations by approximations may provide enhancement on the performance. These simple but useful methods make the whole operation realizable in our case that sampling two channels at a rate of 6 KHz, manipulating the digitized data, performing digital filtering operations, and using an adaptive-threshold based decision algorithm all fit into  $166.67 \mu\text{s}$  so that 6 kHz sampling rate is supported.

**Table 5.3** Standard data types supported by PCW compiler

<b>Type</b>	<b>Size</b>	<b>Range</b>
short int or int1	1 bit	0 or 1
(unsigned ) int or (unsigned) int8	8 bits	0 to 255
signed int or signed int8	8 bits	-128 to +127
char	8 bits	ASCII character, 0 to 255
(unsigned) long int or (unsigned) int16	16 bits	0 to 65535
signed long int or signed int16	16 bits	-32768 to 32767
(unsigned) int32	32 bits	0 to 4294967296
signed int32	32 bits	-2147483648 to 2147483647
float	32 bits	About $-3 \times 10^{-38}$ to $3 \times 10^{-38}$

## **CHAPTER 6**

### **THE IMPLEMENTATION OF A DOUBLE TRANSDUCER ULTRASONIC RECEIVER NODE**

This chapter is devoted to the realization of packet detection and differential demodulation algorithms on the target platform, PIC 18F452. Many implementation issues, especially timing concerns, are directly aimed in this chapter justifying the efforts on optimizing the algorithms applied. For packet detection, noise level at the channel is observed continuously to adapt a threshold mechanism in order to provide a constant false alarm rate similar to the CFAR method mostly used in radar applications. Furthermore, the selection diversity combining scheme is implemented to attain diversity gain from the two receivers. An implementation for the D-BPSK demodulation scheme is also given and finally, important system performance metrics such as false alarm and bit error rates are provided.

#### **6.1 Packet Detection**

Packet detection is an important aspect of communication. In practice a probing pilot sequence is usually provided ahead of the actual data to be sent. At the receiver side, this preamble can be used to determine the existence of a transmission as well as to observe important channel statistics. In Chapter 4, the 13-element Barker code is introduced which realizes a peak-to-peak mainlobe-sidelobe ratio of 13. This gain, which is also called the spreading gain, is especially useful for enhancing the detection range. In this section, implementation details, necessary to detect the preamble, of processing the ultrasonic signals coming from two channels are explained. The implementation

finally gives rise to determine the overall data packet structure to be used in the actual data transmission. The following block diagram summarizes the primitive operations held for packet detection.

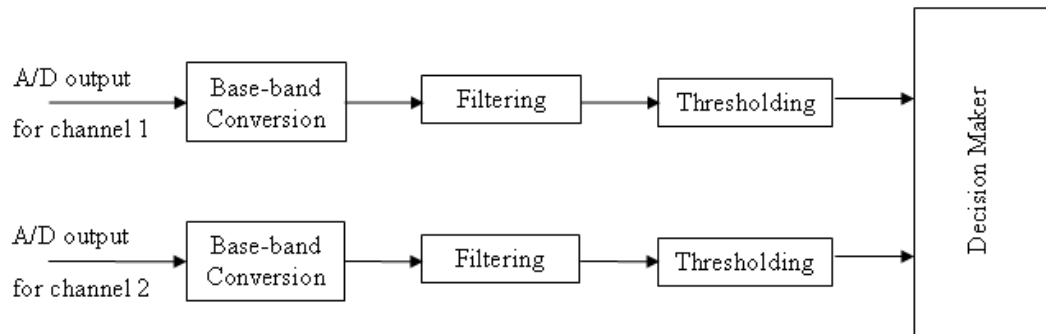


**Figure 6-1** Block diagram for packet detection

Recall that one of the primary goals in this study is to provide a means for achieving receiver diversity gain at the ultrasonic channel. In Chapter 4, the MRC diversity technique is applied for combining ultrasonic signals obtained from two ultrasonic transducers and analysis results are presented. Selection Combining (SC) is another combining method in which the combiner output is the input signal that has the largest SNR. Therefore, in this technique, after observing SNRs at the different transducers, only one transducer, which yields the highest SNR, is used at a time to decode the incoming data packet. As noticeable from the block diagram depicted in Figure 6-1, individual channels are treated separately and run simultaneously and continuously to make a decision on packet detection.

The use of the SC diversity method in the implementation phase can be justified as follows. The first reason is that it is practically easier to detect the highest SNR among all channels and then proceed only with the channel yielding the maximum SNR. Second, since only one channel is used at a time, coherent and differential modulation schemes can be used with no effort required on co-phasing of different branches. And finally, from average bit error rate point of view, not much performance difference is reported in [28] between SC and MRC

with 2 receivers. Figure 6-2 shows the average bit error probability vs. average SNR for MRC and SC for a number of receivers involved when BPSK modulation scheme is in use in an i.i.d. Rayleigh fading channel.

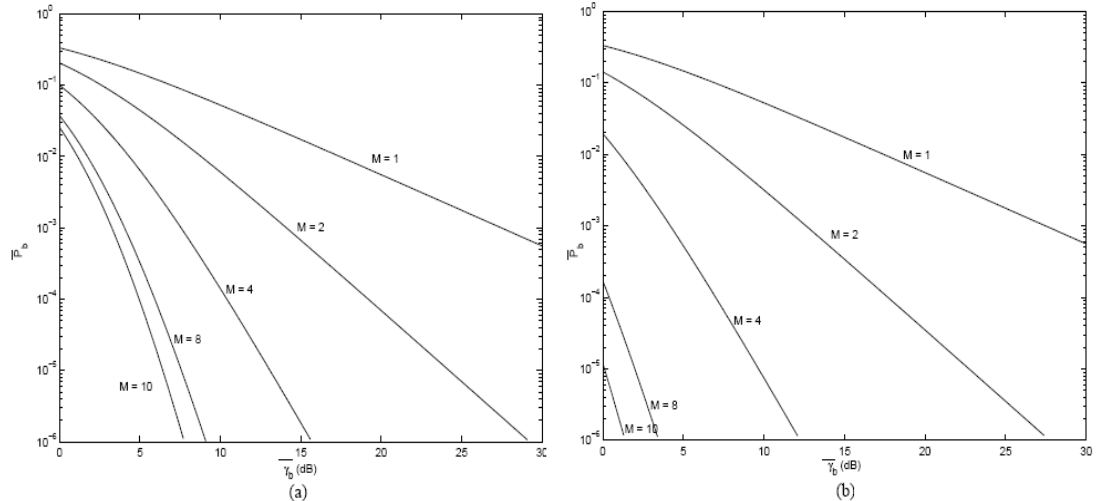


**Figure 6-2** Average bit error probability vs. average branch SNR in i.i.d. Rayleigh fading channel for a number of receivers for (a) SC (b) MRC [28]

### 6.1.1 Down-Conversion

Operation on the received data starts with a passband to baseband conversion. Note that A/D output is a 10 bit number, 0 mapping to ground level and 1023 to 5V. Since there is no 10 bit standard data type, it is stored in 2 byte variables. There is no practical reason to convert back this scalar into floating point voltage. First, operations on integer data types are much faster than the floating point data types as explained before. Second, this conversion just changes the units of variables which are not important when operating on relative values rather than absolute ones. Finally, PICs are limited both in terms of memory and CPU and such a conversion would be a waste of system resources.

The 40 kHz ultrasonic signals are sampled at 6 kHz for the both channels using the bandpass sampling theorem. Calculation of the *in-phase* and *quadrature*

components of the baseband signal requires multiplication with trigonometric expressions  $\cos(2\pi f_c t)$  and  $\sin(2\pi f_c t)$ . Noting the periodicity in the results when center frequency and time values are substituted into the expressions, costly run-time trigonometric functions can be removed since

$$\cos(2\pi f_c t) = [1, -0.5, -0.5, 1, -0.5, -0.5, \dots] \quad (6.1)$$

$$\sin(2\pi f_c t) = [0, -0.866, +0.866, 0, -0.866, +0.866, \dots] \quad (6.2)$$

where  $t = k\Delta t$ ,  $k = 0, 1, \dots$  and  $\Delta t = 1/6000$  s.

Further observations on the resultant points on the unit circle enable to calculate in-phase and quadrature components even without a multiplication operation. Approximating the value 0.866 as 0.875, the following pseudo code explains how this implementation is done where ADC represents the scalar as the output of A/D converter and the '>>' operator stands for the bitwise right shift operator with the number of bits to shift next to it:

1. Allocate a dummy variable,  $k = 0$
2. If  $(k = 0) \Rightarrow$  in-phase = ADC,  
     quadrature = 0,  
     increment k for the next sample
3. If  $(k = 1) \Rightarrow$  in-phase =  $0 - (\text{ADC} \gg 1)$ ,  
     quadrature =  $\text{ADC} - (\text{ADC} \gg 3)$ ,  
     increment k for the next sample
4. If  $(k = 2) \Rightarrow$  in-phase =  $0 - (\text{ADC} \gg 1)$ ,  
     quadrature =  $(\text{ADC} \gg 3) - \text{ADC}$ ,  
     set k back to 0 to start all over from step 2.

The accuracy loss induced by the process above can be inspected by considering an average voltage term, for instance 513, at the output of the A/D converter. Note that at the second step of the calculation there is no accuracy loss. For the third step, Table 6.1 provides an exemplary comparison between the ideal case

and the implemented version. The table holds for the fourth step as well, except that quadrature components are the same in magnitude but signs should be converted into negative. It should be noted that 0.195% and 1% accuracy losses occur in average during the calculations of the in-phase and quadrature components, respectively. These percentages prove the realized approximation to be fairly tolerable in our case. An elaborate analysis of this approximation is possible but beyond the scope and interest of this study, especially since the losses are quite miniscule.

**Table 6.1** Average accuracy loss at step 3 of the pseudo code

	<b>Ideal calculation</b>	<b>Implementation</b>	<b>Difference from ideal (%)</b>
<b>in-phase</b>	-256.5	-256	0.195
<b>quadrature</b>	444.258	449	1.06

Lowpass filtering that should follow the mixers in order to obtain the baseband equivalent signal is performed as combined with the Barker code matching and studied in the next subsection. Here we refer to the samples after mixing as baseband signals with a misnaming.

### **6.1.2 The Matched Filtering Operation**

Having obtained the baseband equivalent of the received signal, the ensuing signal should be passed through a filter matched to the 13-length Barker sequence to detect the presence of a Barker preamble in the ultrasonic channel. In Chapter 4, the response at the output of the matched filter is analyzed for the case where transmitter sends a Barker waveform every 50 ms. As in the case of channel measurements, the chip duration is assumed to be 1ms in the PIC implementation. Therefore, 6 samples are collected on each chip with 6 kHz sampling rate. The following figure shows the construction of the matched filter for the Barker code

in which each chip is expanded to repeat itself six times. The reason for repetition will be justified subsequently.

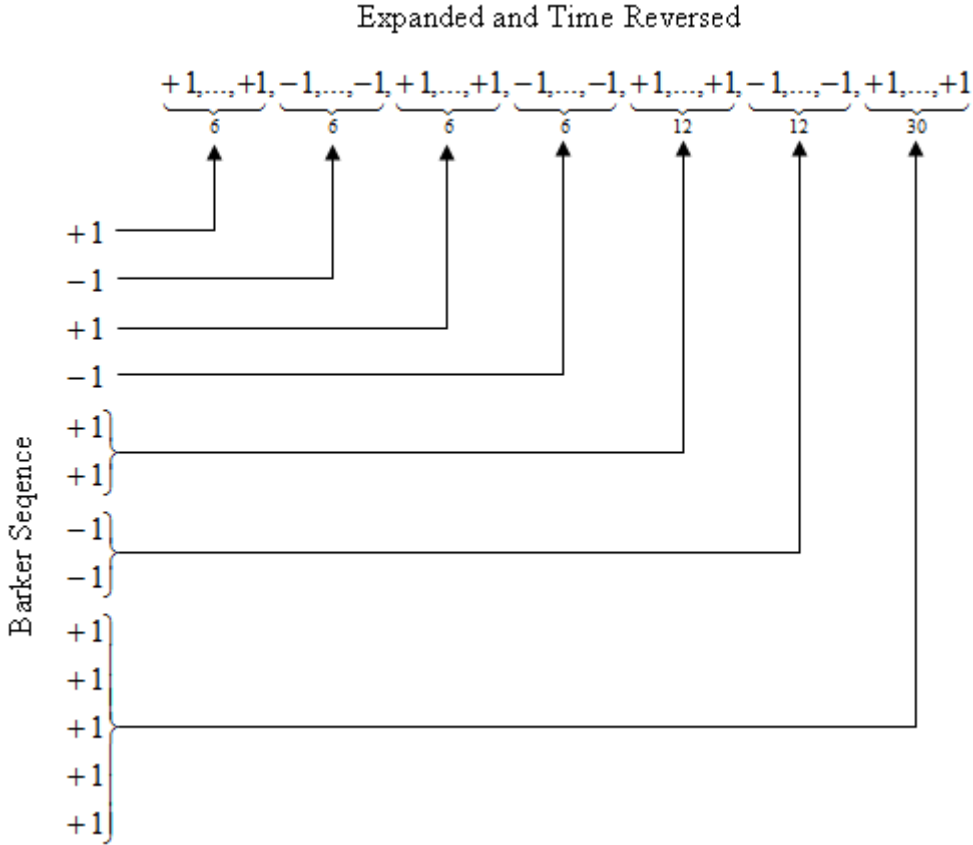


**Figure 6-3** Matched filter construction for the 13-length Barker sequence, chips are expanded by 6 times

The filter consists of 78 elements, an expanded and time reversed version of the original Barker code, hence consisting of +1s and -1s. Since the filter coefficients are all real, in-phase and quadrature components of the baseband signal may be handled separately to calculate the real and imaginary parts of the result. Furthermore, because the filter elements are all +1 and -1, the convolution operation requires only additions and subtractions. Actually this is an important detail simplifying the implementation by requiring less and simple operations and increasing the real-time performance in return. This is the reason why a rectangular receive pulse shape is taken with 6 times repetition.

The most recent 78 baseband signal components are stored in a window for convolution with the matched filter. In order not to miss the peak response and resolve the exact peak location at the output of the filter, the convolution should be realized with a window updated in a sample-based manner, i.e., whenever a new sample is acquired, its baseband equivalent is calculated and the window is updated to hold this recent component while dropping the oldest component. In terms of software terminology, this window can be thought as a first-in-first-out (FIFO) buffer that is updated on the arrival of each new sample. As a straightforward solution, one may choose to use the index 1 to hold for the most recent signal component, index 78 for the oldest one, and all the other indices in-between monotonically varying for others. The following figure illustrates the use of such an indexing for the window and the convolution arithmetic under this scheme.

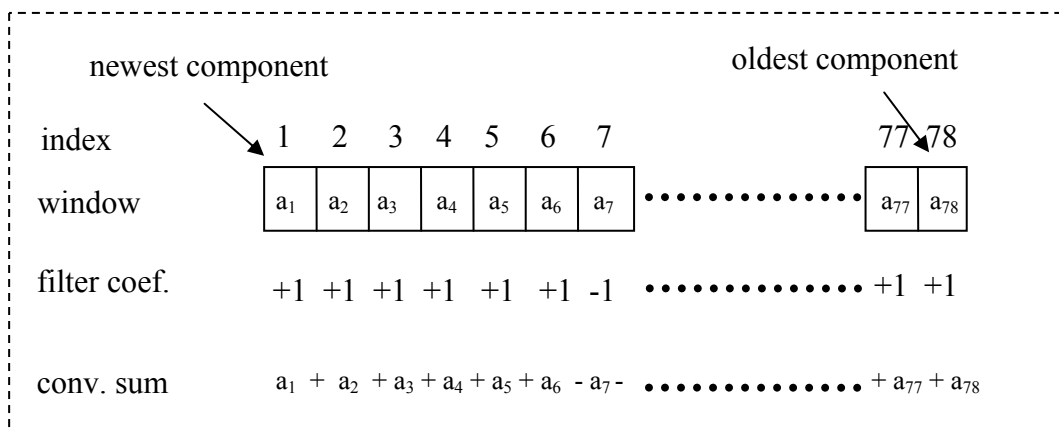


**Figure 6-4** The matched filtering operation on a length-78 linear window

The window should be shifted right to accommodate the new baseband sample calculated as a result of the A/D conversion and multiplication by sine/cosine. This sums to 77 move operations within a single window. Remembering that in-phase and quadrature components of the baseband signal are treated separately, the number of move operations becomes  $2 \times 77$ . The cost again doubles to

$4 \times 77$  when this process is repeated for the other branch since two receiving ultrasonic transducers are employed and data from both branches are used exactly in the same manner. To remove this overhead, an alternative solution is to use a circular buffer and an index to locate the position of the newest item in the buffer. Unnecessary moving operations diminish with the use of a circular buffer structure and relative indexing as depicted in Figure 6-5.

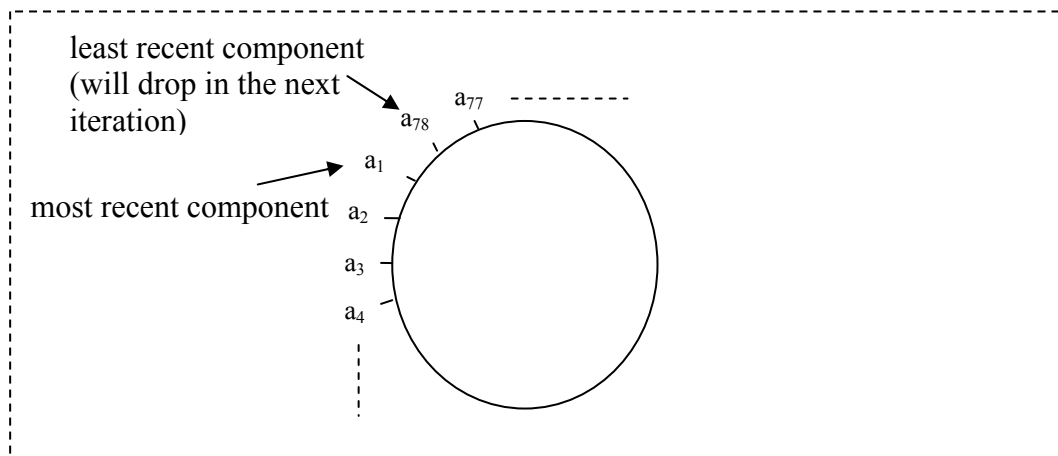


**Figure 6-5** 78-length circular window used for filtering operation

Yet, there is another inefficient aspect in the implementation: the convolution sum. Note that a total of 77 summation and subtraction operations are required at each step of the convolution and the number quadruples as real/imaginary parts are handled separately for both receivers. An observation on the convolution expression depicted in Figure 6-6 reveals another method that does not involve that many operations. The idea behind this new method arises when it is realized that the difference between two consecutive convolutions occurs due to the terms that change sign as well as the newly added term and the dropped term. So, by keeping track of the critical indices which are at the boundaries for changing sign due to the filter coefficients, it is no more necessary to perform the convolution from scratch. Rather, it can be calculated recursively in which the number of operations required decreases significantly. The discussion here can be best

understood from the figure below which shows the difference in the results of successive convolutions with an example. It should be stated here that the new method is combined with the circular window structure described although a linear window is preferred in this figure because it is more descriptive.

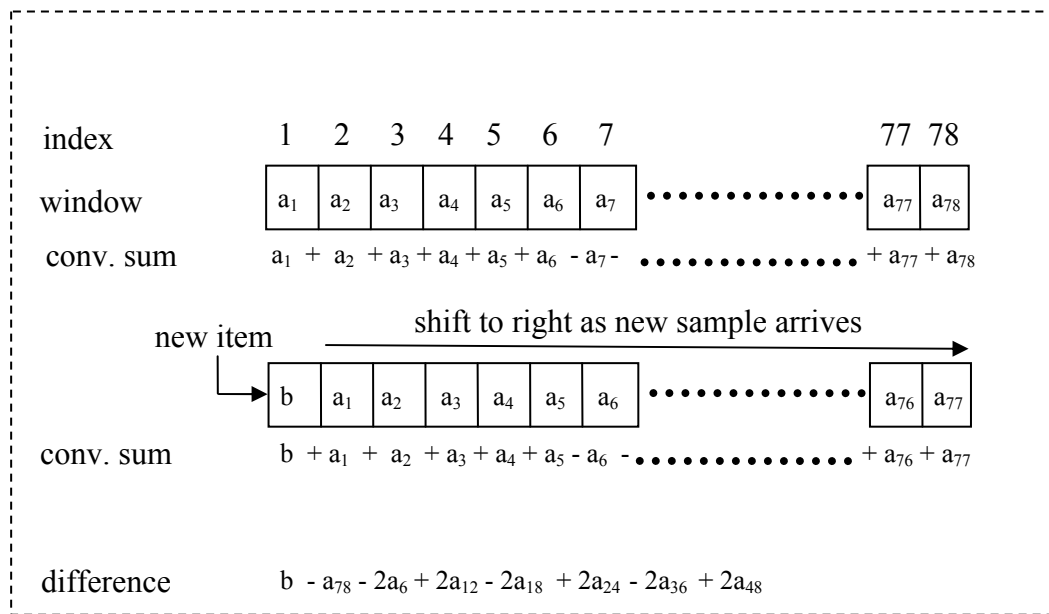


**Figure 6-6** Execution of matched filtering operation for consecutive iterations

The enhancement can be summarized as follows: Having known the convolution sum of the previous step, the current convolution can be calculated by adding the difference terms depicted in the figure above to the previous result. This only involves 7 additions (one for addition to the previous result) and 7 subtractions when multiplication by 2 is implemented as repeated addition/subtraction while calculation from scratch involves 77 operations. The difference in number of operations is significant from a processing time point of view. Referring to Table 5.2 of the previous chapter, a 16-bit addition or subtraction takes 0.4 μs thus making up 30.8 μs for a total of 77 operations. This is even more because the table gives the durations for unsigned variables whereas operations are performed here with signed variables. Remembering that this convolution is repeated 4 times following the acquisition of a new sample, it makes a total of around 123.2 μs.

There is not much time left to accommodate the remaining adaptive thresholding algorithm in this scheme, since everything must fit into  $166.67 \mu\text{s}$  at a sampling rate of 6 kHz. With the new method, the total processing time is around  $22.4 \mu\text{s}$  for all the 4 repetitions leaving a fair amount of time for the remaining portions of the software. It is interesting to notice that the number of required operations does not change even with a higher sampling rate with the proposed method. For instance with 12 kHz sampling rate, still 14 additions/subtractions are required. However, at this rate, the window length doubles to 156 and the overall processing should fit into  $83.33 \mu\text{s}$ , half of the previous one. Actually this trade-off justifies the use of 6 kHz sampling rate in this study. The following pseudo code summarizes the implementation of the matched filtering operation.

1. Initialize the necessary variables
  - o Allocate two 78-length windows (indexed as 0 to 77),  $W_I$  and  $W_Q$ , to hold the in-phase and quadrature components of the baseband signal separately, initialize to all zero.
  - o Allocate two variables to hold convolution sums,  $C_I = 0$ ,  $C_Q = 0$ .
  - o Allocate variables to hold critical indices in the windows and initialize as follows:
    - $i_1 = 0$ : holds the index to put the next item.
    - $i_2 = 72$ : holds the index of the 6<sup>th</sup> previous element.
    - $i_3 = 66$ : holds the index of the 12<sup>th</sup> previous element.
    - $i_4 = 60$ : holds the index of the 18<sup>th</sup> previous element.
    - $i_5 = 54$ : holds the index of the 24<sup>th</sup> previous element.
    - $i_6 = 42$ : holds the index of the 36<sup>th</sup> previous element.
    - $i_7 = 30$ : holds the index of the 48<sup>th</sup> previous element.
2. When the next sample arrives, calculate the in-phase/quadrature components  $s_I$  &  $s_Q$ .

3. Update  $C_I$  and  $C_Q$ :
  - o  $C_I = C_I + s_I - W_I(i_1) - 2W_I(i_2) + 2W_I(i_3) - 2W_I(i_4) + 2W_I(i_5) - 2W_I(i_6) + 2W_I(i_7)$
  - o  $C_Q = C_Q + s_Q - W_Q(i_1) - 2W_Q(i_2) + 2W_Q(i_3) - 2W_Q(i_4) + 2W_Q(i_5) - 2W_Q(i_6) + 2W_Q(i_7)$
4. Calculate  $|C|^2 = C_I^2 + C_Q^2$ .
5. Update both windows:
  - o  $W_I(i_1) = s_I$
  - o  $W_Q(i_1) = s_Q$
6. Increment all indices,  $i_1$  to  $i_7$  by 1.
7. Check the window boundaries for next iteration, If  $(i_j = 78) \Rightarrow i_j = 0$ .
8. Return to and wait at step 2.

Note that the magnitude square of the resultant signal is calculated at step 4. This metric is proportional to the output signal power and will be used in comparison with a threshold to detect the presence of the preamble in the channel. The next section details the use of this metric as an input to the decision mechanism. One may notice that the calculations reach to a steady state after collecting 78 samples due to the number of past elements required. This takes 13 ms from the initial power-up, and successful results can be obtained only thereafter.

### 6.1.3 Thresholding and Detection Mechanism

Having performed the matched filtering operation, magnitude-square of the resultant signal contributes to the decision of an ongoing transmission at the receiver side. This is performed by executing a threshold mechanism so that a signal level above a determined threshold level indicates the presence of a data transmission in the ultrasonic channel. Determination of this threshold involves continuous observations to be made in the channel so as to adapt the changes in the noise floor within the operation environment or in a completely new environment. Furthermore, since it is tightly coupled with probability of false alarm, the threshold is intended to be kept at a level that provides a constant false

alarm rate (CFAR) by using a method similar to that of CFAR approach in the radar terminology.

### 6.1.3.1 Determining Threshold Level

Threshold should be determined in conformance to the trade-off between false alarm and detection probabilities. While a low threshold may increase the tendency to detection, it increases probability of receiving false alarms as well. On the contrary, utilizing a high threshold would decrease the false alarm rate at the cost of reduced detection probability and operational ranges in return. From another point of view, detected packets should ensure a reasonable SNR level so that attained bit error rate makes practical sense. Therefore, threshold constitutes an important performance metric to be analyzed on a theoretical basis.

An analysis of the noise at the output of the matched filter is presented in Chapter 4 when Barker sequence is transmitted over the channel. In Figure 4-6, this noise is estimated to have a complex Gaussian distribution with zero-mean and variance  $N_0$  and Table 4.2 is constructed to list some  $N_0$  values extracted from a number of experiments. The derivation of  $P_{fa}$  below follows from detection theory where  $y_k$  denotes the output of the filter at the  $k^{\text{th}}$  time index in consistent with the earlier notation, and T is a constant threshold:

$$P_{fa} = P(\|y_k\|^2 > T \mid \text{no transmission is made}) . \quad (6.3)$$

In the expression for  $P_{fa}$  above, note that magnitude-square of the filter output is compared to a threshold. In the absence of a transmission, only complex Gaussian noise components contribute to the filter output:

$$y_k = n_k = n_{R,k} + jn_{I,k} , \quad (6.4)$$

where  $n_{R,k}$  and  $n_{I,k}$  are zero-mean Gaussian random variables with variance  $N_0/2$ . Assuming that the real and imaginary parts of the noise are independent, the term  $\|y_k\|^2$  is exponentially distributed with  $\lambda = 1/N_0$  where  $\lambda$  is the parameter of the exponential distribution that has the cumulative distribution function (cdf) given by

$$F(x, \lambda) = 1 - e^{-\lambda x}. \quad (6.5)$$

Combining equations (6-3) and (6.5), the relation between  $P_{fa}$  and the threshold  $T$  can be expressed as below.

$$P_{fa} = P(\|n_k\|^2 > T) = 1 - (1 - e^{-T/N_0}) = e^{-T/N_0} \quad (6.6)$$

$$T = -\ln(P_{fa}) \times N_0 \quad (6.7)$$

An alternative interpretation to equation (6.7) is that the threshold should be set to  $-\ln(P_{fa})$  times larger than the noise power  $N_0$  in order to ensure a false alarm rate of  $P_{fa}$ . To provide a practical understanding, assume one false alarm per minute is intended at a single channel. Since a comparison between the threshold and the filter output is held at each sampling cycle, this corresponds to a single false alarm over  $60 \times 6000$  comparisons in average. Putting the rate into the equation (6.7), this yields a threshold level equivalent to  $12.8N_0$ . Remember that selection diversity combining is proposed to be used to combine the received signals from two ultrasonic transducers. Therefore it is better to concentrate on the system false alarm rate rather than of a single channel. Assuming that two channels are exposed to independent noise components and that  $P_{fa}$  denotes the false alarm rate at a single channel, then the system false alarm rate  $P_{fa,sys}$  can be calculated as

$$P_{fa,sys} = P_{fa} + P_{fa} - P_{fa} \times P_{fa} \cong 2P_{fa}, \quad (6.8)$$

where squared term is neglected at the last step. If a single false alarm per minute in the system is reasonable, then separate channels should count only one false alarm over  $2 \times 60 \times 6000$  comparisons in average. This requires the threshold to be 13.5 times larger than the noise power  $N_0$ . The next section provides the details leading to the implementation that satisfies the condition between threshold level and noise floor.

### **6.1.3.2 Implementation of the CFAR Detection Mechanism**

It is important to note that continuously estimating the noise power with the arriving samples may be crucial in obtaining the desired constant false alarm rate especially in the occurrence of changes in the environmental conditions. In this scheme, the threshold can be adaptively updated to ensure that it is above the noise level by some amount. The ratio between the threshold and  $N_0$  has been showed to be an important performance metric determining the false alarm rate as discussed previously.

It is intended to provide a decision mechanism which is capable of operating at both high and low SNR circumstances. The main difference between the two cases that concerns the implementation is the resolvable side-lobes in the high SNR case which are above the noise floor. On the other hand, at low SNR unresolved side-lobes are likely to be treated as noise components which may outgrow the  $N_0$  estimate and the threshold level in return. Evidently, special attention is needed to handle both cases in order to propose a successful implementation. In the presence of noise only, the following block diagram summarizes how the threshold is calculated to assure a constant ratio,  $K$ , between the threshold and the noise power. Remember that the matched filtering operation applied in one of the previous steps yield a magnitude-square term that is proportional to the signal power, hence it is a convenient metric to take into account while tracking the ratio between the threshold and noise power.

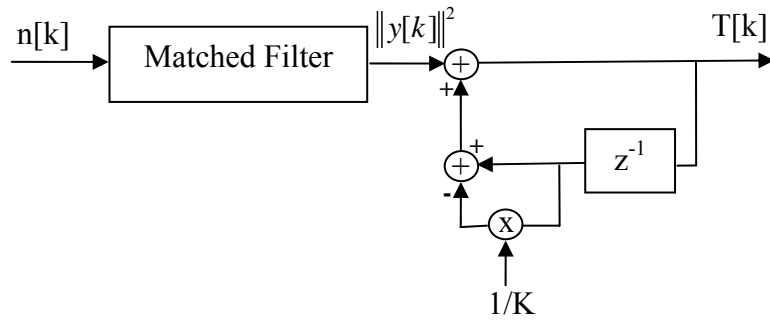


**Figure 6-7** Block diagram for calculating the threshold adaptively

An IIR-filter operation can be extracted from Figure 6-7 in which the current threshold can be expressed in terms of the current matched filter output and previous threshold level when the input to the matched filter is noise only.

$$T[k] = T[k-1] - \frac{1}{K}T[k-1] + \|y[k]\|^2 \quad (6.9)$$

Notice that, the current threshold level is corrected at each iteration so as to keep it above the noise with a predetermined amount. Since the term  $\|y[k]\|^2$  is a realization of noise with variance  $N_0$ ,  $T[k]$  can be expressed after a sufficient amount of iterations in terms of  $N_0$  estimate,  $\hat{N}_0$ , as

$$T[k] = K \times \hat{N}_0. \quad (6.10)$$

Therefore the constant term  $K$  enables adjusting the ratio between the threshold and  $N_0$  so that the equality given in equation (6.7) can be realized for a desired false alarm rate. Since the observed noise level may vary in the two ultrasonic channels, even though not much difference is expected, thresholds are estimated separately by executing the described mechanism above independently at each channel. It is important to keep updating the threshold level when there is no transmission in the channel and stop when a transmission is suspected. If the current output of the matched filter exceeds the threshold, this is treated as

detection of a possible transmission in the channel and a flag is raised. Furthermore, in order to guarantee to some extent that threshold is updated only with noise and not with the transmitted signal, the output of the matched filter is compared to the threshold that is estimated in the third previous time slot. This requires storing a 3-tap history for the threshold in the implementation.

To make a distinction between the side-lobes and the main-lobe in the high SNR case, the peak location should be searched at the vicinity of the first flag raised, with the time interval for the search depending on the preamble autocorrelation characteristics, the sampling rate, and the channel's delay spread ultimately although delay spread is not taken into account in the PIC implementation. This corresponds to a peak search within 78 samples starting from the first passing over the threshold with the 6 kHz sampling rate (refer to Figure 4-1 which shows the autocorrelation function of the 13-length Barker sequence). The software extends this interval to 90 samples to provide a safer operating region rather than working on the limits. Actually this results in a delayed response on the decision of exact peak location. The search is finalized after 90 samples following the resolved peak response. This is important in shaping the packet structure to be used in data transmission. The very first data bit should be sent after a 15 ms guard interval following the preamble to ensure that demodulation data starts at the correct time instance at the receiver side. Packet structure to be used in the system is shown in Figure 6-8.

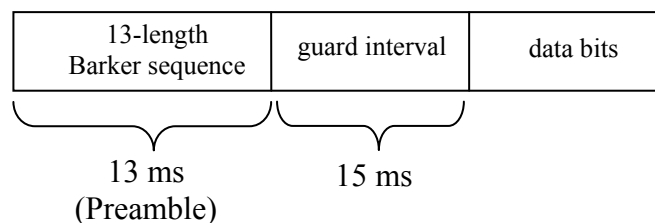


**Figure 6-8** Overall data packet structure

Figure 6-9 describes the general procedure for packet detection at a single channel. In fact, the overall process consists of two concurrent branches since

two channels undergo each step independently. The thresholds are initially set to a relatively high value in order not to observe false alarms at the beginning, perhaps at the cost of losing ongoing packets at the startup. With the assumption that the receiver always starts operation before the transmitter, this overhead diminishes. Since the selection diversity combining technique is to be applied to combine the two receivers' data, peak responses of the matched filters at two branches are compared to proceed with one of the channels. Assuming the difference in the noise powers of the two channels is negligible in this scheme, this comparison yields the larger SNR branch which can be used for demodulation of the DPSK data.

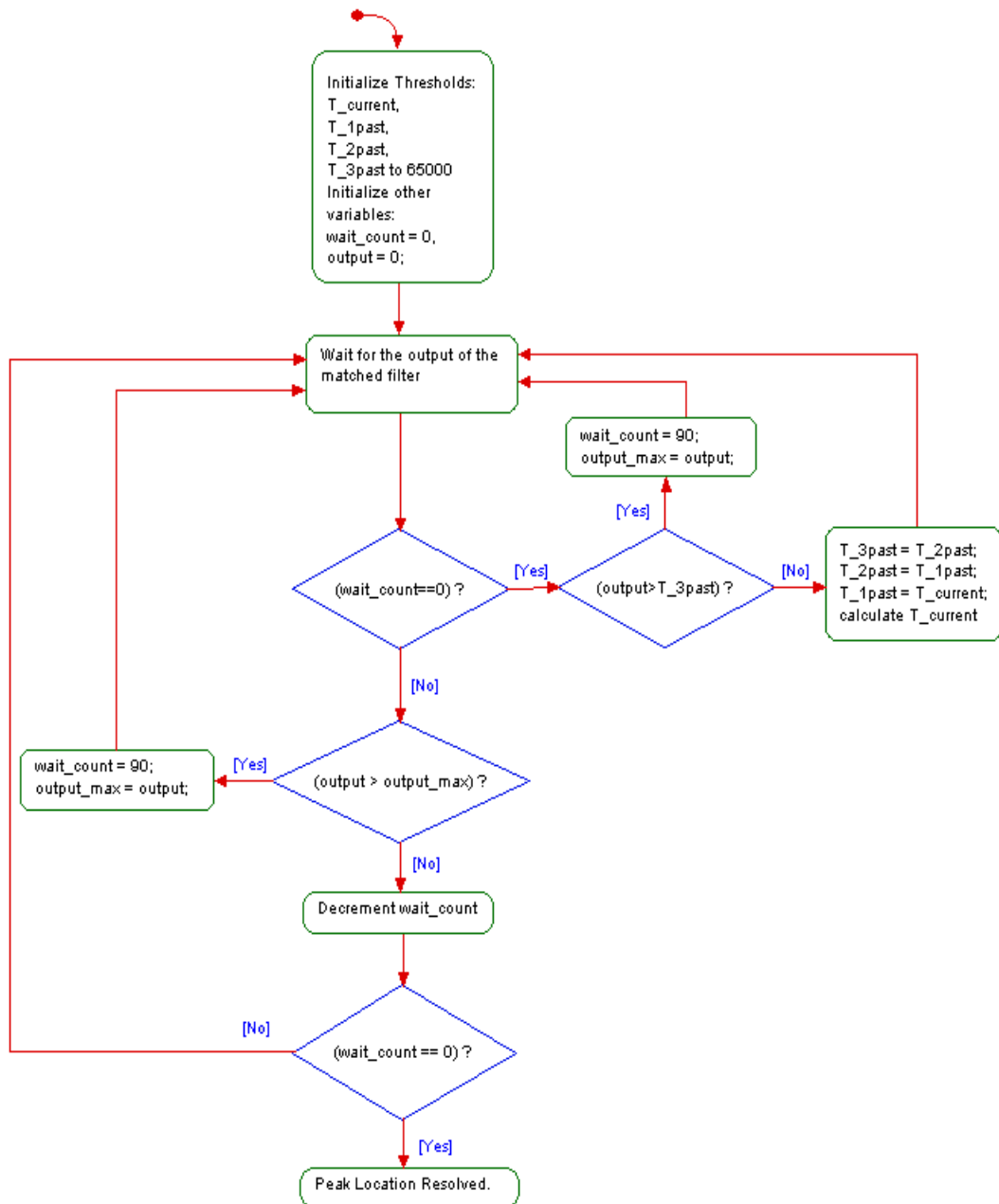


**Figure 6-9** Flow chart for packet detection

Figure 6-10 depicts several threshold levels of varying ratios between the threshold and the noise power. In Chapter 4, the data processed here is used for the free-space ultrasonic channel experiments in which the transmitter-receiver separation corresponds to 10 m. Note in the figure that the threshold level stays constant with the first flag raised until the peak is resolved. In the actual data transmission scenario the threshold is not updated until demodulation of data ends. Since the aim here is to demonstrate how the threshold is updated with different  $K$ s, a new peak search immediately begins as a peak location is resolved. The vertical axis depicts a power related metric at the output of the filter where each actual voltage level is converted back to 1024 A/D levels as it is the case in a 10 bit conversion. This makes a better sense while testing the real computations which will run on the microcontroller.

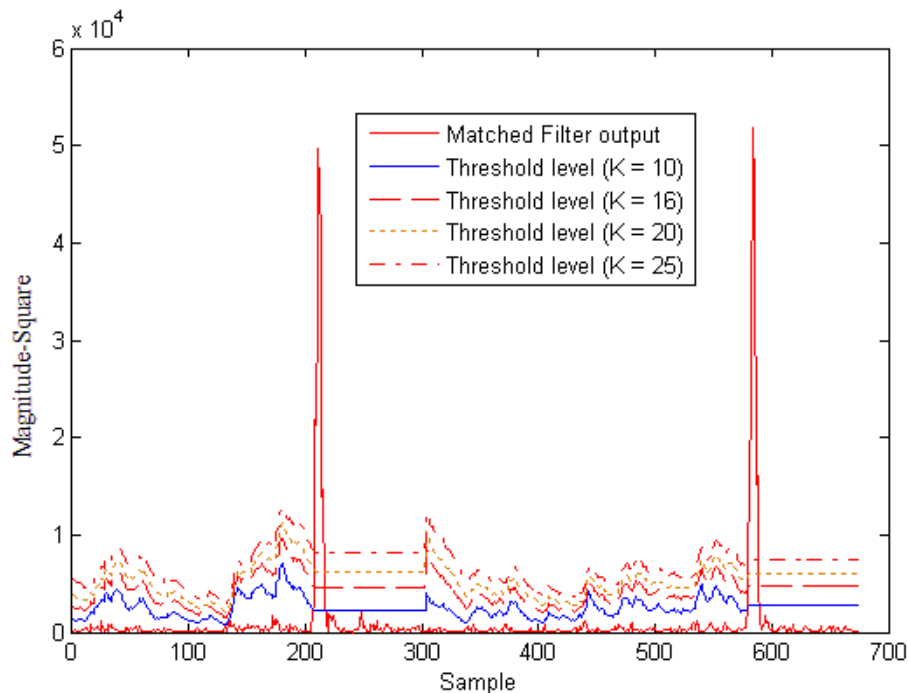


**Figure 6-10** Threshold levels for a number of ratio constants  $K$

## 6.2 The Implementation of D-BPSK Demodulation

Upon the detection of a packet, the subsequent received data can be used to demodulate the D-BPSK bits. As it is the case in the packet detection, the received signal is first converted to baseband by mixing and rectangular pulse shaped matched filtering. The matched filter is a window consisting of all 1s of length 6 due to 6 kHz sampling rate and 1 ms bit duration. The duration of demodulation depends on the number of data bits in a packet.

It is possible to separately treat the in-phase and quadrature components of the baseband signal once again due to the real filter coefficients. The implementation of baseband conversion is exactly the same as in packet detection so it will not be dealt here once more. As opposed to the process held in detection, there is no need to store each individual baseband signal in memory. The difference is due to the fact that the exact timing of the packet is not known and to be determined in the case of detection. However, this is not necessary in the implementation of demodulation since the symbol synchronization is already achieved in detection. All the subsequent operations are performed at the symbol rate of 1 kHz. The process is visualized in Figure 6-11.

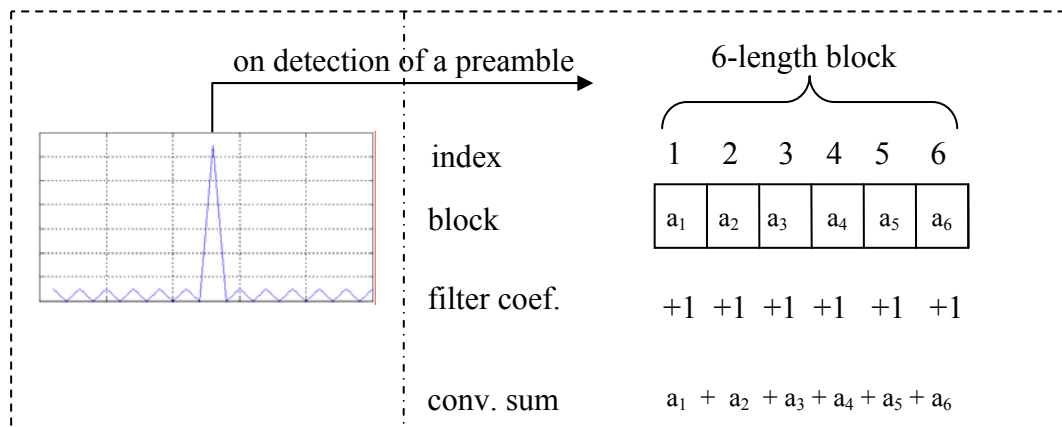


**Figure 6-11** Convolution with rectangular filter prior to differential demodulation

Since convolution with the rectangular filter corresponds to summing the signal components within each 6-sample block, there is no need to wait for the arrival of all the 6 samples within the same block which will require storing some history. Rather, the operation may be efficiently implemented as repetitive summation as the samples arrive and the operation is finalized at the sixth iteration. The signals obtained for the real and imaginary components can be put together in the differential demodulation scheme which is previously given to be

$$\operatorname{Re}(y_k y_{k-1}^*) \begin{cases} < 0, \text{bit '1' is sent} \\ > 0, \text{bit '0' is sent} \end{cases} \quad (6.11)$$

where  $y_k$  is the complex output of the filtering operation performed for the  $k^{\text{th}}$  symbol and ‘\*’ is the complex conjugate operation. To conclude on the received bit, one should track not only the current output of the filter but also the previous one. Denoting the real and imaginary parts of  $y_k$  as  $r_k$  and  $i_k$ , respectively the expression can be replaced by the following one taking into account the results of individual filtering operations:

$$(r_k r_{k-1} + i_k i_{k-1}) \begin{cases} < 0, \text{bit '1' is sent} \\ > 0, \text{bit '0' is sent} \end{cases} \quad (6.12)$$

The following pseudo code gives an overview of the implementation of the D-BPSK demodulator. Processing symbol intervals continues until all the data is extracted from the detected packet. The following operations take place in one of the channels at a time since selection diversity combining method is utilized here.

1. Initialization

- a. Allocate a dummy variable,  $n = 0$
- b. Allocate 2 variables, `output_real` and `output_imag`, to store the current results of the filtering operations, initialize to 0.

- c. Allocate 2 variables, `output_real_pre` and `output_imag_pre`, to store the previous results of filtering operations, initialize to 0.
2. When the next sample arrives calculate baseband equivalent with  $s_I$  and  $s_Q$  in-phase/quadrature components, respectively.
3. Update `output_real` and `output_imag`:
  - a. `output_real = output_real + s_I.`
  - b. `output_imag = output_imag + s_Q.`
4. Increment  $n$ .
5. If ( $n == 6$ ) go to the step 6 otherwise go to 2.
6. Calculate:
 

```
D=output_real*output_real_pre + output_imag*output_imag_pre.
```

 If ( $D < 0$ ) decide '1' else '0'
7. Update history:
 

```
output_real_pre = output_real.
```

```
output_imag_pre = output_imag.
```
8. Reset the counter variable  $n$ , `output_real` and `output_imag` to 0.
9. If there are more bits to receive go to step 2, otherwise exit from the procedure.

### 6.3 Testing and Measuring System Performance

Completing the design and the implementation of the algorithms on the PIC microcontroller, a number of tests are performed on the target platform to ensure correct receiving operations and obtain some metrics to evaluate the overall system performance. In fact, during the development phase enormous effort for testing is spent for many intermediate stages among which the followings have an end point perspective.

#### 6.3.1 Observing Computational Results on PIC 18F452

Every critical computational step in the software is analyzed with a test data set that can readily be processed in MATLAB for comparison. By putting no time

restriction, this kind of test provides isolation from hardware related problems. A data set is loaded to the program memory and referenced at run time as if it is received from the A/D converter module and corresponding results are sent to a PC over the serial line. Since packet detection involves much more complex operations than the demodulation phase, it is the primary means for this type of test.

The outputs of many intermediate steps are inspected in the development. Figure 6-12 compares outputs of the filter matched to the Barker sequence in PIC and in MATLAB as it may illustrate the cumulative effect of many inner computations. Even though the output of the matched filter in the microcontroller is subject to accuracy errors introduced by intermediate levels, the difference from MATLAB is hardly resolved. The peaks occur at the 221<sup>st</sup> time index for both computations and the MATLAB value is greater by a small amount (0.0273 dB). When the Barker sequence is detected, the threshold level calculated in MATLAB is greater than that of PIC by no more than 0.24 dB. These losses are produced by the use of approximations in baseband conversions and bitwise shift operations in place of division, and they are insignificant in the scope of this study.

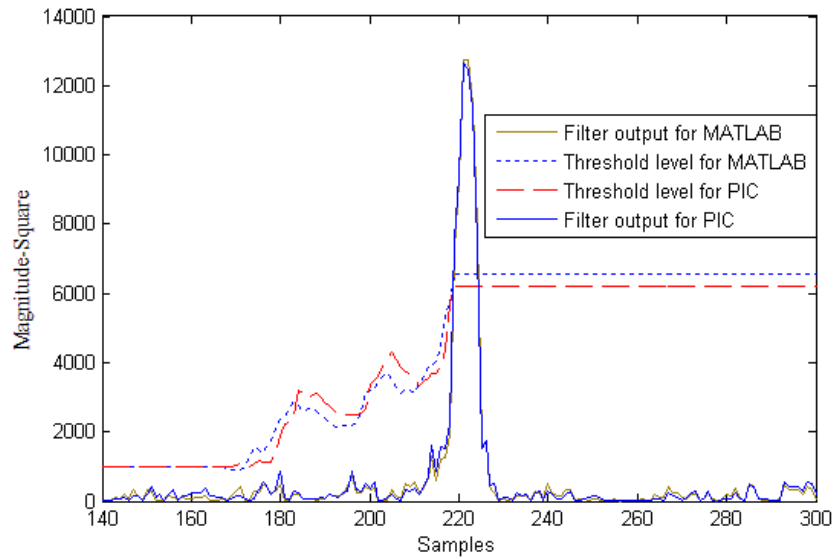


**Figure 6-12** Comparison between the matched filter outputs of PIC and MATLAB along with the corresponding threshold levels

### 6.3.2 Timing Measures

Having validated the computational steps, it is equivalently important to be sure that those computations fit into a sampling period of  $166.67 \mu\text{s}$  for real time operations. As described previously, a regular sampling rate is obtained by use of a special compare module embedded in the microcontroller and a timer module that is incremented in the resolution of 100 ns under ideal conditions. It is experimentally found that 6 kHz rate is equivalent to 1626 increments of the timer and a sample is acquired from the A/D converter at the end of each 1626<sup>th</sup> increment. Therefore, it is better to measure the execution time relative to timer increments which can be accomplished by reading the value from the timer's register.

It is convenient to justify that the software meets its timing constraints in terms of the worst and best case scenarios as well as the average execution time. For that reason, a number of iterations are performed on the software. Since packet detection and demodulation occur at different time slots, they are handled

separately in the analysis. The detection portion is further divided into three phases for practical reasons: the first and second channel's data are processed in the first and second phases, respectively. In the third phase, preparation for the next iteration, such as updating indices, occurs. Table 6.2 summarizes the timing measurements that are corrected by taking into account the overhead of 20 increments introduced by the function call to read the timer register.

As seen in Table 6.2, detection operations in channel 1 last a bit longer than for channel 2. This is because some operations of channel 2 that do not require acquisition of a new sample are performed in the time slot of channel 1 in order to leave sufficient amount of time for the third phase. The worst case total timing of 1580 increments, being less than 1626 increments all the calculations are completed before the acquisition of a new sample.

**Table 6.2** Execution times (in units of timer increments) for different phases

	Detection 1	Detection 2	Detection 3	Demodulation
Best case	708	650	4	321
Worst case	792	756	32	348
Average	742	717	30	337

### 6.3.3 Memory Measures

Memory is an important limitation while working with a source limited processing unit such as a PIC. For instance, in our case PIC 18F452 provides only 1536 bytes of RAM to the software. This restriction requires measuring the number of memory elements used in the implemented algorithms. The following table presents the amount of memory elements involved in the communication schemes with different number of receiving ultrasonic transducers. Note that the

implemented system with 2 transducers in this study uses almost the half of the memory resources in worst case scenario and that a maximum of 4 transducers can be employed in the proposed scheme due to memory limitations. However, with more than 2 transducers sampling interval should be revised in order to provide sufficient amount of time to the algorithms to be executed on separate channels. Referring to Table 6.3, integrating a new transducer to the system has a memory cost of 335 bytes. 44 bytes are used for housekeeping activities, such as indexing for common circular buffer structures, that are shared among different channels and independent of the number of transducers involved.

**Table 6.3** Amount of memory elements used for different number of transducers

# of transducers	1	2	3	4
Memory (bytes)	379	714	1049	1384
Memory (%)	25	46	68	90

### 6.3.4 False Alarm Rate Observations

As derived mathematically, the ratio between the threshold used for packet detection and the noise level is the only parameter determining the false alarm rate in an AWGN channel. To provide a basis for comparison between the theory and actual results and find a ratio that will yield a reasonable false alarm rate, iterations are performed on the receiver while there is no transmission at the channel. At the receiver side only the detection part of the algorithm runs, i.e., a no demodulation action is taken after a false alarm and a new search starts immediately. The following table summarizes the test results where  $K$  in the first column corresponds to the constant ratio used in the algorithm between the threshold and the continuously estimated noise floor. The number of iterations is

equivalent to the number of samples collected at both channels so that the data in the first row requires around 3.5 minutes of continuous observation.

**Table 6.4** False alarm rate observations

<b><math>K</math></b>	<b># of iterations</b>	<b># of false alarms</b>	<b><math>P_{fa}</math> measured</b>	<b><math>P_{fa}</math> calculated</b>
8	2,621,440	4110	1.57e-3	6.71e-4
10.67	8,257,536	1496	1.81e-4	4.65e-5
12.8	11,665,408	376	3.22e-5	5.52e-6
16	26,476,544	52	1.96e-6	2.25e-7

The ratio constant  $K$  can be either expressed as a power of 2 or a combination of two values both are expressed as some power of 2. This allows replacing division operations by bitwise shift operations and additions. For instance, the value 10.67 may be obtained in two steps as in

$$T[k] = T[k-1] - \frac{1}{16}T[k-1] - \frac{1}{32}T[k-1] + \|y[k]\|^2 \quad (6.13)$$

$$= T[k-1] - \frac{1}{10.67}T[k-1] + \|y[k]\|^2, \quad (6.14)$$

where 16 and 32 are substituted into equation (6.9) previously given as the mechanism for updating threshold. While preparing the column for false alarms rate, alarms from separate channels are added as they will initiate necessary actions for demodulation in a real reception scenario. However if both channels raise flag at the same time instant, it is counted as a single false alarm. This is consistent with the proposed combining method where demodulation continues with the branch of higher SNR. The calculation of false alarm probability in the last column follows from equations (6.7) and (6.8) where the neglected term in equation (6.8) corresponds to the case in which both channels gives false alarm at the same time instant. Figure 6-13 puts the false alarm rates depicted in Table 6.3 into a graphical interpretation where approximately 0.5 dB difference between the two curves is realized.

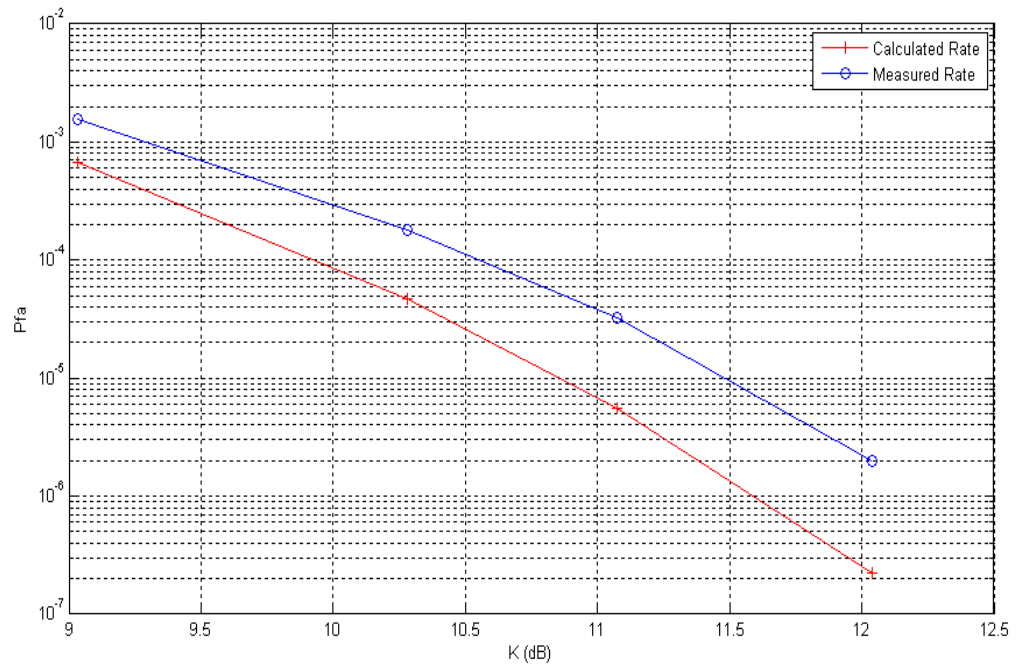


**Figure 6-13** False alarm rate for a number of ratio constants K

The accuracy losses introduced by the computational steps within the implemented algorithm are responsible for some portion of the difference. Those losses prevent setting the ratio between the threshold and the estimated noise power to the exactly desired value. Another possible reason for the difference is the delayed IIR-filter response for estimating the noise power. The changes in the noise power cannot be adapted immediately. Moreover, the calculated rate curve corresponds to an ideal case at which noise distribution is assumed to be complex-Gaussian. This may not be the exact case in a real world scenario.

### 6.3.5 BER Measurements

To obtain the BER curve, packets that contain 100 data bits are transmitted through the ultrasonic channel. 22 ms delay is put between each consecutive packet. Therefore, it takes 150 ms to send 100 bits of data taking into account the preamble and the guard interval that last for 13 ms and 15 ms, respectively. The

data to be transmitted is a random sequence of 0s and 1s also known by the receiver. The same sequence is repeated at each transmission. The transmitter is given a slow circular motion through a path of radius around  $\lambda$  so that phase variations can be observed at the receiver which enables to measure the benefits of diversity in return.

At the receiver side, 3 cm of separation is set between the two transducers. Although the experiment is performed in an indoor environment at close ranges, no ISI effect is measured since the implemented system does not contain an amplifier. The threshold level is put 21.33 times larger than the noise power. Theoretically, this corresponds to a false alarm rate of  $1.1e-9$  which is low enough to assume that no false alarm is raised during the experiment and thus all the detected packets contribute to the BER calculation. Every received packet is compared to the actual transmitted packet and the number of erroneous bits is recorded. The receiver continues operation until 1000 data packets are received which corresponds to 100,000 bits. Then after, the total number of bit error is transmitted to the PC through the serial line. Figure 6-13 depicts the corresponding BER curves for varying transmitter-receiver distances. Note in the figure that at 30 cm distance receiver 1 and 2 attain bit error rates of around  $1e-3$  and  $3e-3$ , respectively. The same bit error rates are achieved in the SC curve at distances approximately 43 cm and 53 cm. Hence with the diversity combining, the multi-transducer system performs 1.5-1.77 times better than the single transducer system in terms of BER performance. The consistent difference observed in the curves for single receivers is mainly due to the differences in the responses of separate ultrasonic transducers. Imperfections in manufacturing may result in deviation from the 40 kHz center frequency as well as in the variation of sensibility to sound pressure levels specified for the transducers.

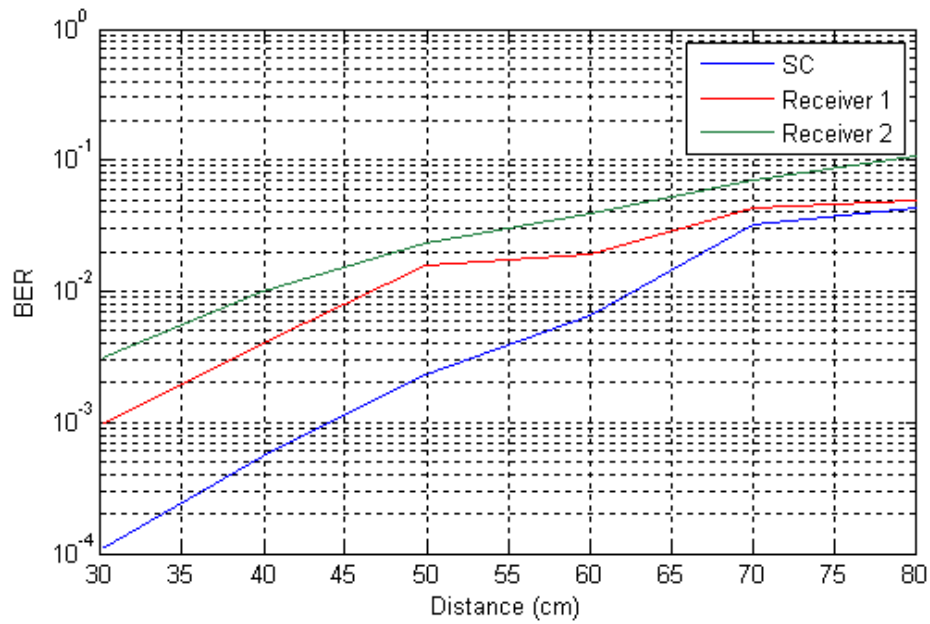


**Figure 6-14** BER measurements for varying receiver-transmitter separations

## 6.4 Conclusion

In this chapter, implementation details of an ultrasonic receiver node with two transducers are presented. The algorithms for packet detection, SC diversity, and differential demodulation are proposed and optimized to successfully run on a simple and low cost PIC processor at 6 kHz sampling rate. The implemented packet detection mechanism involves continuous observation of the noise floor and assures a constant false alarm rate similar to the CFAR method used in radar applications.

At the end of the chapter, some metrics are provided in order to evaluate the overall system performance. Computational steps are verified by comparing to the MATLAB results for the same set of inputs and real-time behavior is measured. Analysis on memory usage reveals that the final system uses almost the half of the available memory and that a maximum of four transducers may be hosted within the proposed scheme. Mathematically derived false alarm rates are compared to the measured rates for varying threshold levels and no considerable

difference is reported. Finally, diversity gain is inspected in terms of BER performance and significant superiority of the combiner output over single branches is presented. Although the BER estimates are provided for short ranges, one can draw similar results at practical communication ranges with the integration of an amplifier to the proposed system. Since this integration involves many electronic circuit design issues, it is beyond the scope and interest of this study and left as a future study.

## **CHAPTER 7**

### **CONCLUSION**

#### **7.1 Summary**

In this thesis, we investigated the terrestrial ultrasonic channel to figure out whether reliable data communication can be established through this channel. The primary intention was to provide another means for communication where RF communication may fail due to the radio signal propagation characteristics. The utilization of ultrasound for data communication, even as a backup channel for the highly preferred RF channel, would offer diversification of communication media crucial especially in some areas such as military communications. Although there are many studies for underwater acoustic communication with several applications, the research work in the area of terrestrial ultrasonic communications is very limited and lacks of details so as to conclude on some specific communication scenarios that can be constructed on this channel. Therefore, the key characteristics of the channel were observed with the ultrasonic transducers in hand in order to build a device capable of receiving data through the ultrasonic channel with the use of several well-known digital communication techniques.

The study first detailed the construction of an experiment setup that would enable ultrasonic channel observations up to 20-30 meters. Having observed important ultrasonic channel characteristics, another primary intention in the study was to show that ultrasonic communication can be enhanced with the use of multiple transducers. Hence, experiments were conveyed with small separations between

multiple receiving ultrasonic transducers and promising results are obtained for receiver diversity gain under a single-input-multiple-output (SIMO) scheme.

As a final study in this thesis, on the basis of encouraging experiment results, it is intended to show that it is realizable to implement a receiver node with two ultrasonic transducers that attains a receiver diversity gain. A very important benefit in using the ultrasonic channel is the ease of design and manufacturing at lower frequencies. Furthermore, a low cost microcontroller is adequate for digital signal processing required for packet detection and demodulation. A 40 MHz PIC 18F452 is used to execute a selection combining (SC) receiver diversity scheme, a constant false alarm rate (CFAR) packet detection algorithm, and differential binary phase shift keying (D-BPSK) demodulation. The implemented system is consistent with the general concepts of a WSN node in terms of cost, size, and power limitations. Further, it is not challenging to implement an ultrasonic transmitter with the same type of microcontroller as it can readily drive a 40 kHz transducer. Transmitter implementation is not in the scope of this thesis and left as a future study.

## **7.2 Conclusions on Experiments**

Experiments were initially performed in an outdoor environment without scatterers in the surroundings that is convenient to model as an Additive White Gaussian Noise (AWGN) channel. This provided channel response observation for varying transmitter-receiver separations and the latency introduced by the electromechanical components of piezoelectric ultrasonic transducers in the absence of inter-symbol-interference (ISI) related issues. No destructive effect of the transducer response is observed with a symbol duration of 1 ms. Since receiving transducers convert mechanical stress into electrical waveform, the transient response of the transducers are expected to get longer for shorter symbol durations hence obscuring the channel response. A pilot sequence in the form of a 13-length Barker code is transmitted through the channel to analyze SNR and the

channel capacity. The results reveal that the channel capacity of around 14 kbps for 1 m transmitter-receiver separation decreases to 1.22 kbps for 20 m separation at 1 kHz communication bandwidth.

As the second objective for the experiments, the average delay spread of the ultrasonic channel is inspected in both indoor and outdoor environments suitable for multipath propagation. The analysis is performed under both LOS and non-LOS transmission scenarios and the average delay spreads in the multipath channels are estimated to be in the order of a few milliseconds. Depending on the communication bandwidth, those results may be used to determine the multipath fading model to be employed in the ultrasonic channel.

The receiver correlation under LOS and non-LOS conditions in an indoor environment is observed to figure out whether ultrasonic communication can be enhanced with the use of multiple transducers. The studies presented in this thesis revealed that a small separation between the receivers yields almost uncorrelated reception even under strong LOS conditions. Experimental results agree for the non-LOS condition with further reduction in the separation of receivers. This constituted the basis for an increased expectation in attainable receiver diversity gain by utilizing multiple receiving ultrasonic transducers.

The experiments are finally extended to observe the BER when D-BPSK modulation scheme with a bit rate of 1 kbps is used. The analyses were led in a manner so as to keep direct correspondence to a possible implementation with a low cost processor unit such as a PIC microcontroller. For this reason, receiver diversity gain in a SIMO scheme using two receiving transducers is explored at a communication rate fairly below the ultrasonic channel capacity predictions obtained from previous experiments. The observations of two receivers are combined with a well known linear diversity technique, Maximal Ratio Combining (MC), and a significant diversity gain is enjoyed. Hence, in some applications such as wireless sensor networks where the communication range is

limited, the ultrasonic channel can prove itself as an alternative to the RF channel due to important benefits of MIMO capability in small areas.

### **7.3 Conclusion on Implementations**

Another important purpose in this thesis was to demonstrate that the promising experimental results on receiver diversity can be realized with the advantage of simple design and manufacturing provided by the low operating frequency of the transducers in hand. For this reason, the details of the study relevant to the implementation of such a prototype were presented both in terms of hardware and software aspects. As a computational unit, an 18F452 series PIC microcontroller is employed in the proposed receiver scheme. Although the primary application of those type of processors are low-rate control applications, a real time software, which is capable of performing many complex digital signal processing operations at 6 kHz sampling rate, is successfully integrated on the hardware. These operations include a packet detection algorithm with threshold adaptation, the selection diversity combining scheme, and demodulation of the received D-BPSK signal with 1 ms bit duration.

Although the final system contains only two receivers, it is adequate for many purposes such as to observe the SIMO channel characteristics and achieve receiver diversity. The algorithms and software are designed in an extendable manner to readily enable further integration of more transducers. Using more transducers would require reducing the communication rate to leave sufficient amount of time to the algorithms that will be executed on more channels. Besides, one may need to revise the diversity combining method implemented herein since the superiority of MRC over SC becomes more significant as the number of receivers involved increases. In fact, memory limitations of the PIC microcontroller used allows a maximum of 4 ultrasonic transducers within the implemented scheme.

## 7.4 Future Directions

In this thesis, no optimization is intended over the electrical components. A number of enhancements may be applied over the experimental setup to improve the quality of the ultrasonic channel observations. For instance, the amplifier scheme used throughout this thesis may be accompanied with a simple Butterworth type band-pass filter. Although the ultrasonic transducers have strong band-pass characteristics on their own, filtering out the thermal noise introduced by electrical components will be beneficial in obtaining better experimental results and in increasing the maximum observation ranges. Furthermore, replacing transducers with the ones fabricated for only receive or transmit purposes may provide working on the channel with increased sensitivity which may enhance the conclusions presented in this study in return.

The implementation presented here is primarily concerned with an AWGN ultrasonic channel. To achieve immunity against noise and inter-symbol interference (ISI), the adaptation of spread spectrum techniques to ultrasonic channels may be considered. The primary focus should be in using the narrow ultrasonic communication bandwidth in an efficient manner. Moreover, rectangular pulse shapes that are used throughout the analysis and implementation herein may be replaced with an effective pulse shaping scheme to reduce the power of spectral side-lobes and increase spectral efficiency.

A low noise amplifier may be integrated to the proposed ultrasonic receiver node so that the system performance can be evaluated at practical communication ranges. A more powerful processing unit may be utilized to implement the corresponding communication scenario. Besides, additional receiving ultrasonic transducers may be integrated on that processor so as to inspect higher receiver diversity gains. The MRC technique performs significantly better than the SC when more antennas are put in use. The implementation should take this into account.

Since a receiver clock mismatch may prevent the proper operation of demodulation beyond some packet sizes, some analysis may be performed to find out an optimum data packet length to transmit through the ultrasonic channels after each pilot sequence. And finally, some channel coding schemes may be used to reduce BER presented in the study.

## REFERENCES

- [1] I. F. Akyildiz, D. Pompili, and T. Melodia, "Underwater acoustic sensor networks: Research challenges", *Ad Hoc Networks (Elsevier)*, vol. 3, no. 3, pp. 257-279, March 2005.
- [2] G. J. Pottie, "Wireless sensor networks", in *IEEE Information Theory Workshop Proceedings*, June 1998.
- [3] F. A. Everest, *Master Handbook of Acoustics*, 4<sup>th</sup> Ed. NY: McGraw-Hill, 2001.
- [4] M. D. L. D. Castro, and F. P. Capote, *Analytical Applications of Ultrasound*, 1<sup>st</sup> Ed. UK: Elsevier Science, 2007.
- [5] S. Holm, "Airborne ultrasound data communications: The core of an indoor positioning system", in *IEEE Int. Ultrasonics Symp.*, September 2005.
- [6] T. L. Murphy, "Ultrasonic digital communication system for a steel wall multipath channel: methods and results", M. S. Thesis, Rensselaer Polytechnic Institute, Dec. 2005.
- [7] A. H. Quazi, and W. L. Konrad, "Underwater acoustic communication", *IEEE Communications Magazine* 20 (2) (1982) 24-30.
- [8] M. Stojanovic, "Recent Advances in High-Speed Underwater Acoustic Communications", *Oceanic Engineering, IEEE Journal of*, vol. 21, no. 2, pp. 125-136, 1996.

- [9] Underwater Sensor Networks at BWN Laboratory, Georgia Institute of Technology, Accessed 2 Jan. 2009, online: <<http://www.ece.gatech.edu/research/labs/bwn/UWASN/>>.
- [10] J. Zhang, Z. Huang, X Liu, “Acoustic communications in wireless sensor networks”, unpublished, University of Virginia.
- [11] S. Holm, O.B. Hovind, S. Rostad, and R. Holm, “Indoors Data Communications Using Airborne Ultrasound”, in IEEE Int. Conf. on Acoust. Speech Sign. Proc. March 2005.
- [12] H. D. Haynes, M. A. Akerman, and V. M. Baylor, “Y-NSP-252 Final Report: Ultrasonic Communication Project; Phase 1, FY 1999”, National Security Program Office of the Oak Ridge Y-12 Plant Managed by Lockheed Martin Energy Systems Inc. for the U.S. Department of Energy, Accessed 2 Jan. 2009, online: <<http://www1.y12.doe.gov/search/library/documents/pdf/ynsp-252.pdf>>.
- [13] USB-6211 Datasheet, Accessed 2 Jan. 2009, online: <<http://sine.ni.com/nips/cds/view/p/lang/en/nid/203190>>.
- [14] M. T. Smith, Audio Engineer's Reference Book, 2<sup>nd</sup> Ed. MA: Focal Press, 2001.
- [15] A. F. Grandt, Fundamentals of Structural Integrity, 1<sup>st</sup> Ed. NJ: John Wiley & Sons Inc. 2004.
- [16] Piezoelectric Materials Overview, Accessed 2 Jan. 2009, online: <<http://www.azom.com/Details.asp?ArticleID=81>>.

- [17] Ultrasonic Transducers' Specifications, Accessed 2 Jan. 2009, online: <[http://www.quartz1.com/downloads/UltrasonicSensors/T\\_R40-6OA00.pdf](http://www.quartz1.com/downloads/UltrasonicSensors/T_R40-6OA00.pdf)>.
- [18] Ultrasonic Transducers' Specifications, Accessed 2 Jan. 2009, online: <[http://www.komantech.com/product/Ultra\\_AT\\_R40\\_12.htm](http://www.komantech.com/product/Ultra_AT_R40_12.htm)>.
- [19] Sample Ultrasonic Amplifier Circuit, Accessed 2 Jan. 2009, online: <[http://www.massmind.org/images/www/hobby\\_elec/e\\_sonic1\\_3.htm](http://www.massmind.org/images/www/hobby_elec/e_sonic1_3.htm)>.
- [20] Sample Ultrasonic Amplifier Circuit, Accessed 2 Jan. 2009, online: <<http://www2.itu.edu.tr/~gunesec/bitirme/dincer/donanim.html>>.
- [21] B. Carter, "Application Note: A Single-Supply Op-Amp Circuit Collection, Nov. 2000", Accessed 2. Jan 2009, online: <<http://instruct1.cit.cornell.edu/courses/bionb440/datasheets/SingleSupply.pdf>>.
- [22] TL072 Datasheet, Accessed 2. Jan 2009, online: <<http://www.datasheetcatalog.org/datasheet/stmicroelectronics/2298.pdf>>.
- [23] USB-6009 Datasheet, Accessed 2 Jan. 2009, online: <<http://www.ni.com/pdf/products/us/20043762301101dlr.pdf>>.
- [24] P. Kyritsi, D. C. Cox, R. A. Valenzuela, and P. W. Wolniansky, "Correlation analysis based on MIMO channel measurements in an indoor environment", IEEE Journal on Selected Areas in Communications, vol. 21, no. 5, pp.713-720, June 2003.
- [25] D. S. Shiu, G. J. Foschini., M. J. Gans, and J. M. Kahn, "Fading correlation and its effect on the capacity of multielement antenna systems", IEEE Trans. on Communications, vol. 48, no. 3, pp. 502-513, March 2000.

- [26] N. Levanon, E. Mozeson, Radar Signals, 1<sup>st</sup> Ed. NY: John Wiley & Sons Inc., 2004.
- [27] M. I. Skolnik, Radar Handbook, 3<sup>rd</sup> Ed. NY: McGraw-Hill, 2008.
- [28] A. Goldsmith, Wireless Communications, 1<sup>st</sup> Ed. NY: Cambridge University Press, 2005.
- [29] J. Dunlop, D. Girma, and J. Irvine, Digital Mobile Communications and the Tetra System, 1<sup>st</sup> Ed. NY: John Wiley & Sons Inc., 1999.
- [30] J. Proakis, Digital Communications, 4<sup>th</sup> Ed. NY: McGraw-Hill, 1995.
- [31] PIC 18F452 Datasheet, Accessed 2 Jan. 2009, online: <<http://ww1.microchip.com/downloads/en/DeviceDoc/39564c.pdf>>.
- [32] MAX 232 Datasheet, Accessed 2 Jan. 2009, online: <<http://www.datasheetcatalog.org/datasheet/maxim/MAX220-MAX249.pdf>>.
- [33] B. K. A. Ramu, “Implementing FIR and IIR Digital Filters Using PIC18 Microcontrollers”, Accessed 2 Jan. 2009, online: <<http://ww1.microchip.com/downloads/en/AppNotes/00852a.pdf>>.
- [34] LM 7805 Datasheet, Accessed 2 Jan. 2009, online: <<http://www.fairchildsemi.com/ds/LM/LM7805.pdf>>.
- [35] C Compiler Reference Manual, 4<sup>th</sup> Version, 2006, Accessed 2 Jan. 2009, online: <[http://web.ee.sun.ac.za/~nrossouw/Data/Programmering/ccs\\_c\\_manual\\_v4\\_Augustus\\_2006%20.pdf](http://web.ee.sun.ac.za/~nrossouw/Data/Programmering/ccs_c_manual_v4_Augustus_2006%20.pdf)>.

- [36] LM 324 Datasheet, Accessed 2 Jan. 2009, online: <<http://www.datasheetcatalog.org/datasheet2/c/0hi5uu6hphuyzfkzs5a014cyyuyy.pdf>>.
- [37] Ultrasonic Transducers' Specifications, Accessed 2 Jan. 2009, online: <<http://www.robot-electronics.co.uk/datasheets/t400s16.pdf>>.